MECHANICAL AND BIOLOGICAL EVALUATIONS OF HYDROXYAPATITE COMPOSITE FOR ORTHOPEDIC APPLICATIONS

SAEID BARADARAN

THESIS SUBMITTED IN FULFILLMENT OF THE REQUIREMENTS FOR THE DEGREE OF DOCTOR OF PHILOSOPHY IN MECHANICAL ENGINEERING

FACULTY OF ENGINEERING
UNIVERSITY OF MALAYA
KUALA LUMPUR

2015

UNIVERSITI MALAYA
ORIGINAL LITERARY WORK DECLARATION

Name of Candidate: Saeid Baradaran   I.C/Passport No: P95424219

Registration/Matric No: KHA110123

Name of Degree: PHD of Engineering
Title of Project Paper/Research Report/Dissertation/Thesis ("this Work"):

Mechanical and biological evaluations of Hydroxyapatite Composite for Orthopedic Applications.

Field of Study: Advanced Materials (Biomaterials, Bioceramic)

I do solemnly and sincerely declare that:

(1)   I am the sole author/writer of this Work;
(2)   This Work is original;
(3)   Any use of any work in which copyright exists was done by way of fair dealing and for permitted purposes and any excerpt or extract from, or reference to or reproduction of any copyright work has been disclosed expressly and sufficiently and the title of the Work and its authorship have been acknowledged in this Work;
(4)   I do not have any actual knowledge nor do I ought reasonably to know that the making of this work constitutes an infringement of any copyright work;
(5)   I hereby assign all and every rights in the copyright to this Work to the University of Malaya ("UM"), who henceforth shall be owner of the copyright in this Work and that any reproduction or use in any form or by any means whatsoever is prohibited without the written consent of UM having been first had and obtained;
(6)   I am fully aware that if in the course of making this Work I have infringed any copyright whether intentionally or otherwise, I may be subject to legal action or any other action as may be determined by UM.

 Candidate's Signature   Date

Subscribed and solemnly declared before,

Witness's Signature   Date

Name:

Designation:

ACKNOWLEDGEMENTS

ABSTRACT

Hydroxyapatite (HA) has received wide attention in orthopedics, due to its biocompatibility and osseointegration ability. Despite these advantages, the poor mechanical properties of HA often results in rapid wear and premature fracture of implant. Hence, there is a need to improve the mechanical properties of HA without compromising its biocompatibility. The aim of the current research is to explore the potential of metal ion doping and graphene nanosheets (GNS) as reinforcement to HA for orthopedic implants. HA/reduce graphene oxide (rGO) and Ni doped HA/Graphene nano platelet (GNP) are synthesized by hydrothermal and chemical precipitation and characterized by XRD, FT-IR, EDAX, FESEM and Raman spectroscopy. HA/reduce graphene oxide (rGO) and Ni doped HA/ Graphene nanoplatelet (GNP) powder are solidified by hot iso-static pressing, and investigated for their mechanical and biological behavior. In this aspect, rGO, GNP and metal ions reinforcement improve the mechanical properties of HA for free standing composites. In case of nHA/rGO, the fracture toughness and modulus elasticity improves 40% and 86% by wt.%1.5 GNS and hardness increases 32% by wt.%1.0 GNP in compare to HA. In another case (HA-Ni/GNP), microhardness, fracture toughness and elastic modulus of 6%Ni doped HA were improved 55% , 60% and 121% in 6% doping of Ni and also 75%, 164% and 85% in 1.5Ni6, respectively. Both cases have demonstrated a positive influence on the proliferation, differentiation and matrix mineralization activities of osteoblasts, during in-vitro biocompatibility studies in presence of GNS.

ABSTRAK

Hydroxyapatite (HA) telah mendapat perhatian yang luas dalam ortopedik, kerana kemampuannya biocompatibility dan osseointegration itu. Walaupun kelebihan ini, sifat-sifat mekanikal miskin HA sering menyebabkan haus pesat dan patah pramatang implan. Oleh itu, terdapat keperluan untuk meningkatkan sifat mekanik HA tanpa menjejaskan biocompatibility itu. Tujuan kajian semasa adalah untuk meneroka potensi ion logam doping dan nanosheets graphene (GNS) sebagai tetulang kepada HA untuk implan ortopedik. HA/mengurangkan graphene oksida (rGO) dan Ni didopkan HA/graphene nano platelet (GNP) yang disintesis oleh hidroterma dan pemendakan kimia dan ciri-ciri XRD, FT-IR, EDAX, FESEM dan spektroskopi Raman. HA / mengurangkan graphene oksida (rGO) dan Ni didopkan HA/graphene nano platelet (GNP) serbuk yang digabungkan dengan panas iso-statik menekan, dan disiasat bagi kelakuan mekanikal dan biologi mereka. Dalam aspek ini, rGO, GNP dan ion logam tetulang meningkatkan sifat mekanik komposit HA untuk berdiri bebas. Dalam kes nHA/rGO, keliatan patah dan keanjalan modulus meningkatkan 40% dan 86% oleh berat.% 1,5 GNP dan kekerasan meningkat 32% oleh berat.% 1,0 GNS dalam ke HA. Dalam kes yang lain (HA-Ni/GNP), microhardness, patah kekuatan dan modulus elastik 6% Ni didopkan HA telah meningkat 55%, 60% dan 121% dalam 6% doping Ni dan juga 75%, 164% dan 85% dalam 1.5Ni6 masing-masing. Kedua-dua kes telah menunjukkan pengaruh yang positif ke atas percambahan, pembezaan dan matriks mineral aktiviti osteoblas, semasa dalam vitro kajian biocompatibility di hadapan GNS.

Table of Contents

List of Figures

List of Tables

List of Scheme

List of Symbols and Abbreviations

ALP	Alkaline phosphates
NH_4OH	Ammonium hydroxide
$NH_4H_2PO_4$	Ammonium dihydrogen orthophosphate
ANOVA	Analysis of variance
AD	Apparent density
P	Applied indentation load
BCP	Biphasic calcium phosphate
$CaCO_3$	Calcium carbonate
$CaCl_2$	Calcium chloride
$Ca(NO_3)_2 \cdot 4H_2O$	Calcium nitrate tetrahydrate
CaO	Calcium oxide
CP	Calcium phosphate
CNF	Carbon nano fiber
CNM	Carbon nano material
CNS	Carbon nano sheet
CNT	Carbon nanotube
CVD	Chemical vapor deposition
CTAB	Cetyl trimethyl ammonium bromid
CICP	Cross-Linked C-Telopeptides of Type
CS	Conventional sintering
X_C	Crystallinity
DI	Deionized water
DCP	Dicalcium phosphate
DCPA	Dibasic calcium phosphate anhydrous
DCPD	Dibasic calcium phosphate dihydrate
ddH_2O	Double distilled water

ECM	Extracellular matrix
EDS	Energy-dispersive X-ray spectroscopy
EG	Ethylene glycol
FESEM	Field emission scanning electron microscopy
FT-IR	Fourier transform infrared spectroscopy
K_{IC}	Fracture toughness
GNP	Graphene nanoplatelet
GO	Graphene oxide
HV	Hardness Vickers
HMDS	Hexamethyldisilane
HIP	Hot isostatic pressing
HP	Hot pressing
hFOB	Human fetal osteoblastic cell
HCl	Hydrogen chloride
H_2O_2	Hydrogen peroxide
HA	Hydroxyapatite
JCPDS	Joint committee on powder diffraction and standards
Mg	Magnesium
Mn	Manganese
MSC	Mesenchymal stem cell
MTT	Methyl thiazole tetrazolium
MS	Microwave sintering
NCD	nanocrystalline diamond
DMF	N,N-Dimethylformamide
$Ni(NO_3)_2 \cdot 6H_2O$	Nickle II nitrate hexahydrate
HNO_3	Nitric acide
NMP	N-Methylpyrrolidinone

OCP	Octacalcium phosphate
OC	Osteocalcin
OHA	Oxyhydroxyapatite
H_3PO_4	Phosphoric acid
PGA	Poly(glycolic acid)
PLA	Poly(lactic acid)
PLGA	Poly(lactic-co-glycolic acid)
$KClO_3$	Potassium chlorate
$KMnO_4$	Potassium permanganate
rGO	Reduced graphene oxide
SLS	Selective laser sintering
Si_3N_4	Silicon nitride
Ag	Silver
SBF	Simulated body fluid
Ksp	Solubility product equilibrium constant
SPS	Spark plasma sintering
SD	Standard deviation
Sr	Strontium
H_2SO_4	Sulfuric acid
TEM	Thermo gravimetric analysis
THF	Tetrahydrofuran
TTCP	Tetracalcium phosphate
TEM	Transmission electron microscope
TCP	Tricalcium phosphate
f	Volume fraction of grain boundary
XRD	X-ray Diffraction
E	Young's modulus

Zn   Zinc

$ZrBr_2$ Zirconium (II) bromide

CHAPTER I: INTRODUCTION

1.1   Background of Study

With societal development and improved living conditions, individuals focus on medical care and rehabilitation. Injuries to human hard tissue system account for more than one million surgeries annually. As such, demands for biomaterials to rehabilitate bone defects caused by damage, infection, or tumors, as well as osteoporosis and osteomalacia caused by aging, have increased. Global Information reported that orthopedic biomaterial device markets, which are among the major biomaterial-providing regions, generated approximately $115.4 billion in 2008; this amount is predicted to increase to $252.7 billion in 2014. This finding indicates that demands for diverse orthopedic biomaterials has increased by 18% to 20% per year (Moussy, 2010). Therefore, the quality and quantity of hard tissue rehabilitation materials should be improved. Bone graft materials with good mechanical properties and appropriate biological properties should also be developed to successfully perform bone replacement surgery. Alternative materials for bone graft are categorized into natural materials (autografts, allografts, and xenografts) and artificial bone (metals, ceramics, and polymers).

The human skeletal system is composed of a diverse hierarchical architecture of various tissues and cellular components. For example, bone is an inorganic–organic composite consisting of collagen proteins and hydroxyapatite (HA) (Oryan et al., 2014; Scaglione & Quarto, 2009; Vertenten et al., 2010). In case of severe injuries to the skeletal system, bone grafts are required to repair damage. In bone repair, natural materials, such as autografts, are preferred bone grafts. In autografts, bone is harvested from a different body part of a patient. Autografts are also regarded as one of the safest grafts because these materials pose low risk of disease transmission; low risk is

observed because autografts contain a high amount of a patient's bone-growing cells and proteins. However, autografts are limited by insufficient available tissues, additional costs, and intensive surgical procedures. In contrast to autografts, allografts involve the use of another individual's bone skeleton as bone implant. Similar to autografts, allografts consist of a natural bone structure and exhibit high bioactivity. Despite these advantages, allografts induce antigenicity and pathogen transmission between a bone provider and a patient. In some cases, patients have to wait for a bone source. In addition to autografts and allografts, xenografts are biomaterials used for transplantation; unlike autografts and allografts, xenografts are transplanted from a donor to a recipient of different species (e.g., baboon to human). Although allografts and xenografts provide several benefits, these materials trigger immune response and promote disease transmission. Another large family of bone graft alternatives includes synthesized materials. These materials have been used to produce artificial materials that behave similarly to native autografts.

Materials science and biomedical science focus on creating new biomaterials. New materials have been developed to rehabilitate bone defects. These biomaterials should exhibit biocompatibility and mimic natural bone properties, such as matching functional and mechanical behaviors with a damaged tissue to be replaced. A stable bond between an implant and a natural bone should also be established. Numerous implant materials, generally composed of metals, polymers, ceramics, and their composites, have been evaluated for biomedical applications to treat bone defects. These implants are classified into three categories based on *in-vivo* responses: (1) bioinert implants that do not exhibit interaction between implants and bone; (2) bioactive implants that interact chemically with bone after these materials are implanted for a particular range of time; and (3) bioresorbable implants that are gradually resorbed and completely replaced with new bone ingrowths (Carta et al., 2005; Yelten et al.,

2012). Although these materials have been clinically applied, these materials present many disadvantages. Metals and polymers were the first biomaterials used to replace hard tissues. Common metals for clinical applications include stainless steel and titanium, as well as its alloys. Some hip joints, bone fixing plates, and bolts are composed of these metals. However, stress shielding occurs when these metals are used to replace hard tissues, particularly under load bearing conditions. A tissue bearing overload or underload usually degrades; as a consequence, implantation fails. Metallic materials cannot also bond well to natural bones. Fibrous tissue is formed around metal implants, and bonding strength is low; thus, poor stress-transforming conditions occur. Some harmful metal elements are released into the body because of metal corrosion and wear in the internal environment of a human body. By contrast, polymer materials can be easily formed; some of these materials, such as polylactic acid (PLA), polyglycolic acid (PGA), and poly (lactic-co-glycolic) acid (PLGA), are biocompatible and biodegradable. Nevertheless, the degradation rate of these materials is not equivalent to the growth rate of new bone (Burdick & Mauck, 2011; Yaszemski, 2013). Realizing that bone consists of a large amount of inorganic components, researchers have used various synthetic ceramic materials as bone substitutes for more than 30 years. Alumina and zirconia are the first ceramics introduced to biomedical applications because these materials exhibit excellent corrosion resistance, high wear resistance, and high strength (De Aza et al., 2002). Despite these excellent properties, these materials are bio-inert; therefore, these materials cannot bind directly to tissues. Instead, a fibrous membrane forms around implanted materials (Manicone et al., 2007).

Calcium phosphates are of great interest in interdisciplinary sciences encompassing chemistry, biology, medicine, and geology. Calcium phosphates are mostly classified as resorbable biomaterials. As such, these biomaterials dissolve under

physiological conditions. In general, the solubility trend of calcium phosphate materials is as follows:

$$CaHPO_4 \; (DCP) > Ca_4(PO_4)_2 \; (TTCP) > Ca_3(PO_4)_2 \; (TCP) > Ca_5(PO_4)_3(OH) \; (HA)$$

HA is thermodynamically stable at body temperature because HA is relatively insoluble (HA; $K_{sp} = 2.34 \times 10^{59}$) under physiological conditions (Dorozhkin, 2013; Y. Yang et al., 2011). This compound is chemically similar to the mineral component of bones and hard tissues in mammals. HA is one of few materials classified as bioactive; as such, this material supports bone ingrowth and osseointegration when HA is used in orthopedic, dental, and maxillofacial applications. The bioactivity and osteoconductivity of HA provide a suitable condition for new bone growth and integration (Dorozhkin, 2013; Oh et al., 2006). Thus, HA is extensively investigated and clinically used as a freestanding implant, coating on metallic implants, and reinforcement in polymer scaffold materials for tissue regeneration (Hong et al., 2005; Pielichowska & Blazewicz, 2010; Shepperd & Apthorp, 2005). However, freestanding HA implant or HA coatings exhibit several disadvantages, such as poor fracture toughness (K_{IC}) and wear resistance (Y. Chen et al., 2007; Y. Gu et al., 2004; Yu et al., 2003). K_{IC} of dense HA (1 MPa·m$^{0.5}$) is significantly lower than the minimum reported K_{IC} of cortical bone (2 MPa·m$^{0.5}$) (Tan et al., 2011). Bones are load-bearing parts of a living body. These tissues should possess good K_{IC} to prevent cracking and fracture when high and cyclic loading is applied during limb movement and actions. Therefore, K_{IC} of HA should be improved when bone is replaced with an implant or coating. Poor K_{IC} also results in low wear resistance of HA because wear volume loss in ceramics is directly related to K_{IC} (Coathup et al., 2005; Lahiri, Benaduce, et al., 2011).

One of the possible solutions is HA reinforcement with a second-phase material that can help improve mechanical and biological properties of HA. Considering the

4

biocompatibility of a composite structure, an ideal reinforcement material should be able to significantly increase mechanical properties with a low content of reinforced phase. Low content of reinforcement phase ensures that minimum amount of foreign element is introduced to the internal environment of a living body. HA integrates with bones because this substance contains similar chemical composition to the mineral component of bones. Thus, reinforcement phase should possess excellent elastic modulus (E) and strength; with excellent E and strength, minimum content of reinforcement phase can significantly increase K_{IC} of HA.

1.2   Motivation

Bone injuries aggravated by malformations, disease, developmental deformity, trauma, or adverse effects from medical treatments have increased the demand of improved bone implant materials (L. L. Hench & Polak, 2002). Affected bones are repaired using surgical techniques with autogenous grafts, allogenous grafts, internal and external fixation devices, electrical stimuli, and replacement implants. Several implant materials, such as metals, polymers, ceramics, and composites, have been evaluated and applied in biomedical industries. Among these materials, synthetic HA ceramics have been widely utilized as an implant material because the composition of this material is similar to inorganic ingredients of bones (Best et al., 2008). Compared with natural bone, synthetic HA exhibits poor mechanical properties, such as low strength and toughness (D.-M. Liu et al., 2001). Therefore, synthetic HA has been used as an implant and coating on metals, such as stainless steel and titanium, as well as its alloys (Geetha et al., 2009). Inferior osteogenic capacity and poor mechanical strength cause slow bone growth on or through implant surfaces, thereby delaying recovery. Decreased osteogenic capacity and mechanical properties of synthetic HA are attributed to subtle but significant chemical differences, such as those observed in trace elements,

including Mg^{2+}, Sr^{2+}, Zn^{2+}, F^-, and CO_3^{2-} (Bandyopadhyay et al., 2006; Young, 1974). This result suggests that adding trace elements, as well as changing surface property that favors interaction between a graft material and a natural bone, can be performed to improve the osteogenic capacity and mechanical properties of synthetic HA. In addition, a graphene nanosheet (GNS), with excellent stiffness and strength has been considered as a potential reinforcement to HA because this material has overcome limitations related to mechanical and biological properties. GNS possesses Young's modulus of up to 1 TPa and intrinsic strength of approximately 130 GPa (C. Lee et al., 2008). Studies on GNS-reinforced ceramic/polymer matrix composites have successfully demonstrated that this material can improve structural properties, such as strength, E, and wear resistance (Y. Fan et al., 2010; X. Wang et al., 2012). In addition to E, K_{IC} of any ceramic-based composite system can be enhanced by GNS through energy absorption *via* crack deflection and crack bridging (J. Liu et al., 2013; J. Liu et al., 2012; Kai Wang et al., 2011). GNS can also enhance mechanical properties, including wear resistance and K_{IC}. This study aimed to develop techniques for doping metal ions and creating composites with GNS to improve the mechanical and biological properties of HA.

1.3   Objective of Study

This project aimed to develop biocomposites with mechanical strength similar to that of natural bone and superior bioproperties; these biocomposites could be used as bone rehabilitation materials in orthopedic applications. HA is the main mineral composition of natural bone; this component exhibits excellent bioproperties. As such, HA was selected to fabricate ceramic composites. Ceramics sintered with nano-sized HA particles display superior mechanical and biological properties. Therefore, nano-sized HA particles were prepared to produce ceramic matrix. The small grain size of ceramic provides greater toughness than the sintered material from conventional micro-

sized HA particles. Biocompatible reinforcements, such as graphene and metal ion-doped materials, with unique reinforcing ability were used to enhance the mechanical strength of HA ceramics. Multi-phase reinforcing effects of graphene and metal ion-doped were considered. Different reinforcing phases and reinforcing mechanisms were also investigated. Mechanical reinforcing mechanisms and biological concerns were considered to develop a series of new bioceramic composites for orthopedic applications.

This study aims to achieve the following specific objectives:

- To perform different methods to synthesize nano-sized HA particles, which are similar to those in natural bone; with different morphology are expected to be achieved.
- To investigate the reinforcing effects of graphene and metal-ion doped materials and the influence of filling percentages on the mechanical strength of fabricated composites.
- To evaluate *in-vitro* the biocompatibility of composites through proliferation, viability, and cytotoxicity assays using a bone cell.

Figure 1.1 summarizes the experiments conducted in this study.

In this project, HA-graphene and HA-metal ion doped-graphene composites are designed and fabricated. The mechanical strength and biological properties of HA composite ceramic is improved by combining the reinforcing effects of graphene and metal-ion doped materials.

1.4   Organization of This Thesis

This thesis is divided into five chapters as follows:

Chapter One highlights the background of the study and the problems existing in this area, which served as the motivation of this project. **Chapter One** also presents the objective of this study.

Chapter Two provides a literature review, which discusses the properties of HA, fabrication methods of HA particles and composites, properties of graphene, and treatment methods of biocomposites.

Chapter Three describes the methodology used in this project. A reinforcement method with nanoparticle and phase-transformation reinforcements of HA, as well as graphene and metal ion-doped material reinforcements, was developed and designed to enhance mechanical properties of HA composites. The fabrication, characterization, and details of composite material synthesis are also described in this chapter.

Chapter Four introduces and discusses the testing methods of the mechanical and bioactivity of HA composites. The growth status of cells and a new apatite layer on the sample surface are examined in this chapter.

Chapter Five presents comprehensive conclusions and recommendations for further studies. The originality of this project is also summarized in this chapter.
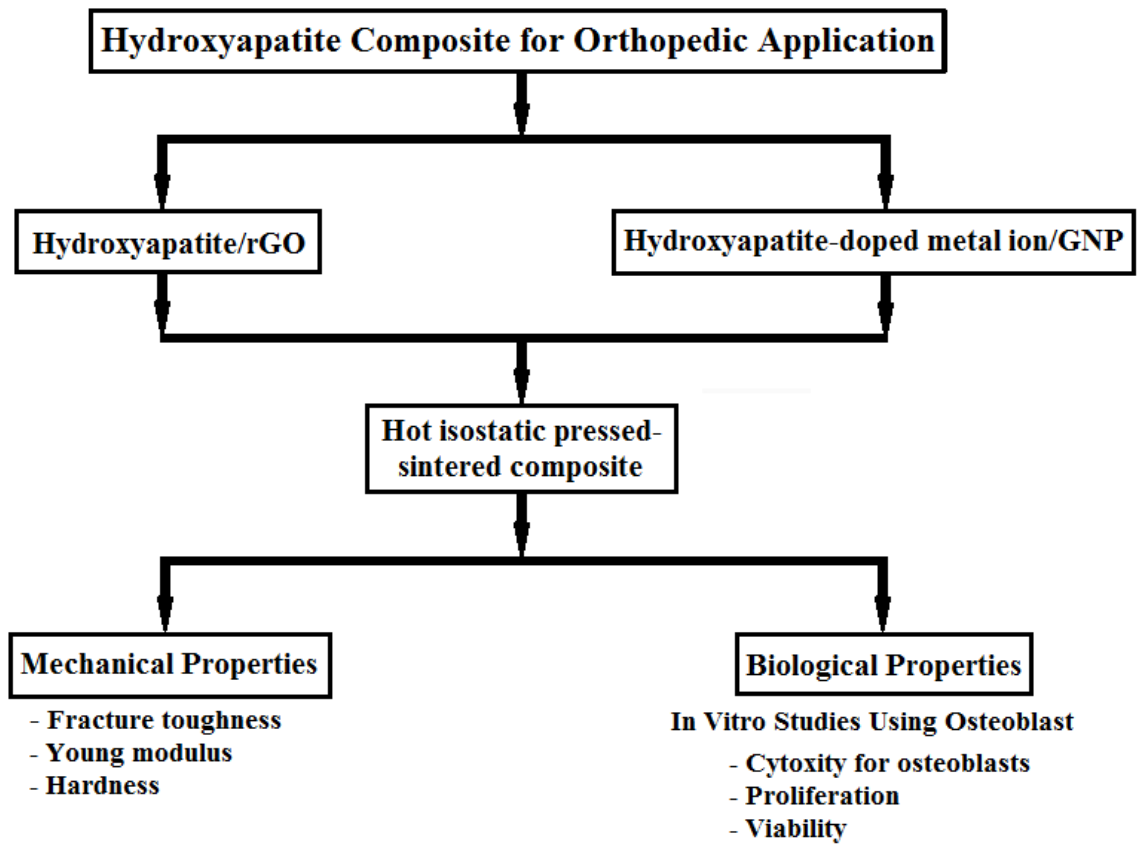
Figure 1.1 Flow chart of the research plan.

Chapter II: LITERATURE REVIEW

2.1 Overview of Bioceramics

Bioceramics have been widely used in orthopedic applications in the past few decades because these materials exhibit biocompatibility, superior corrosion resistance, excellent chemical stability, mechanical strength, and non-toxicity under physiological conditions (L. Hench, 1993; Lacefield et al., 1993). Bioceramics can be categorized into three parts according to their bioactivity after implantation: bioinert, biodegradable, and bioactive (L. L. Hench et al., 1993). Bioinert ceramics are stable; no chemical reaction or biodegradation occurs during long-term implantation. In general, a fibrous tissue is formed between a natural bone and a bioinert implant; therefore, bonding strength with a natural bone is weak. Bioinert ceramics are widely used because these materials exhibit superior mechanical strength, wear resistance, modest K_{IC}, and excellent corrosion resistance compared with the two other types. Alumina and zirconia are typical bioinert ceramics used in orthopedic applications, such as hip prostheses, dental implants, and joint prostheses. Biodegradable ceramics degrade gradually in a physical environment. These materials can act as support for the growth of new bone during rehabilitation and stimulate immature bone formation. β-Tricalcium phosphate (β-TCP) is a typical biodegradable ceramic, which has been successfully used since 1920 (Albee, 1920; Hulbert et al., 1982). Biodegradable ceramics cannot be used in orthopedic applications because these materials exhibit low mechanical strength.

Over the last two decades, bioactive ceramics can directly bond to natural bone without forming fibrous tissues around bioactive implants. Thus, bioactive ceramics have been extensively investigated. HA [$Ca_{10}(PO_4)_6(OH)_2$], which is the main mineral constituent of human and animal hard tissues, is a typical bioactive ceramic (Bonner et al., 2001; L. L. Hench & Ethridge, 1972; Suchanek et al., 1996). This compound can

induce new bone generation and support bone growth; as a result, a strong chemical bond is formed between HA implants and natural bone. The bonding strength of the interface between HA implants, and bone is 5 or 7 times as much as that between other bioinert ceramics and natural bone. The bonding strength of the interface is very high; therefore, fractures are usually generated in HA or natural bone but not at the interface (Okumura et al., 1991). Moreover, the bonding zone between HA and natural bone exhibits a high-gradient Young's modulus (L. Hench, 1993), which compensates the difference in Young's modulus between HA implant and natural bone. Therefore, load can be effectively transferred between HA implant and natural bone. Several typical mechanical strength values of these bioceramics are listed in Table 2.1.

Table 2.1 Mechanical properties of bioceramics (B. Chen et al., 2008; Yoshida et al., 2006)

	Bioinert ceramics		Bioactive ceramics	Biodegradable ceramics
	Al_2O_3	ZrO_2	HA	β-TCP
Flexural strength (MPa)	595	1000	60-90	36-47
Fracture toughness (MPa.m1/2)	4-6	7	0.60-0.95	0.40-0.80
Young`s modulus (GPa)	380-420	150-200	40-120	33-90

2.2 Calcium Phosphates (CP)

Calcium phosphates (CPs) are some of the most extensively investigated bioceramics. These materials are first used in clinical applications as fillers of bone defects in the 1920s and first incorporated in dentistry and orthopedics in the 1980s (Bohner, 2000). Various types of CP materials include HA, β-TCP, α-TCP, and tetracalcium phosphate (TTCP), among others. These materials differ from one another in terms of Ca/P molar ratio. Table 2.2 lists several calcium phosphates according to Ca/P molar ratio. This ratio is an important parameter that determines the acidity and solubility of CPs. A low Ca/P molar ratio corresponds to highly acidic and water-soluble CPs. For example, monocalcium phosphate monohydrate is highly soluble;

TTCP is unstable under aqueous conditions. HA, TCP, hydrated dicalcium phosphate (DCP), and anhydrous calcium phosphate are soluble *in-vivo* (R. Z. LeGeros & LeGeros, 1993; Ravaglioli & Krajewski, 1992). Although CP compositions have been considered, HA with a Ca/P molar ratio of 1.67 has been extensively investigated (Gauthier et al., 2001; Osborn & Newesely, 1980) because HA contains a chemical composition and structure comparable with those of natural bone mineral (De Jong, 1926).

Considering natural bone composition, which is approximately 70% HA by weight and 50% HA by volume, researchers also used HA as a bone substitute material. CPs are compounds of great interest in interdisciplinary sciences encompassing chemistry, biology, medicine, and geology. Most CPs are classified as resorbable biomaterials. Thus, these compounds dissolve under physiological conditions. The solubility trend of CP materials is as follows:

$$CaHPO_4 (DCP) > Ca_4 (PO_4)_2 (TTCP) > Ca_3 (PO_4)_2 (TCP) \gg Ca_5 (PO_4)_3 (OH) (HA)$$
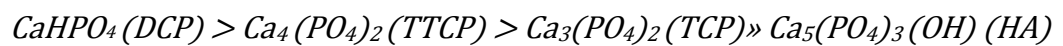
HA is thermodynamically stable at body temperature because HA is relatively insoluble ($K_{sp} = 2.34 \times 10^{59}$) under physiological conditions. HA is chemically similar to the mineral component of bones and hard tissues in mammals. This compound is a bioactive material, indicating that HA supports bone ingrowth and osseointegration when this material is used in orthopedic, dental, and maxillofacial applications (Dorozhkin, 2013).

Table 2.2 Various calcium phosphates with their respective Ca/P molar ratios
(Dorozhkin, 2010)

Ca/P	Compound	Formula
0.5	Calcium metaphosphate (α,β,γ)	$Ca(PO_3)_2$
0.5	Monocalcium phosphate monohydrate (MCPM)	$Ca(H_2PO_4)_2.H_2O$
0.5	Monocalcium phosphate anhydrous (MCPA)	$Ca(H_2PO_4)_2$
0.67	Tetracalcium dihydrogen phosphate (TDHP)	$Ca_4H_2P_6O_{20}$
0.7	Heptacalcium phosphate (HCP)	$Ca_7(P_5O_{16})_2$
1.0	Dicalcium phosphate dehydrate (DCPD), mineral brushite	$CaHPO_4.2H_2O$
1.0	Dicalcium phosphate anhydrous (DCPA), mineral monetite	$CaHPO_4$
1.33	Octacalcium phosphate (OCP)	$Ca_8(HPO_4)_2(PO_4)_4.5H_2O$
1.5	α-Tricalcium phosphate (α-TCP)	α-$Ca_3(PO_4)_2$
1.5	β-Tricalcium phosphate (β-TCP)	β-$Ca_3(PO_4)_2$
1.2-2.2	Amorphous calcium phosphate (ACP)	$Ca_{10-x}H_{2x}(PO_4)_6(OH)_2$
1.5-1.67	Calcium-deficient hydroxyapatite (CDHA) [e]	$Ca_{10-x}(HPO_4)_x(PO_4)_{6x}(OH)_{2\_x}$ [f] $(0 < x < 1)$
1.67	Hydroxyapatite (HA or OHAp)	$Ca_{10}(PO_4)_6(OH)_2$
1.67	Fluorapatite (FA or FAp)	$Ca_{10}(PO_4)_6F_2$
2.0	Tetracalcium phosphate (TTCP), mineral hilgenstockite	$Ca_4(PO_4)_2O$

[e] Occasionally, is named as precipitated HA.
[f] In the case x=1 (the boundary condition with Ca/P=1.5), the chemical formula of CDHA looks as follows: $Ca_9(HPO_4)(PO_4)_5(OH)$.

2.2.1 Hydroxyapatite (HA)

HA is the main component of teeth and bone minerals; this component represents a large proportion of the elementary composition of the human body. The chemical formula of HA is $[Ca_{10}(PO_4)_6(OH)_2]$, indicating that HA is a basic calcium phosphate with Ca/P ratio of 1.67. This compound is medically and dentally applied as artificial bone, bone filler, bone formation promoter, bioelectrode, drug delivery carrier, dental and bone cements, root canal filler, and dental implants (Aoki, 1994). HA is a highly biocompatible, bioactive ceramic with osteoconductive properties; as a result, a strong chemical bond is formed with bone and bone tissue (Blokhuis et al., 2000; Ghanaati et al., 2012). Previous studies showed the high degree of biocompatibility and bioactivity of HA (Jansen et al., 1993; Martin et al., 1993). Although, HA is a very desirable material for biomedical applications because of high biocompatibility and bioactivity, some of the mechanical properties of HA greatly limit its applications.

Table 2.3 Properties of HA and cortical Bone (Hench et al., 1993)

Mechanical and physical properties	Hydroxyapatite	Natural Bone
Young`s modulus (GPa)	40-120	7-30
Compressive strength (MPa)	300	10-230
Bending strength (MPa)	110-200	200
Fracture toughness (MPa.m$^{1/2}$)	<1	2-12
Poisson`s	0.27	0.30

If mechanical properties of HA can be enhanced to achieve similar properties to those of natural bone, potential applications of HA in orthopedics and in other fields of medicine would likely increase. Bone in-growth in HA is excellent, as previously mentioned. The modulus of this material is greater than that of bone, but HA does not provide the degree of stress shielding similar to that of metallic implants with much higher moduli. The compressive strength in a dense form is comparable at 300 MPa, but the bending strength of approximately 112 MPa is set as cut, and 196 MPa polished to a surface finish of 1 pm is not at par (Thomas et al., 1980). K_{IC} of HA is <1 MPa·m$^{1/2}$, whereas K_{IC} of bone is 2 MPa·m$^{1/2}$ to 12 MPa·m$^{1/2}$ depending on bone type, location, and age. To enhance the reliability of HA in bone replacement applications, researchers should set K_{IC} of at least 2 MPa·m$^{1/2}$. The comparative data of HA and natural bone are shown in Table 2.3.

2.2.1.1 Structure of Hydroxyapatite
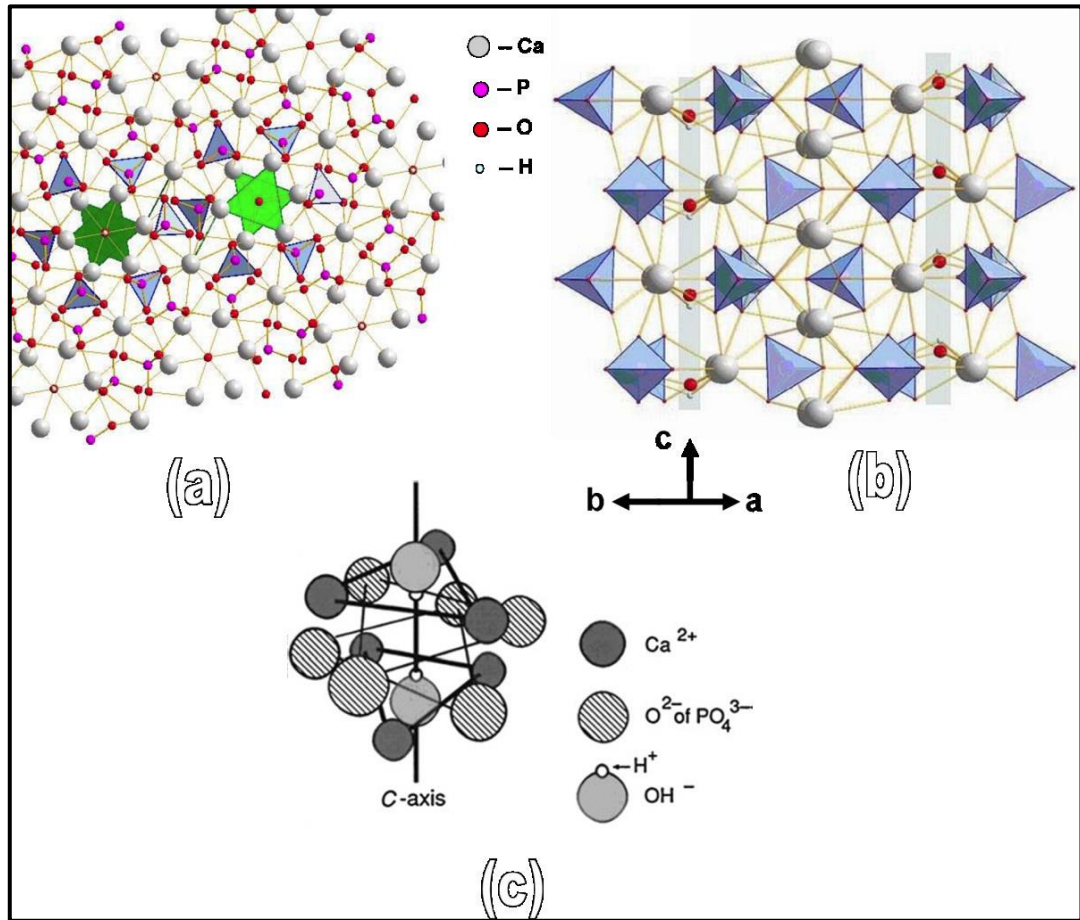
Figure 2.1 HA structure - formation of pseudo-one-dimensional OH channels (a) OH dipoles form chains along crystallographic c-axes, (b) view on the OH channels from the plane cross section. PO$_4$ group is shown as tetrahedral, (c) simplified unit cell structure of HA showing that OH groups are aligned along columnar C directions (Nakamura et al., 2001; Terra et al., 2002)

The most common bioactive ceramic material is HA [Ca$_{10}$(PO$_4$)$_6$(OH)$_2$], which contains similar composition to bone and teeth. Between the two known crystal forms of HA, namely, monoclinic (space group P2$_1$/b) and hexagonal (space group P6$_3$/m) phases, only the hexagonal phase is of practical importance because the monoclinic form is destabilized by the presence of even small amounts of foreign ions (Elliott, 1994; Gras et al., 2014). *a* and *c* lattice parameters of HA are 0.9418 and 0.6884 nm, respectively (Ellis et al., 2006). PO$_4^{3-}$ group forms a regular tetrahedron with a central P^{5+} ion and O^{2-} ions in the four corners (Figure 2.1). OH$^-$ groups are also ionically bonded. HA lattice contains two types of calcium positions, namely, columnar and

hexagonal (Terra et al., 2002). Four "columnar calcium" ions occupy [1/3, 2/3, 0] and [1/3. 2/3, 1/2] lattice points.

"Hexagonal calcium" ions are located on planes parallel to the basal plane at $c = 1/4$ and $c = 3/4$. Six (PO_4^{3-}) groups are located on these planes. A significant property of HA is the presence of hydroxyl [OH^-] groups, which are located in columns parallel to the c axis. This phenomenon may be viewed as passing through the centers of triangles formed by "hexagonal calcium" ions (Elliott, 1994). Successive "hexagonal calcium" triangles are rotated at 60°, as indicated by green shade in Figure 1.2. OH^- ions are aligned in columns parallel to the c-axis, along with Ca^{2+} and (PO_4^{3-}) ions, and form OH^- ion chain. In the hexagonal phase, OH dipoles in the same columnar channel may be oriented differently (disordered column model). These dipoles may be oriented similar to a specific column, but orientation is independent of the orientation in neighboring columns (ordered column model of a hexagonal phase).

2.3 Carbon Nano-Structures (CNS)

CNS are some of the most important members of the nanotechnology family of materials. The discovery and emergence of CNS have affected and reshaped various aspects of nanotechnology. These structures have stimulated and contributed to significant developments in physics, electronics, optics, mechanics, biology, and medicine. Carbon nanoscience has rapidly emerged as a new discipline that employs properties of carbon at a nanoscale (Shenderova et al., 2002). These carbon entities include zero-dimensional structures (i.e., fullerenes, particulate diamond, and carbon black), one-dimensional (1D) structures (i.e., nanotubes or nanofibers and diamond nanorods), two-dimensional (2D) structures (i.e., graphene, graphite sheets, and diamond nanoplatelets), and three-dimensional (3D) structures [i.e., nanocrystalline

diamond (NCD) films, nanostructured diamond-like carbon films, and fullerite] (Y. Hu et al., 2006). CNS have been extensively investigated in biology and medicine.

With extraordinary properties, fullerenes and carbon nanotubes (CNTs) have been examined for numerous therapeutic and pharmaceutical purposes since the mid-1990s (Shenderova et al., 2002). Other CNS, such as NCD, have been commonly used because various fabrication and modification techniques have greatly developed. However, CNS in orthopedic applications remains unclear. For instance, the first practical study on carbon nanofibers (CNFs) and CNTs to support osteoblast (bone-forming cell) functions necessary to improve orthopedic implant applications was performed by Webster et al. in 2002 (Elias et al., 2002). In this study, osteoblast proliferation was enhanced. Intracellular protein synthesis, alkaline phosphatase activity, and calcium-containing mineral deposition on nano-diameter CNF are compared with those of conventional micron-diameter carbon fibers and implanted titanium (L. Yang et al., 2011). However, studies on the use of CNS, specifically graphene, in orthopedic medical device applications have grown exponentially (Janković et al., 2014; Lahiri et al., 2012; Lv Zhang et al., 2013). Graphene exhibits excellent mechanical properties (e.g., Young's modulus or E) because of sp^2 carbon-bonding network. Single-layer graphene theoretically yields Young's modulus (E) of 1.02 TPa ($v = 0.149$), which is experimentally validated for a defect-free graphene sheet (flat-shaped structure) with a fracture strength of 42 N·m^{-1} (C. Lee et al., 2008).

The measured mechanical properties of graphene nano platelets (GNPs; Young's modulus, ultimate tensile strength, K_{IC}, fracture energy, and resistance to fatigue crack propagation) indicate that GNPs significantly outperform CNT additives. Young's modulus of graphene nanocomposite was 31% greater than pure epoxy, with 3% increase in single-walled CNTs. The tensile strength of baseline epoxy was enhanced by

17

40% with GNPs compared with that of another substance with 14% improvement in multi-walled CNTs. K_{IC} of mode I of the nanocomposite with GNPs showed 53% increase based on epoxy compared with 20% improvement in multi-walled CNTs. The superiority of GNPs to CNTs in terms of mechanical property enhancement may be related to a high specific surface area, enhanced nanofiller matrix adhesion/interlocking arising from a wrinkled (rough) surface, and 2D (planar) geometry of GNPs (Rafiee et al., 2009).

2.3.1 Graphene Oxide (GO)

GO is a compound of carbon, oxygen, and hydrogen at variable ratios with a single-atomic layer, which is synthesized by exfoliating graphite with strong oxidizers. The bulk product is a brownish/yellowish solid material that retains the layer structure of graphite but with larger and irregular spacing. GO does not require post-production functionalization because this material can be structurally visualized as a graphene sheet; the basal plane of this material is decorated by oxygen-containing groups, such as hydroxyl, carboxyl, and epoxide groups (Figure 2.2). GO is hydrophilic, and this material can be dissolved and dispersed in deionized water (DI), N-Methylpyrrolidinone (NMP), Dimethylformamide (DMF), Tetrahydrofuran (THF), and other solvents that behave similar to water because these groups exhibit high affinity to water molecules. GO is a poor conductor, but light, heat, or chemical reduction treatment can restore most properties of pure graphene (Dreyer et al., 2010; W. Hu et al., 2010; J. Kim et al., 2010; Y. Zhu et al., 2010).
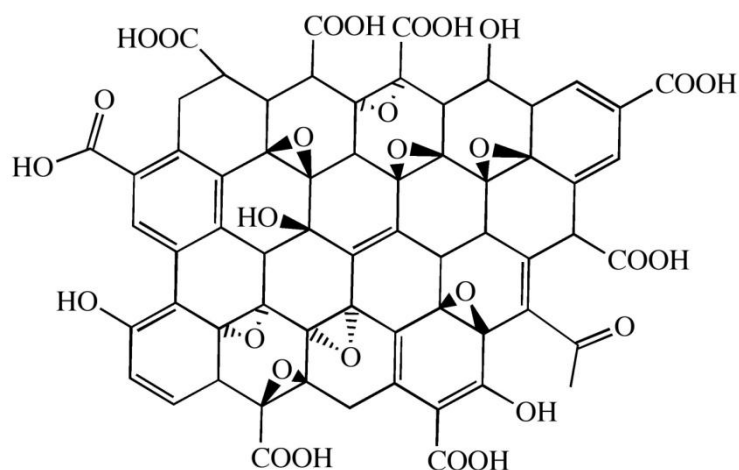
Figure 2.2 Structure of GO with the omission of minor groups (carboxyl, carbonyl, ester, etc.) on the periphery of the carbon plane of the graphitic platelets of GO.

2.3.2 Reduced Graphene Oxide (rGO)

GO is prepared by exfoliating graphite oxide obtained through graphite oxidation in the presence of strong acids and oxidants. One of the most attractive properties of GO is that this material can be (partly) reduced to graphene-like sheets by removing oxygen-containing groups; as a result, a conjugated structure is recovered. Reduced GO (rGO) sheets are usually considered as a type of chemically derived graphene (Pei & Cheng, 2012). The reduction of GO, which is one of the most common chemically converted graphenes, is performed *via* chemical methods by using different reductants, such as hydrazine (Tung et al., 2008), dimethyl hydrazine (Stankovich, Dikin, et al., 2006), hydroquinone (G. Wang et al., 2008), sodium borohydride (Si & Samulski, 2008), hydroiodic acid (Pham et al., 2011), sulfur-containing compounds (W. Chen, L. Yan, & P. Bangal, 2010), ascorbic acid (J. Zhang et al., 2010), and vitamin C (Gao et al., 2010). Among these reductants, hydrazine is widely used because this substance is an effective reducing agent suitable to reduce GO in various media (Dang et al., 2012). However, reduction is very slow, toxic, and dangerously unstable. A green chemistry route of graphene reduction should be investigated. GO reduction has been performed under various conditions, such as alkaline condition, ultraviolet-assisted methods, and

hydrothermal methods (W. Chen, L. Yan, & P. R. Bangal, 2010). Hydrothermal technique is a green method because no hazardous reductants are used (Nethravathi & Rajamathi, 2008; G. Wang et al., 2009; Y. Zhou et al., 2009).

2.3.3   Graphene Nanoplatelet (GNP)

Graphite is a layered compound comprising a series of stacked parallel graphene layers. In a basal plane, each carbon atom is sp^2 hybridized and covalently bonded to three other substances, forming continuous hexagons. The fourth hybridized valence electron is paired with another delocalized electron of the adjacent plane by a much weaker van der Waals force (Pierson, 1993). Delocalized electrons can move readily from one side of the plane to the other side but cannot easily move from one layer to another. Consequently, graphite is highly anisotropic. Table 2.4 summarizes the major properties of graphite.

Table 2.4 Physical properties of graphite

Properties	Basal Plane	Interlayer
Specific gravity (g cm-3)	2.26	
Thermal conductivity (w m-1k-1)	390	2
Electrical conductivity (S cm-1)	4000	3.3
Young`s modulus (GPa)	1060	36.5

Graphene layers in a graphite flake can be readily separated to form thin graphene nanoplatelets (GNPs) through intercalation and exfoliation because of a unique layered structure (Viculis et al., 2005). GNPs are multi-layer particles consisting of 10 to 30 sheets of graphene, but these particles retained much of single-layer properties. GNPs can be produced in bulk quantities through the following: (i) mechanical peeling; (ii) substrate-based methods, such as epitaxial growth and chemical vapor deposition (CVD); (iii) solution-based reduction of GO; and (iv) direct exfoliation of graphite in selected solvents (Novoselov et al., 2004; Alfonso Reina et al., 2008;

Stankovich, Dikin, et al., 2006; Sutter et al., 2008). Platelet primarily refers to the multiple-layer structure of graphene sheets. The use of GNPs is desirable because these materials are cheaper and easier to produce than single-layer graphene or CNTs (Nieto et al., 2012). Moreover, GNPs exhibit exceptional functionalities, high mechanical strength (1 TPa in Young's modulus and 130 GPa in ultimate strength), and chemical stability because of several parameters, such as abundance, cost effectiveness, and high specific surface area, which carries high levels of transferring stress across an interface; thus, reinforcement is enhanced. GNPs are platelet-like graphite nanocrystals with multiple graphene layers (C. Lee et al., 2008; Shen et al., 2013).

2.4 Synthesis of HA

The synthesis of HA particles is usually the first step to fabricate HA implants. HA synthesis is dependent on physical requirements, including crystallinity, particle size, specific surface area, and morphological characteristics, of the resulting HA powder. Various methods, such as sol–gel (Fathi & Hanifi, 2007; Feng et al., 2005), hydrothermal (J. Liu et al., 2003; H.-b. Zhang et al., 2009), mechanochemical (B Nasiri-Tabrizi et al., 2009; C. Silva et al., 2003), spray-drying (Nandiyanto & Okuyama, 2011; R. Sun et al., 2009), sonochemical (Cao et al., 2005; Poinern et al., 2009), and co-precipitation (V. V. Silva et al., 2001; L. Zhang et al., 2005) methods, have been developed to prepare HA particles.

Calcium HA ceramic is usually prepared from apatites obtained through precipitation or hydrolysis under basic conditions and subsequently sintered at 950 °C to 1300 °C (Bonel et al., 1988). Precipitation can be obtained *via* either of the following reactions:

$$Ca(NO_3)_2 + NH_4H_2PO_4 + NH_4OH \rightarrow Ca_{10}(PO_4)_6(OH)_2$$

$$Ca(CH_3COO)_2 + NH_4H_2PO_4 + NH_4OH \rightarrow Ca_{10}(PO_4)_6(OH)_2$$

$$Ca(OH)_2 + H_3(PO_4)_2 + NH_4OH \rightarrow Ca_{10}(PO_4)_6(OH)_2$$
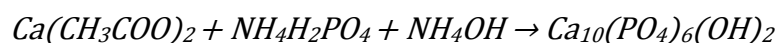
HA ceramic may also be prepared by sintering the products of dicalcium phosphate dihydrate (DCPD, $CaHPO_4 \cdot 2H_2O$), dicalcium phosphate anhydrous (DCPA, $CaHPO_4$), or octacalcium phosphate [OCP, $Ca_8H_2(PO_4)_6 \cdot 5H_2O$] hydrolysis in basic solutions or $CaCO_3$ in phosphate solutions (R. LeGeros, 1988), as in the following reactions.

$$CaPO4 \text{ or } CaHPO4.2H2O + NH4OH \rightarrow Ca10(PO4)6(OH)2$$

$$CaCO3 + NH4H2PO4 \rightarrow Ca10(PO4)6(OH)2$$
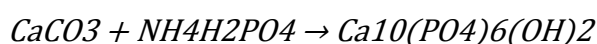
The critical control of reaction pH and reactant concentration is required to obtain HA. In this study, two methods are used to synthesize HA, namely, low-temperature (aqueous precipitation) and high-temperature (hydrothermal) techniques.

2.4.1 Wet Chemical Precipitation Method

Conventional wet chemical precipitation methods are among the most common approaches because these methods are simple, available, and inexpensive raw materials. Combined with low reaction temperatures, this process leads to minimal operational costs. Wet chemical precipitation is essential for manufacturing applications because of scalability. Precipitation method involves mixing reactants in the presence of water at controlled temperature, atmosphere, and pH; this method allows the resulting precipitate to age under continuous stirring for 12 h. Once aged, the precipitate is thoroughly washed, filtered, and dried. Super saturation is key to precipitation. A solution is defined as supersaturated when this solution contains more solute than the desired amount that should be present at equilibrium. Nucleation and crystal growth occur once a solution is supersaturated. This phenomenon occurs when phosphate solution is

titrated in a calcium solution, thereby forming a suspension of precipitated particles. HA powders can result in powder with deviations from stoichiometry (i.e., Ca/P ≠ 1.67), along with additional secondary phase. Experimental parameters, such as reactant concentration, reaction temperature, reaction atmosphere, and reaction pH, should be carefully controlled to avoid the formation of secondary phases during aqueous precipitation. In precipitation, pH is a very important factor to control the properties of precipitates during HA nanoparticle synthesis. The major precipitates in a solution are HA, TCP, DCPA, DCPD, and OCP. The ionization equations of these chemicals in a solution are as follows:

$$HA: 5Ca^{2+} + 3PO_4^{3-} + OH^- \leftrightarrow Ca_5(PO_4)_3OH$$

$$TCP: 3Ca^{2+} + 2PO_4^{3-} \leftrightarrow Ca_3(PO_4)_2$$

$$OCP: 8Ca^{2+} + 6PO_4^{3-} + 2H^+ + 5H_2O \leftrightarrow Ca_8H_2(PO_4)_6.2H_2O$$

$$DCPA: Ca^{2+} + HPO_4^{2-} \leftrightarrow CaHPO_4$$

$$DCPD: Ca^{2+} + HPO_4^{2-} + 2H_2O \leftrightarrow CaHPO_4.2H_2O$$
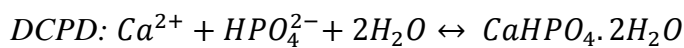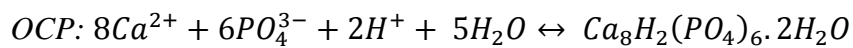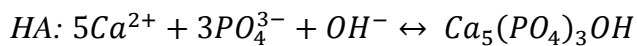
These equations show that a high pH favors HA nanoparticle precipitation. At pH > 8, the solubility of HA nanoparticles is much lower than that of DCPA, DCPD, OCP, and TCP. At pH > 8, the nucleation rate of HA particles increases as pH increases. Crystals nucleate in a short period, and competition among these crystals restricts HA crystal growth, which favors nanoparticle production. In this experiment, pH was controlled between 9 and 11 by adding ammonia (Koutsopoulos, 2002; C. Liu et al., 2001; Mobasherpour et al., 2007; P. Wang et al., 2010).

2.4.2 Hydrothermal Method

Hydrothermal method is used to synthesize materials at high temperature and high pressure by using chemical supersaturated solutions (J. Liu et al., 2003). Hydrothermal processing involves the use of a solvent (with precursor soluble ions), which is heated in a sealed vessel. The main solvent in this process is water. Solvent temperature can be increased to above boiling point because autogenous pressure in a sealed vessel exceeds ambient pressure. Variations in solvent and reactant properties (e.g., solubility) at increased temperature indicate that experimental variables can be controlled to a high degree. With this characteristic, reactions become more predictable because crystal nucleation, growth, and aging can be regulated. Calcination is not required in this method. In low-temperature methods, such as wet chemical precipitation and sol–gel synthesis, post-heat treatment is required to crystallize HA, whereas crystalline HA can be produced in one step *via* hydrothermal and solvothermal syntheses. Yields approaching 100%, relatively low-cost reagents, and short reaction times have also been reported for these processes. Furthermore, HA nanotube, microtube, and nanorod with a micro length are formed (Chandanshive et al., 2013; C. Chen et al., 2011; D. K. Lee et al., 2011; Lester et al., 2013; J. Liu et al., 2003; M.-G. Ma et al., 2008).

2.5 Synthesis of Graphene Nano-Sheet (GNS)

Graphene synthesis can be conducted *via* four different methods: (1) CVD (Eizenberg & Blakely, 1979); (2) scotch tape method involving graphene sheets that are mechanically exfoliated from highly oriented graphite flakes (Novoselov et al., 2004); (3) epitaxial growth of graphene films on an electrical insulating substrate (e.g., Si) (Berger et al., 2006); and (4) chemical reduction of GO derivatives from natural graphite flakes (Stankovich, Piner, et al., 2006). These methods have been described in

several studies since this material was discovered. In the early 1970s, the pioneers of monolayer graphite production through CVD were surface scientists and chemists. In the 1950s and 1960s, extensive studies on aqueous suspensions of monolayer graphite oxide sheets were conducted by (Hans-Peter Boehm et al., 1962). Graphite oxide, which can be used to extract GO sheets through oxidation of natural graphite flakes, was identified as early as the 19th century (Staudenmaier, 1898); Brodie, 1860; Hummers & Offeman, 1958). Ultrasonication, a recently discovered process, can be utilized to exfoliate graphite flakes and generate aqueous suspensions of oxidized graphene sheets with a broad range of physical and mechanical properties (Park & Ruoff, 2009)

2.5.1   Graphene Oxide

Despite the relative novelty of graphene as a material of much interest and great potential (Park & Ruoff, 2009; Tung et al., 2008), GO was used in previous studies of graphite chemistry (Hanns-Peter Boehm & Stumpp, 2007). Brodie, a British chemist, was the first to explore the structure of graphite by investigating the reactivity of graphite flake. In one of the reactions, potassium chlorate ($KClO_3$) is added to graphite slurry in fuming nitric acid (HNO_3) (Brodie, 1859). Brodie determined that the resulting material is composed of carbon, hydrogen, and oxygen, resulting in an increased overall mass of graphite flake. Almost 40 years after Brodie's discovery of the feasibility of graphite oxidation, Staudenmaier (Staudenmaier, 1898) improved $KClO_3$-fuming HNO_3 preparation by adding chlorate in multiple aliquots during the reaction; $KClO_3$-fuming HNO_3 preparation is also improved by adding concentrated sulfuric acid to increase mixture acidity, in contrast to single addition performed by Brodie. This slight change in procedure resulted in an overall extent of oxidation similar to Brodie's multiple oxidation approach; however, this procedure was performed more practically in a single reaction vessel. Almost 60 years after Staudenmaier's study, Hummers and Offeman

developed an alternate oxidation method by reacting graphite with a mixture of potassium permanganate (KMnO₄) and concentrated sulfuric acid (H₂SO₄); as a result, similar oxidation levels have been achieved (Scheme 2.1) (Hummers Jr & Offeman, 1958). Although slightly modified versions have been developed, the three previously described methods are the primary routes of GO formation.

$$KMnO_4 + 3H_2SO_4 \rightarrow K^+ + MnO_3^+ + H_3O^+ + 3HSO_4^-$$

$$MnO_3^+ + MnO_4^- \rightarrow Mn_2O_7$$
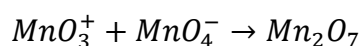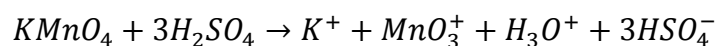
Scheme 2.1 Formation of dimanganeseheptoxide (Mn₂O₇ from KMnO₄) in the presence of strong acid.

2.6 Synthesis of Composite

Single-phase ceramics cannot satisfy the requirements in many application conditions. These ceramics have either low bioactivity or low mechanical strength. Composite materials with properties of each constituted phase should be developed as a good approach to enhance the quality of bone rehabilitation materials. The properties of composite materials can be controlled by adjusting their composition and the percentages of their constituted phases. Table 2.5 lists the mechanical properties of HA and cortical bone. If the mechanical properties of HA could be enhanced, the use of this material in orthopedics is feasible. HA is used as a rehabilitating material of human hard tissue and drug-releasing agent because of excellent biocompatibility and bioactivity. However, low strength and inherent brittleness of this material limits its application to non-load-bearing conditions.

Table 2.5 Typical mechanical properties of HA and cortical bone (Hench et al 1993; Murugan and Ramakrishna 2005; Chen et al 2008)

Mechanical Properties	Hydroxyapatite	Cortical bone
Young`s Modulus (GPa)	40-120	7-30
Compressive strength (MPa)	300	10-230
Flexural strength (MPa)	60-90	50-150
Fracture toughness (MPa.m$^{1/2}$)	<1	2-12

A composite technique was applied to improve the mechanical strength of HA without impeding the biocompatibility and bioactivity of this material for biomedical applications. Composite materials exhibit distinct properties of each constitutive phase. The properties of composite materials can be adjusted to satisfy specific requirements by deriving and applying an appropriate processing technology. Various methods, such as refining HA particle microstructure and incorporating reinforcement phases, have been conducted to improve K_{IC} and flexural strength of HA ceramics. HA composites are classified as follows:

1. HA-ceramic composite (HA-Al$_2$O$_3$, HA-ZrO$_2$, and HA-bioglass) (Cholewa-Kowalska et al., 2009; Curran et al., 2009; Sona Kim et al., 2002; J. Li et al., 1995; Quan et al., 2008; Ravarian et al., 2010).

2. HA-polymer composite (HA-PLLA, PGA, and PPF) (Isago et al., 2014; Muguruma, 2010; Takayama et al., 2012; X. Zhou et al., 2008).

3. HA-carbon nanostructure composite (HA-CNT and HA-GNS) (Fan et al., 2014; Safavi & Sorouri, 2013; W. Wang et al., 2012; A. White et al., 2011; Lv Zhang et al., 2013).

4. HA doped with metal ions (HA/Ag$^+$, Na$^+$, Zn^{2+}, Ni^{2+}, Sr^{2+}, La^{3+}, Y^{3+}, Ta^{5+}, Nb^{5+}) (Dasgupta et al., 2010; Guerra-López et al., 2001; Jadalannagari et al., 2014; Hejun Li et al., 2012; Ligot et al., 2012; Nathanael et al., 2011; Roy et al., 2011; Stanić et al., 2011).

These composites exhibit distinct advantages and disadvantages. For instance, the flexural strength stability of HA ceramic composite, such as Al_2O_3, is poor, although the flexural strength and K_{IC} of composites have been improved significantly. This drawback is caused by differences in thermal expansion coefficients of HA and Al_2O_3; as a result, multiple microcracking occurs after sintering occurs, and flexural strength of composites weakens (Champion et al., 1996). In HA carbon nanostructure composites, such as CNT, CNTs in CP, especially HA, have been applied because these materials exhibit unique mechanical properties; toughness and elastic strength of HA composites have also been improved. However, the widespread use of CNT as fillers is reduced by several issues, such as high cost and heterogeneous dispersion throughout the matrix, which can affect mechanical properties and cytotoxic response in an organic environment. For metal ion-doped HA, stoichiometric HA displays limited reactivity in *in-vitro* (Ducheyne et al., 1993) and *in-vivo* (Schepers et al., 1991) experiments, resulting in prolonged recovery time (Salgado et al., 2004). Low osteogenic capacity and mechanical properties of synthetic HA are caused by the absence of trace elements in natural bone structure (Bandyopadhyay et al., 2006). Therefore, these elements are incorporated in synthetic HA to improve mechanical and biological properties of synthetic HA.

2.6.1 Synthesis of Ions Doped HA

Doping is a very important concept in materials science. In doping, elements (e.g., atoms, ions, and molecules) are deliberately introduced to a specific material to improve material properties. Impure products are formed when foreign elements are

found in a material but not formed *via* a controlled procedure. Accidental impurities are good dopants because these substances enhance material properties or develop new properties. Thus, material doping is a very crucial issue to produce functional materials. A dopant contains lower concentration than the main elements of a material, and this concentration typically ranges from a few ppm to a few percent values (Nedelec et al., 2008).

In synthetic HA, trace elements, such as anions (F^- and CO_3^{2-}) and cations (Ag^+, Sr^{2+}, Y^{3+}, and Ta^{5+}), are implicated in the improvement of structural stability and biological and mechanical performances of bone (Basar et al., 2010; Elena Landi et al., 2004; Ligot et al., 2012; Mardziah et al., 2009; Stanić et al., 2011). Doping of cations results in alterations in structure, microstructure, and surface properties of HA. The valency of dopants can be increased, resulting in enhanced bioactivity of doped HA. A desired level of bioactivity, biocompatibility, solubility, and adsorption properties can be achieved by controlling ions that substitute Ca^{2+}, PO_4^{3-}, and OH^- in the HA lattice structure. However, elements with high valency have been used to dope HA. Ion dopants are synthesized using several methods. Wet chemical precipitation (Paluszkiewicz et al., 2010; Ren et al., 2010; J. L. Xu & K. A. Khor, 2007), sol–gel (K. Cheng, Zhang, & Weng, 2005; K. Cheng, Zhang, Weng, et al., 2005; Kalita & Bhatt, 2007; Mardziah et al., 2009; Miao et al., 2005), and hydrothermal (Aminian et al., 2011; F. Chen, P. Huang, et al., 2011; Nathanael et al., 2011; Sato et al., 2006) methods have been applied using different chemical precursors. For instance, (Nedelec et al., 2008) considered numerous advantages of sol–gel method to prepare and dope ions. Sol–gel process provides materials with good chemical homogeneity, which is a very crucial characteristic. Homogeneous doping produces materials with homogeneous properties, which are a fundamental characteristic of large-scale production and low doping levels. In doping, sol–gel chemistry provides another advantage; in particular, doping is highly

versatile, which causes variation in doping ion type and concentration. However, wet chemical precipitation is commonly used to synthesize monovalent, bivalent, trivalent, and pentavalent ions. Wet chemical precipitation involves the use of different sources of reagents to synthesize doped HA.

2.6.2   Synthesis of HA/Graphene Composite

Homogeneous distribution and efficient use of the secondary phase are some of the major challenges in composite systems. GNS is a nanoscale material. GNS agglomerates because of a high surface energy when this material is added to composites as a reinforcing phase; as a result, this process negatively influences the reinforcing ability of composite materials (Nieto et al., 2012). Several modifications in composite processing techniques have been proposed to improve the dispersing properties of GNS in HA. These techniques and their modifications are discussed in the following subsections. The main goals of these methods are as follows:

(i) To ensure good dispersion and avoid agglomeration of GNS in the HA matrix and

(ii) to provide good interaction of GNS with HA at the interface to ensure good bonding in a composite.

(a) Synthesis of Composite by Chemical Precipitation and Hydrothermal Method

The chemical precipitation of HA on a GNS surface is generally performed by dispersing GNS in a chemical bath where HA is precipitated. HA-coated GNS ensures that HA and GNS are uniformly distributed. GNS is suspended in calcium nitrate/chloride/hydroxide/carbonate bath and then stirred. Afterward, diamonium hydrogen phosphate/phosphoric acid is added dropwise to the bath with vigorous agitation to form HA precipitate on the surface of the suspended GNS. pH (>10) and

precipitation parameters, such as temperature, should be optimized to ensure that HA phase precipitates and $CaHPO_4 \cdot 2H_2O$ or $Ca_3(PO_4)_2$ phases are not formed. GNS is also uniformly distributed in HA precipitate in a powder form *via* chemical precipitation (M. Li, Wang, et al., 2013; Y. Liu et al., 2014; Neelgund et al., 2013; Núñez et al., 2014; Oyefusi et al., 2014). HA precipitate formed on the GNS surface through chemical precipitation contains an amorphous structure that requires posttreatment to transform into a crystalline structure. HA/GNS is formed *via* hydrothermal method to obtain the crystalline structure of HA composite. In this method, GNS agglomeration is prevented using DMF and cetyltrimethylammonium bromide (CTAB) as surfactants to promote good dispersion of GNS under controlled pH of approximately 5 (Fan et al., 2014; Qi et al., 2015). Figure 2.3 shows the GNS/HA composite produced through precipitation and hydrothermal methods.
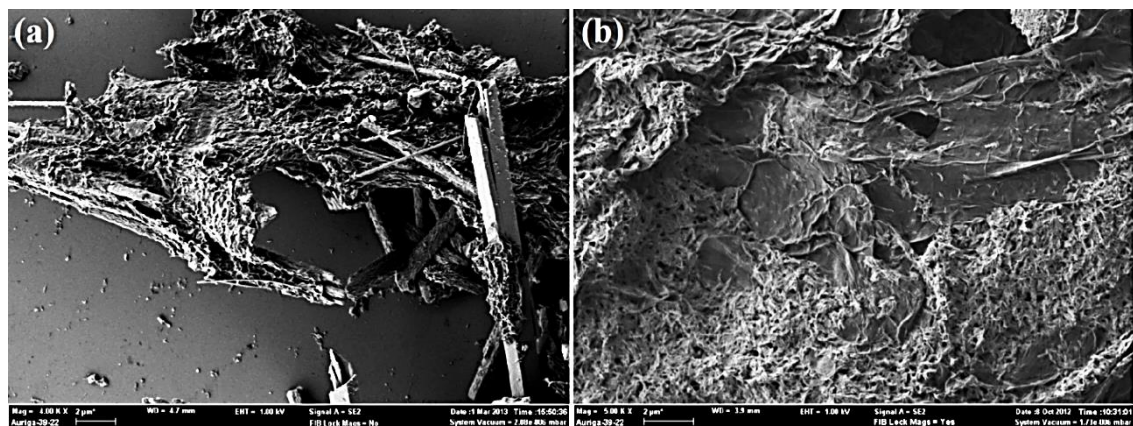
Figure 2.3 GNS/HA composite by (a) hydrothermal (b) chemical precipitation method.

(b) Mechanical Mixing Methods

In mechanical processing of composite powder, HA is physically mixed with GNS *via* mechanical forces. These techniques are also associated with chemical mixing routes to enhance GNS dispersion. Mechanical mixing can be divided into three parts, namely, (i) ball milling, (ii) ultrasonication, and (iii) stirring. Ball milling is one of the commonly used techniques to disperse GNS in HA to prepare composite powders and

fabricate coatings and sintered parts. HA composite synthesized by mixing through ultrasonication is more effective in dispersion than that produced through ball milling (K. Sun et al., 2004).
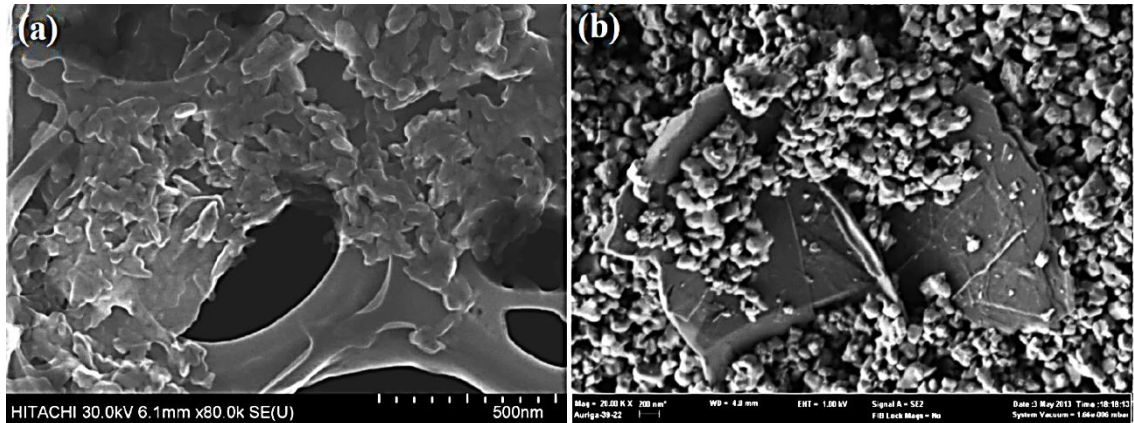
Figure 2.4 Distribution of GNS in HA powder mixed using (a) ultrasonication (b) ball-milling.

Ultrasonication is performed to prepare HA composite precursor by using ambient temperature coating technique, namely, electrophoresis (Janković et al., 2014; M. Li et al., 2014; M. Li, Liu, et al., 2013). Ultrasonication bath is also used to mix GNS with HA to uniformly disperse GNS in precursor and coating stages (Lv Zhang et al., 2013; J. Zhu et al., 2011). Ball milling is performed to mix 2.5wt% GNS in BCP powders to prepare composites *via* sintering, hot pressing, and spark plasma sintering (SPS) routes (Yan Zhao et al., 2013). However, studies have not specifically mentioned the effectiveness of ball milling to disperse GNS in HA. Figure 2.4 presents uniformly distributed GNS in HA powder mixed through ultrasonication and ball milling.

Surfactant used to disperse GNS

A surfactant plays an important role to disperse particles to produce a composite. Nanoparticles exhibit a high surface energy because these particles lack coordinate atoms, and high van der Waals forces induce agglomeration. In a study on different surfactants used to disperse GNS, anionic surfactants, such as sodium dodecyl sulfate,

sodium dodecyl benzene sulfonate, and CTAB, enhance GNS dispersion in DI water (Fan et al., 2014; Y. H. Meng et al., 2006; Walker et al., 2011; Lv Zhang et al., 2013; Yan Zhao et al., 2013). A surfactant facilitates the dispersal of nanomaterials because surfactants exhibit unique properties. A surfactant contains a water-soluble (hydrophilic) end and a water-insoluble (hydrophobic) end. The hydrophobic end of a surfactant attaches to the particle surface, and the hydrophilic end extends to water. An electric layer forms on the particle surface because of the attached surfactant. The electrostatic effect of the charges on a particle surface prevents agglomeration. CTAB, which is an ionic surfactant, was selected in this experiment because CTAB contains a tetrahedral structure similar to that of phosphate anions in HA. Structural similarity causes CTAB to attach to a specific side of HA, which influences particle growth direction.

2.7   Thermal Heating Process and Consolidation of Composite Structure

HA composites are sintered; as a result, dense solid shapes used in orthopedic applications are formed to produce HA powder. In sintering, HA powder is subjected to mechanical compaction and firing until individual particles are combined through diffusion. Compaction and firing, along with chemical and morphological characteristics of starting powder, determine the microstructure of a solid material. The primary considerations during consolidation at high temperature include the control of porosity, maintenance of good dispersion of powder fillers, and simultaneous minimizing of the chemical dissociation of HA to other phases (TCP and CaO). The chemical composition and microstructure are basic aspects governing the mechanical properties of ceramics (Juang and Hon, 1996; Tuan and Guo, 2004; Pramanik et al., 2007; Rahaman, 2007; Zhang et al., 2007). HA composites are combined by sintering after powder is subjected to compaction; this process can be performed through uniaxial

and isostatic pressing. A wide range of sintering temperature from 1050 °C to 1200 °C with a dwell time of 1 h to 3 h is used to consolidate HA/GNS. However, high temperature and prolonged heat treatment enhance the density and crystallinity of HA but increase the probability of HA dissociation. A previous study showed that the density of HA/GNS composite is lower than HA under similar sintering conditions. This finding shows that GNS hold the grains of the matrix apart and prevent closure of pores. However, several sintering methods, such as pressure-less, hot-isostatic/hot-press, microwave, and vacuum sintering, as well as SPS, have been proposed for ceramic densification.

In HA/GNS composites, several sintering methods have been performed to consolidate samples. Zhao et al. reported that BCP/GNS composites are fabricated by hot pressing (HP) screened powders at 1150 °C in a multipurpose high-temperature furnace at a pressure of 30 MPa in an argon atmosphere for 1 h. The GNS contents in the composites were 0, 0.5, 1.0, 1.5, 2.0, and 2.5wt%. Composites with different amounts of GNS exhibit almost the same grain size. In other studies, SPS technique has been used. The use of SPS to produce HA-based composites is advantageous because fine grain structure is retained and HA dissociation is reduced. SPS is a very promising technique to process nanostructured materials because this technique retains fine grain size after sintering is completed. This process is more applicable for ceramics because grain size refinement can simultaneously increase hardness and K_{IC} of the ceramic structure as a consequence of the deflection of a propagating crack and changes in a cracking mode from transgranular to intergranular. In SPS of HA/GNS, temperatures are set in the range of 900 °C to 1150 °C and pressure is set at 40 MPa in vacuum or argon. Systematic studies on the determination of ideal SPS temperature for HA/GNS system have revealed that 1100 °C as optimum sintering temperature. Temperatures

lower than 1100 °C cause poor consolidation with abundant residual pores, whereas temperatures higher than 1100 °C results in excessive grain growth.

2.8 Physical Properties of Composite

Diverse factors affect HA decomposition. The main factor is the stability of HA structure against sintering temperature. The decomposition temperature of HA can be significantly decreased by reducing water partial pressure in sintering atmosphere, lowering Ca/P ratio, and sintering with particulate additives. Dehydroxylation and decomposition are two steps of HA thermal decomposition. At temperatures > 900 °C in air and 850 °C in water-free atmosphere, dehydroxylation to oxyhydroxyapatite (OHA) is accomplished (Ruys et al., 1995; P. E. Wang & Chaki, 1993; J. Zhou et al., 1993). Further dissociation of HA at higher temperatures (1200 °C–1450 °C) is dependent on Ca/P ratio, which is 1.67. At Ca/P < 1.67, HA dissociates into β-TCP (or into α-TCP at high temperatures) and TCP. HA dissociates to CaO when Ca/P > 1.67 (Ruys et al., 1995; A. A. White et al., 2007).

$$Ca_{10}(PO_4)_6(OH)_2 > Ca_{10}(PO_4)_6(OH)_{2-2x}O_x + xH_2O \, gas \quad (OHA)$$

$$Ca_{10}(PO_4)_6(OH)_2 > 2Ca_3(PO_4)_2 + Ca_4P_2O_9 + H_2O \, gas \quad (TCP)$$
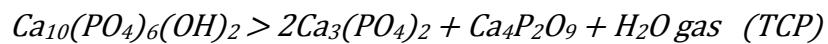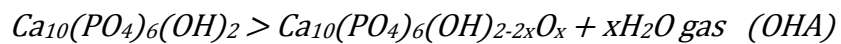
The dissociation of HA into TCP or other phases elicits two major effects on the consolidated structure. (1) The dissociated phases cause problems in densification, thereby significantly reducing structural strength. (ii) The phases formed by dissociation of HA leads to a considerable increase in the dissolution rate at physiological pH, as confirmed by *in-vitro* tests (Jarcho et al., 1976; Radin & Ducheyne, 1992; Ruys et al., 1995). HA dissociates inside a living body, and this process is unsuitable for orthopedic applications. Similar problems are also observed in HA/GNS composite systems. Moreover, H_2O formed by HA dihydroxylation at high temperature can react with GNS

to cause damage to nanosheets. Problems regarding HA phase transformation are largely associated with high-temperature synthesis routes. Phase dissociation is mainly detected by analyzing X-ray diffraction (XRD) pattern of a composite structure. JCPDS PDF No. 09-0432 is used to detect the characteristic diffraction peaks from HA. The presence of dissociated phases is also detected by referring to the JCPDS database, e.g., PDF No. 070-2065 for β-TCP and PDF No. 029-0359 for α-TCP. The reference XRD data of GNS are available in JCPDS PDF No. 23-0064 for graphite. Zhang et al. revealed the effect of 1.0 wt% GNS on minor dissociation of HA into α-TCP caused by rapid processing conditions and low sintering temperature (1150 °C) during SPS (L. Zhang et al., 2013). Zhao presented the XRD patterns of GNP/BCP composites after hot-pressed sintering is performed. Patterns are similar; this result indicates that GNP incorporation does not affect the stability of HA and β-TCP (Y. Zhao et al., 2013).

Kadir reported the XRD patterns of Zn–Ag/HA samples in metal-ion doped HA. In the XRD of 2.5 wt% Zn substitution, a peak related to Zn containing β-TCP was identified, indicating that a small amount of β-TCP may have been formed along with HA as a result of Zn addition. Zn content further increases from 2.5 wt% to 5 wt%; as a result, the intensity of HA peaks evidently decreases, but the intensity of Zn-TCP peaks increases. The formation of TCP is due to the difference in sizes of Ca (0.99 Å) and Zn (0.83 Å) ions, thereby distorting crystal structures (Kadir et al., 2013). investigated the additional phase (CaO) during the synthesis of HA co-doped with zinc and fluoride. The presence of CaO in Zn^{2+}-doped samples is attributed to the replacement of Ca^{2+} ion by Zn^{2+} ion in HA; Ca^{2+} ions detached from the HA structure to form CaO. The XRD spectra of fluoridated samples showed that the CaO phase disappears in 5F and Zn^{2+}–F^- co-doped samples. This phenomenon is possibly because F^- enhances the stability of HA structure (Uysal et al., 2013).

2.9   Mechanical Properties of Composites

In spite of HA exhibits excellent bioactivities, the mechanical properties of this substance are poor. The compressive strength of HA can reach as high as 500 MPa, which is three to six times higher than that of cortical bone (90 MPa to 160 MPa). However, K_{IC} of HA (1.1 MPa·m$^{0.5}$ to 1.2 MPa·m$^{0.5}$) is lower than that of human bone (2 MPa·m$^{0.5}$ to 20 MPa·m$^{0.5}$). Therefore, bulk HA cannot be used as load-bearing implants. Various techniques are used to obtain high mechanical properties of HA materials. Sintering conditions can be altered and composites can be fabricated by adding additives; these processes are two major methods to improve the mechanical properties of bulk HA ceramics. This study mainly aims to use GNS and add metal ion dopants to HA to improve the overall mechanical properties of the composite. In GNS, a high specific surface area of these nanostructures can form and wrap around a HA grain, resulting in increased contact area with the matrix. Therefore, bonding strength between GNS and HA grain can be significantly enhanced; high amounts of energy are required to remove nanofillers from a HA matrix. The rough and wrinkled surface of GNS also helps enhance mechanical interlocking; as a result, load-transfer efficiency between HA matrix and GNS is increased (Lv Zhang et al., 2013). The following subsections present a comprehensive summary of the effect of GNS and metal ion addition on K_{IC}, E, and hardness of composites.

2.9.1   Fracture Toughness

Bones are the load bearing parts of a living body. Thus, they need to possess good fracture toughness (K_{IC}) to prevent cracking and fracture on the application of high and cyclic loading during limb movement and actions. Fracture toughness of dense HA (1 MPa.m$^{1/2}$) is significantly lower than the minimum reported value for cortical bone (2 MPa.m$^{1/2}$) (A. A. White et al., 2007). Thus, to replace bone as an implant, fracture

toughness of HA needs to be improved. GNS and ion doped HA have been explored as additives for improving the fracture toughness of HA based composite parts. The role of GNS in improving the fracture toughness of the composite system can be explained using four main toughening mechanisms (i) crack deflection; (ii) graphene pull-out and (iii) crack branching (iv) crack bridging.

(i) Crack Deflection: When a crack propagates through the matrix and reaches a GNS across its path, the crack gets deflected and absorbs some energy resulting in toughening of the matrix.

(ii) GNS Pull-out: Pulling out of GNS from the ceramic matrix can dissipate energy due to binding and friction and subsequently, leads to toughening.

(iii) Crack branching: Crack branching toughening mechanism was observed in Polycrystalline-graphene composites. Crack branching is very frequently observed toughening mechanisms in all the investigated composites. The origin of this mechanism is the interaction of the propagating crack and GNS with smaller size. The length of the secondary cracks is several microns and the frequency of occurrence of this mechanism is very high.

(iv) Crack Bridging: GNS can act as bridges and restrict the widening of the cracks. GNS bridges require more energy for opening up of the cracks and cause toughening.
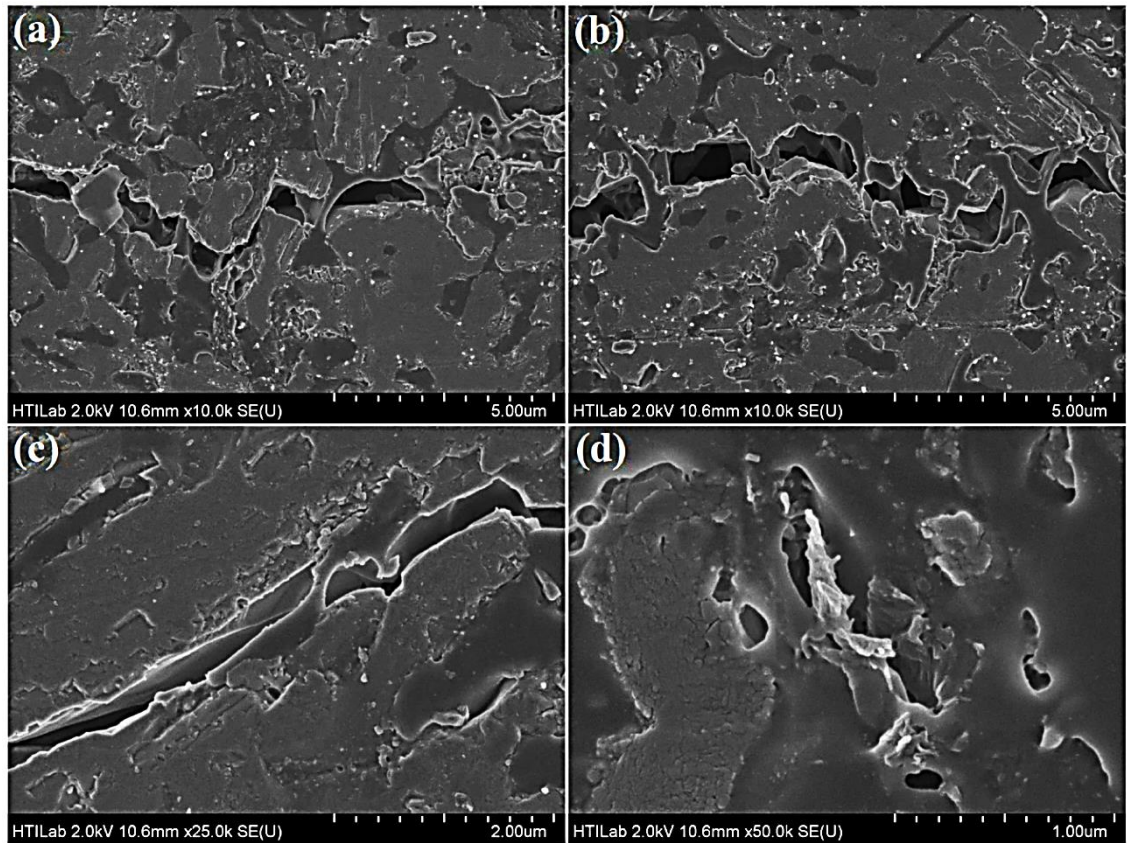
Figure 2.5 Toughening mechanisms in HA/GNS composites: (a), (b) crack deflection and bridging, (c) crack bridging, and (d) rGO Pull-out

Indentation-based technique is primarily used to measure K_{IC}. K_{IC} depends on several factors, including processing route, powder morphological characteristic, and structural type, that is, freestanding or coating (Balani et al., 2009; Y. Meng et al., 2009). Thus, the percentage of improvement in K_{IC} of a HA/GNS system is calculated with reference to K_{IC} of a HA structure (without GNS) reported in the same study. The highest improvement in K_{IC} of 80% was obtained by (Lv Zhang et al., 2013) with 1.0 wt% GNS addition on the sample sintered by SPS. Liu et al. demonstrated that HA/rGO nanocomposites can be synthesized *via* a liquid precipitation approach followed by SPS consolidation. K_{IC} of HA/rGO composites reached 3.94 MPa·m$^{0.5}$, indicating a 203% increase compared with that of pure HA. Crack deflection, crack tip shielding, and crack bridging at HA/rGO interfaces are considered as major strengthening regimes in composites (Y. Liu et al., 2013b). Zhao et al. showed that the mechanical properties of

GNP/BCP composite measured along the direction parallel to the hot-pressing (HP) direction are higher than those measured along the perpendicular direction. Parallel to the HP direction, the composite containing 1.5 wt% GNPs exhibited maximum bending strength and K_{IC} of 151.82 MPa and 1.74 MPa·m$^{0.5}$, respectively, which are approximately 55% and 76% higher than the corresponding values from monolithic BCP (Yan Zhao et al., 2013). Mehrali et al. investigated the effect of GNS on an increase in K_{IC} of calcium silicate fabricated by hot isostatic pressing (HIP) method with the addition of the maximum amount of GNS (1.5%) (Mehrali et al., 2014a, 2014b). Sintering in the presence of any gas is detrimental for HA-based systems. A HA surface can absorb gas that deteriorates the densification of HA; therefore, sintering in vacuum produces the greatest densification. Thus, K_{IC} in this study was improved by 650%, showing a cumulative effect of CNT reinforcement and enhanced densification in the absence of gas. In-depth studies have shown that K_{IC} improves by more than 100%; the effect of uniform dispersion on GNS becomes evident (A. Li et al., 2007).

Miranzo et al. reported that the mixing of SiC/GNS and additive powders, performed through attrition milling in ethanol by using Si_3N_4 grinding media, and powder compositions are sintered through SPS (Miranzo et al., 2013). Fan et al. prepared fully dense Al_2O_3/GNP composites through SPS. GNPs after ball milling are 2.5 nm to 20 nm in thickness and homogeneously dispersed in a ceramic matrix (Y. Fan et al., 2010). Wang et al. confirmed the effect of GNS dispersion on K_{IC} of hot-pressed Al_2O_3/GNS composite. The results indicated that K_{IC} of GNP/Al_2O_3 composite improved by 53%, which was attributed to pulling out and bridging of nanosheets (Kai Wang et al., 2011). Centeno et al. described the production of Al_2O_3/GNP composites through SPS at a very low graphene loading (0.22 wt%). The presence of graphene enhanced K_{IC} of raw alumina by almost 50%; crack bridging was found as the main reinforcement mechanism (Centeno et al., 2013). Liu et al. investigated the effects of

GNPs on the microstructure and mechanical properties of Al_2O_3-based ceramic composites prepared through SPS. Mixing was followed by ball milling in a planetary ball mill. K_{IC} of GNP-reinforced Al_2O_3 ceramic composites increases by 27.20%, which was higher than that of monolithic Al_2O_3 samples with toughening mechanisms, such as pull-out and crack deflection, induced by GNPs (J. Liu et al., 2013). Walker et al. found that K_{IC} of ceramic GNP homogeneously dispersed with Si_3N_4 fabricated through SPS increases by 235% (from 2.8 $MPa \cdot m^{0.5}$ to 6.6 $MPa \cdot m^{0.5}$) at 1.5% GNP volume fraction. Novel toughening mechanisms have shown that GNP wrap and anchor around individual ceramic grains to resist sheet pull-out (Walker et al., 2011). Dusza et al. investigated the influence of the addition of various GNPs as filler on microstructure development and on K_{IC} of Si_3N_4/GNP composites fabricated through ball milling dispersion and HIP sintering. Single and overlapped GNPs are located at the boundaries of Si_3N_4, hindered grain growth, and changed grain shape. Composites exhibited significantly higher K_{IC} than monolithic Si_3N_4, with the highest K_{IC} of 9.9 $MPa \cdot m^{0.5}$ for the composite containing the smallest GNPs.

The main toughening mechanisms attributed to the presence of GNPs and responsible for the enhanced K_{IC} are crack deflection, crack branching, and crack bridging (Ján Dusza et al., 2012). Ramirez et al. reported the two types of Si_3N_4 composites containing graphene nanostructures by using two different graphene sources, namely, pure GNPs and GO layers, produced through SPS. The maximum toughness with 4 vol% of rGO indicated a toughening enhancement of 135% compared with a similar Si_3N_4. For composites with thicker GNPs, only 40% increase in toughness was observed. A large difference in maximum toughness accomplished in both types of composites was attributed to the variations in the characteristics of graphene/Si_3N_4 interface and to the extent of monolayer graphene exfoliation (Ramirez et al., 2014). Govindaraajan et al. reported the preparation of GNP with ZrB_2 ultra-high

temperature ceramic composites reinforced using 2, 4, and 6 vol% GNP by colloidal processing. The investigations were the effect of GNP reinforcement on densification behavior, microstructure, and mechanical properties toughening of composites through GNP pull-out, crack deflection, and crack bridging (Govindaraajan B Yadhukulakrishnan et al., 2013)). Porwal et al. reported well dispersed and fully dense silica-GONP composite powders prepared using a colloidal processing route followed by SPS densification. The present result showed that K_{IC} of composites increased linearly as GONP concentration increased and reached 0.9 MPa·m$^{0.5}$ for 2.5 vol% loading. Various toughening mechanisms, namely, GONP necking, GONP pull-out, crack bridging, crack deflection, and crack branching, have been observed (Porwal et al., 2013).

Shin et al. obtained fully dense yttria-stabilized zirconia ceramics reinforced with rGO fabricated through SPS. K_{IC} significantly improved by 134% accompanied with the toughening mechanisms of pull-out and crack bridging (Shin & Hong, 2014). In metal-ion doped HA, only one case has been investigated to determine the effect of metal ion dopant on K_{IC} of a composite. Basar et al. reported K_{IC} of pure and yttrium and fluoride co-doped HA compared with sintering temperature. K_{IC} obtained at various temperatures and doping amounts range between 1.0 and 2.1 MPa·m$^{0.5}$. The maximum K_{IC} of 2.1 MPa·m$^{0.5}$ was measured for 2.5YFHA sintered at 1100 °C. The lowest K_{IC} of 1.0 MPa·m$^{0.5}$ was calculated for 5YFHA sintered at 900 °C. The sample doped with 2.5% Y^{3+} and 2.5% F^- ions exhibited the optimum K_{IC} (Basar et al., 2010).

2.9.2   Elastic Modulus

E of human cortical bone ranges from 15 GPa to 25 GPa (Rho et al., 1997), but *E* of consolidated monolithic HA is much higher (100 GPa) (Ravaglioli & Krajewski, 1992). *E* mismatch at the bone–implant interface may pose a risk of fracture or

delamination of implant. However, the osseointegration ability of HA creates a strong bond at HA–bone interface, thereby reducing the probability of delamination and fracture. In contrast to K_{IC}, E of HA should not be improved to match that of the bone. However, an increase in E directly influences the improvement in K_{IC} of ceramic-based composite systems. K_{IC} of a brittle ceramic system is mainly estimated from indentation cracking by using Anstis' equation (Anstis et al., 1981), median crack equation by Lawn et al. (Lawn et al., 1980), or Evans' relationship (Evan & Charles, 1976) as follows:

$$Anstis'\ Equation: K_{IC} = 0.016 \left(\frac{E}{H}\right)^{0.5} \frac{P}{C^{1.5}}$$

$$Median\ Crack\ Equation: K_{IC} = 0.018 \left(\frac{E}{H}\right)^{0.5} \left(\frac{a}{C^{1.5}}\right)$$

$$Evans\ and\ Charles\ Equation: K_{IC} = 0.16 H a^{0.5} \left(\frac{c}{a}\right)^{-1.5}, Where\ c/a \geq 3$$

where, K_{IC}: is the fracture toughness,

E: is the elastic modulus,

H: is the hardness,

a: is the half diagonal length of indent and

c: is the radial crack length.

An increase in E is advantageous for enhanced K_{IC}, which is necessary to apply HA/GNS in orthopedics. E of an HA/GNS system is improved because of high E of GNS (1 TPa) (Shen et al., 2013) and good bonding at the HA/GNS interface. Upon application of stress on HA/GNS, a matrix initially deforms because of lower E. If HA matrix exhibits a strong interfacial bonding with stiffer GNS, stress can be effectively transferred from the matrix to the reinforcement. GNS can absorb much higher stress than HA to produce a similar amount of elastic strain. Thus, the resultant elastic strain

generated in the composite structure is reduced compared with HA for the same applied stress; as a result, the effective E of HA/GNS is increased. E increases to 70% with a GNS content ranging from 0.25wt% to 2.5wt%. Homogeneous dispersion of GNS and good HA/GNS interfacial bonding play a key role in increasing E of the composite. Zhang et al. measured E of 1.0 wt% HA/GNS composite and determined 40% of improvement compared with pure HA (Lv Zhang et al., 2013). Li et al. prepared GO/HA and CS-GO/HA nanocomposites and found that E of nanocomposites increases because of the reinforcing effects of GO on HA from 5.55 GPa to 19.09 GPa compared with HA (M. Li et al., 2014). Janković et al. reported the electrophoretic deposition of HA/GNS composite on Ti as E increases by approximately 50% compared with pure HA coating (Janković et al., 2014).

In another case, Liu et al. showed that E of HA-rGO SPS pellets increases as a function of rGO content and rGO content in composites increases. E of HA/rGO composite is enhanced by 47.6%(Y. Liu et al., 2013b). Mehrali et al. reported that E elasticities of CS/rGO and GNP composite in calcium silicate increase by 52% and 11%, respectively, compared with that of pure CS. In metal ion-doped HA, the effect of different ions on E of composites has been investigated (Mehrali et al., 2014a, 2014b). Yatongchai et al. investigated the effects of two strontium (Sr) additions, particularly 5% and 10% of total Ca content, on phase assemblage and Weibull statistics of HA and compared the results with those of undoped HA (Yatongchai et al., 2013). Yatongchai et al. further reported that Weibull modulus is relatively independent of the porosity of undoped HA samples. In addition, 5% Sr-HA samples showed a slight increase in Weibull modulus with porosity, indicating a possible relationship between these parameters. However, 10% Sr-HA samples showed the highest Weibull modulus with approximately 15 at all sintering temperatures (Yatongchai et al., 2013). Xu et al. found that E of sintered spray-dried HA increases as the amount of doping silica increases

from 1 wt% to 5 wt%. *E* also increases by approximately 15% from 84 GPa to 100 GPa compared with that of HA without silica (approximately 89 GPa) (J. Xu & K. A. Khor, 2007).

2.9.3 Hardness

The addition of carbon nanomaterials (CNMs), such as CNT and GNS, influences the hardness of HA-based composite. The higher stiffness of CNM provides a strengthening effect on HA matrix, which hampers plastic deformation. A significant reduction in pile up at the edge of nano-indents as CNM content increases corresponds to enhanced resistance to plastic deformation (Y. Chen et al., 2006). Grain boundary pinning and structure refinement by CNM also help enhance hardness and K_{IC} (J. Wang & Shaw, 2009; Xu et al., 2009). Vickers' hardness measurement and instrumental nanoindentation technique have been performed to quantify the hardness of HA/CNM composite. Absolute hardness values differ between nanoindentation and Vickers' experiments because of great differences in applied load, tip geometry, and measurement length scale (Lahiri, Singh, et al., 2011). Microindentation test uses a larger volume of an indenter and a higher volume fraction of GNS than nanoindentation test (Mehrali et al., 2014b).

Zhang et. al reported that Vickers' hardness of 1.0 wt% GNS/HA composite in HA/GNS improves by 30% compared with pure HA because of good bonding strength between GNS and HA grain, which significantly enhances hardness (Lv Zhang et al., 2013). Wang et al. found that the hardness of HA increases from 367.59 ± 25.76 MPa to 624.32 ± 11.77 MPa compared with HA because GO matrix strongly interacts with HA nanoparticles. The addition of GNS improves the hardness of HA because of matrix strengthening and grain size refinement; both of these processes hinder plastic deformation. Zhao et al. found that the hardness of BCP/GNP along the direction

parallel to the HP direction is higher than that measured along the perpendicular direction. Zhao et al. reported that hardness decreases as GNP increases (M. Li, Wang, et al., 2013). Mehrali et al. reported an increase in hardness in lower GNS content in other cases, such as CS/GNS composites, because of matrix strengthening and grain size refinement; these processes prevent plastic deformation (Mehrali et al., 2014a, 2014b). Thus, the addition of GNS beyond ineffectively enhances hardness of a composite structure. Similar to E, agglomeration and weak interface cause a slight increase or decrease in hardness with GNS addition (Centeno et al., 2013). Kalita et al. performed Vickers' hardness test on metal ion-doped HA, particularly pure and doped nanocrystalline-sintered HA structures. The results of our hardness test showed that the surface hardness of nanocrystalline HA ceramics is influenced by the presence of magnesium and zinc as dopants during powder synthesis. Furthermore, 20% and 6% improvement of the aforementioned composition because of an increase in the density of the sintered ceramics (Kalita & Bhatt, 2007).

Basar et al. reported the effect of co-substitutions of Y^{3+} (2.5, 5, and 7.5 mol%) and F^- (2.5 mol%) ion-doped HA on microhardness. In addition, 7.5YFHA sintered at 1300 °C yielded the highest microhardness of 5.9 GPa; by contrast, pure HA exhibited microhardness of 4.5 GPa. Furthermore, 7.5YFHA with the highest density (96.6%) exhibited the greatest microhardness with a grain size smaller than those of the other HA samples (Basar et al., 2010). Curran et al. found that the hardness of microwave-sintered (MS) and conventional-sintered (CS) Sr-HA samples increased as Sr content increased (Curran et al., 2009). They reported that differences in relative densities and grain sizes between MS and CS samples may elicit a regulatory effect on differences between hardness values of the two samples. The hardness values of both samples were dependent on the level of open (surface) porosity because hardness technique is a surface technique; surface porosity is effectively filled because an indenter affects the

surface. In MS samples, grain size also determines hardness; therefore, an increase in grain size causes an increase in hardness. Xu et al. investigated the effect of silica-doped HA on the decrease in hardness of bulk samples compared with pure HA. The relatively low hardness obtained from doped samples was mainly attributed to low bulk density of materials. Pore formation and phase transformation of HA into β-TCP mainly contribute to reduced densities (J. Xu & K. A. Khor, 2007). Joshy et al. reported that hardness increases gradually as the amount of incorporated La^{3+} ions in L5HA (50 mM La^{3+}) increases by 14% (Ahymah Joshy et al., 2011).

2.10 Biological Properties of Composites

2.10.1 *In-vitro* Bioactivity

The ability of apatite to precipitate on any surface during stimulated body fluid (SBF) immersion is a preliminary indicator of the capability of this substance to be integrated with new bone *in-vivo.* The suitability of SBF immersion test as an indicator of biocompatibility can be justified through a statement by Kokubo, who invented SBF, and Takadama, who conducted an "*examination of apatite formation on a material in SBF used to predict in-vivo bone bioactivity of a material, and the number of animals used and the duration of animal experiments can be reduced remarkably by using this method*" (Kokubo & Takadama, 2006). New bone integration on an orthopedic surface is closely related and governed by osteoblast attachment, proliferation, and differentiation, which predict the mineralization of apatite on an orthopedic surface (Pan et al., 2010). Thus, the behavior of an osteoblast is also crucial to determine the biocompatibility of an orthopedic surface along with apatite formability. Studies have shown that GNS composite surfaces are suitable for apatite precipitation. Mineralization proceeds in three stages: (1) dissolution-controlled stage, (2) precipitation-controlled stage, and (3) bone-like apatite formation. In the first stage, dissolution of phosphate

and calcium ions occurs. However, the process and kinetics of HA deposition on composites are affected by surface area and negative surface charges. In HA/GNS composite, apatite precipitation ability of HA/GNS composite surfaces has also been investigated. Janković et al. reported a seven-day incubation period for newly formed apatite layer containing plate-shaped HA crystals on HA/Gr composite surface coating on Ti when this material is immersed in standard SBF. They found that the morphological characteristic of mineralization product varies remarkably with the incorporation of Gr into the HA matrix. Curled, plate-shaped apatite evidently forms on HA/Gr composite coating (Janković et al., 2015).

Fan et al. demonstrated that a thick and dense apatite layer gradually forms on the surface of coated HA/GNS immersed in SBF for 7 d. They revealed a slower initial precipitation rate in the presence of GNS; this parameter subsequently increases with various morphological characteristics from granular to plate-like form (Fan et al., 2014). Zhang et al. found that apatite layer on 1.0wt% GNS/HA composite is thicker than that on pure HA after 7 d of immersion in SBF. The results indicated that the mineralization area on pure HA is mainly localized near and/or inside pores; by contrast, mineral deposit ultimately influences the whole surface of a GNS/HA composite (L. Zhang et al., 2013). Conversely, the morphological characteristic of a mineralization product varies remarkably when GNS incorporated into a HA matrix. Short needle-shaped apatite is formed on pure HA sample, whereas curled sheet-shaped apatite is formed on GNS/HA composites. These findings sufficiently indicate that incorporation of GNSs into HA matrix facilitates the formation of bone-like apatite on GNS/HA composites. *In-vitro* studies on HA/GNS systems have shown that the presence of GNS in HA is biocompatible and advantageous in some aspects. Joshy et al. investigated the bioactivity of La-doped HA as a metal ion-doped HA by immersing pellets in SBF solution. After pellets are immersed in SBF, the formation of platy apatite crystals of

HA is transformed to spherical apatite deposition because of bioactivity(Ahymah Joshy et al., 2011). Medvecký et al. reported that the total Mn content of up to 0.25 wt% in HA prepared by precipitation does not influence the growth rate of HA particles in SBF solutions. However, a high Mn concentration on the surface of HA particles after ion exchange rapidly reduces the growth rate of HA in SBF solutions (Medvecký et al., 2006). Cox et al. indicated the presence of apatite growth on the surface of all substituted (Sr, Mg, and Zn) and pure HA samples immersed in SBF for 28 d; a positive result indicates bioactivity (Cox et al., 2014). Therefore, interferometry results may not be directly correlated with increased apatite growth because of a combination of factors that may influence surface roughness of substrates; as such, these results cannot be reliably used as a quantitative tool. Moreover, the formation of bone-apatite observed on AgHA coating during immersion in SBF suggested a favorable biological response of AgHA. The presence of Ag ions do not affect the interaction of ions in SBF to form bone-apatite onto AgHA (Y. Chen et al., 2010; Noda et al., 2009).

2.10.2 *In-vitro* Biocompatibility

Zhu et al. performed the first study on osteoblast cell growth on spark plasma-sintered HA/2 wt% GNS sample. Cell culture and MTT assay results demonstrated that GN addition impeded osteoblast cell adhesion and proliferation on HA (J. Zhu et al., 2011). Ma et al. reported that the cytocompatibility of as-prepared PLA/HA/GO fibrous membrane may be estimated by culturing MC3T3-E1 cells and determining the corresponding cell adhesion and differentiation capability. They confirmed that PLA/HA/GO nanocomposite fibrous membrane created an appropriate environment of the seeding and proliferation of MC3T3-E1 cells (H. Ma et al., 2012). Zhang et al. found that osteoblasts uniformly covered the surface of GNS/HA composites as a confluent layer compared with separate islands formed on pure HA surface. Osteoblasts

on the surface of each sample are elongated and flat with a good spread; this finding strongly indicates that the added graphene nanosheets elicited a slight negative effect on osteoblasts spreading on HA sample because these materials exhibit excellent biocompatibility. The difference in the number of adherent osteoblasts illustrated that nanosheets provide composites with an optimal surface for osteoblast adhesion. The added nanosheets can be detected by osteoblasts as extra suitable locations for adhesion; as a result, osteoblast adhesion on GNS/HA composites (L. Zhang et al., 2013). Li et al. investigated the *in-vitro* cytotoxicity of the prepared nanocomposites (GO/HA and CS-GO/HA) through a CCK-8 assay on murine fibroblast L-929 and human osteoblast-like MG-63 cell lines. Both nanocomposites yielded high cell proliferation rates of both cell lines; CS-GO/HA could provide significantly higher cell viability and alkaline phosphatase activity than GO/HA composite (M. Li, Wang, et al., 2013).

Liu et al. also reported the enhanced proliferation of osteoblast cells on rGO-containing HA composites. In ALP activity, ALP expression level on HA/1.0 wt% rGO composites is approximately twice that on pure HA. The proliferation and attachment of osteoblast cells on the surface of HA/GNS composite coating are also reported. The presence of GNS in HA improves bone cell proliferation. Viability assessment also reveals that the percentage of live cells increases in the presence of GNS (Y. Liu et al., 2013a). Li et al. reported that the presence of GO fillers can promote the proliferation of L929 cells and MG63 cells in 2GO/HA-coated samples compared with 5GO/HA-coated samples. Superior (approximately 95% cell viability of 2 wt% GO/HA) or comparable (80% to 90% cell viability of 5wt% GO/HA) *in-vitro* biocompatibility is observed compared with HA-coated and uncoated Ti substrate (M. Li et al., 2014). Liu et al. found that the filopodia of osteoblast cells likely move to and become anchored by GNS. This phenomenon presumably accounts for the enhanced spreading and subsequent proliferation of cells on GN-containing coatings (Y. Liu et al., 2014). Fan et

al. found that GNS/HA nanorod composite containing 40 wt% HA showed higher osseointegration ability with surrounding tissues, better biocompatibility, and more superior bone cellular proliferation induction compared with pure GO and HA (Fan et al., 2014). The following factors possibly enhance proliferation and viability of osteoblast on HA/GNS composite surface:

(i)   attachment of proteins on a GNS surface from a cell culture medium;

(ii)   unique porous structure and high surface area of GNS;

(iii)   higher porosity content of HA/GNS composite; and

(iv)   bioactive nature of GNS.

In metal ion-doped HA, bioactivity and biocompatibility of HA doped with metal ions are enhanced compared with those of pure HA. The potential of Zn-substituted HA as a material to reduce resorptive activity; thus, long-term bonding of implant to bone is observed. ZnHA inhibits osteoclast-like cell formation. In this study, osteoclast formation and resorption are reduced, suggesting that ZnHA may be a beneficial alternative to unsubstituted HA as an implant coating (Kalita & Bhatt, 2007; Shepherd et al., 2014; Thian et al., 2013). Other studies have also reported that Sr concentrations in the range of 3 to 7 atom% significantly stimulate osteoblast activity and differentiation, as shown by increased ALP, CICP, and OC production compared with pure HA. Cell culture test results indicated that Sr/HA shows good biocompatibility with human osteoblasts. Compared with HA, Sr/HA promotes OPC1 cell attachment and proliferation; Sr/HA elicits no deleterious effects on ECM formation and mineralization. Sr doped HA can be employed to prepare biomaterials that can promote osseointegration and bone regeneration, as well as prevention and repair local bone loss (Capuccini et al., 2009; Elena Landi et al., 2007; Xue et al., 2006). (Basar et al., 2010) also investigated the effect of Y^{3+} and F^- co-doping on pure HA on cell proliferation.

Basar et al. found that cells highly adhere and proliferate on large grain-sized pure HAs or when these cells are doped with 2.5% or 5% yttrium and 2.5% fluoride (Basar et al., 2010).

.

CHAPTER III: MATERIALS, METHODS AND PROCEDURES

This chapter provides a detailed account of the synthesis methods of HA and its composites as well as its characterization for physical, mechanical and biological properties.

3.1 Synthesis of Graphene Oxide

The graphite flakes used in this project were purchased from Ashbury Inc. The sulfuric acid (H_2SO_4, 98%), phosphoric acid (H_3PO_4, 98%), potassium permanganate ($KMnO_4$, 99.9%), hydrogen peroxide (H_2O_2, 30%) and hydrochloric acid (HCl, 37%) were purchased from Merck (Malaysia). All of the aqueous solutions were prepared using double distilled water (ddH_2O). The GO was prepared from the graphite flakes using a simplified Hummers' method (Lim et al., 2011). Initially, 360 mL of H_2SO_4 and 40 mL H_3PO_4 were added to a beaker containing 3 g of graphite at room temperature. Then, 18 g of $KMnO_4$ was gradually added to the mixture. The mixture was stirred for three days to ensure the complete oxidation of the graphite. Finally, the suspension was cooled and diluted with 400 mL of ice water. Afterwards, H_2O_2 (30%) was added until the gas evolution ceased. This is performed to ensure the reduction of the residual permanganate into soluble manganese ions. After the synthesis, the GO suspension was washed with dilute 1 M HCl and ddH_2O repeatedly until a pH of 5 was reached. The resulting product was separated from the mixture by using a centrifuge spinning at 11000 rpm. Figure 3.1shows the flowchart synthesis of graphene oxide as follows:
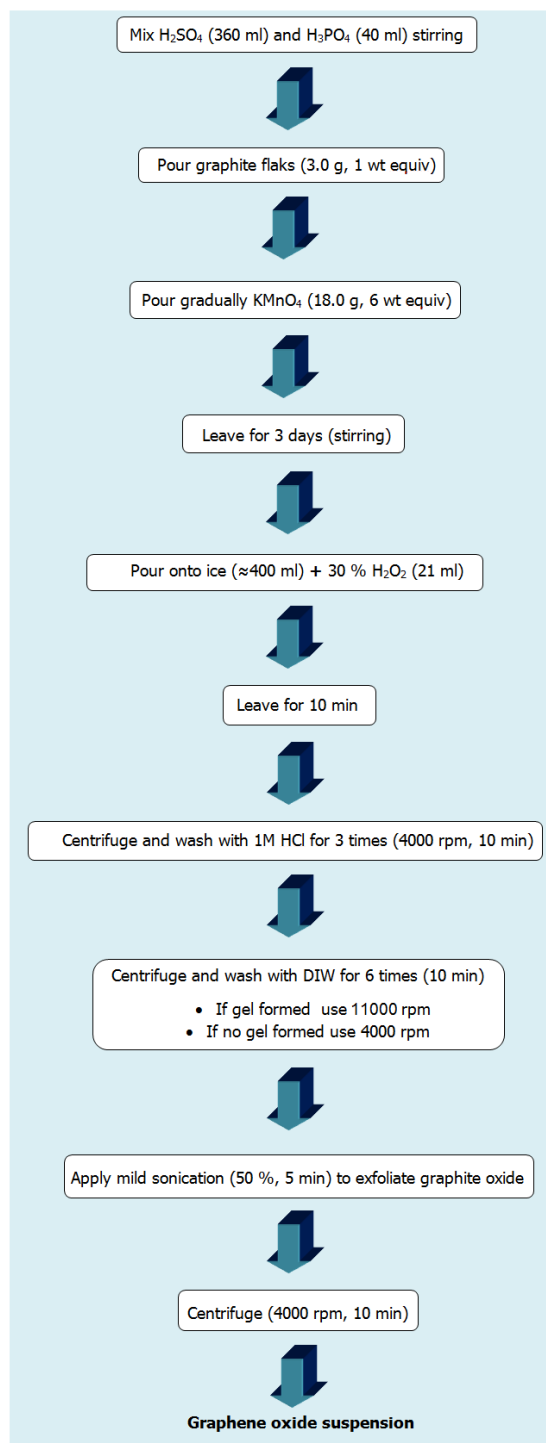
Figure 3.1 Flow chart of synthesis of Graphene oxide

3.2   Synthesis of Composite Powders

Ethylene glycol (EG, 68%), isopropyl alcohol (60%) and Ammonium hydroxide (NH$_4$OH, 28%) were purchased from Merck (Malaysia). Calcium nitrate tetrahydrate Ca(NO$_3$).4H$_2$O, Calcium chloride (CaCl$_2$), nickel (II) nitrate hexahydrate Ni(NO$_3$)$_2$.6H$_2$O and ammonium dihydrogen orthophosphate (NH$_4$H$_2$PO$_4$.6H$_2$O) were

all purchased from Sigma Aldrich (Malaysia). The N,N-Dimethylformamide (DMF, 99.99%) was purchased from J. T. Baker Company. Cetyl trimethyl ammonium bromide (CTAB) was selected as the dispersion media. Graphene nanoplatelets (GNP) were obtained from XG Sciences, Lansing, MI, USA. All the chemicals were of analytical grade and used without further purification. All of the aqueous solutions were prepared using ddH$_2$O.

3.2.1 Synthesis of Nanotube Hydroxyapatite (nHA)-Reduced Graphene Oxide (rGO) Composite

The nHA was synthesized using the method described by Feng Chen *et al.* (F. Chen, Y.-J. Zhu, et al., 2011). To synthesize the nHA-rGO composites, 8.2 mg of GO was dissolved in 10 mL water using ultrasonication for 1 h to obtain a yellow-brown uniformly dispersed solution. Initially, 3.33 mL of 0.24 M CaCl$_2$ was dissolved in 3.33 mL of EG. Afterwards, 0.82 mg mL^{-1} of the GO suspension was added drop-wise into the solution *via* magnetic stirring for 60 min to obtain a homogenous dispersion. Similarly, 3.33 mL of 0.2 M NH$_4$H$_2$PO$_4$ was dissolved in another beaker with 3.33 mL of EG. The second solution was added drop-wise into the first solution and stirred for another 30 min. Finally, 27 mL of DMF was added to the mixture at a rate of 4 mL min^{-1}. The final suspension was transferred to a 50 mL Teflon-lined stainless steel autoclave for hydrothermal reaction at 200 ℃ for 24 h. It was expected that the concurrent reduction of GO to rGO and *in-situ* synthesis of the nHA-rGO composite may be achieved during the hydrothermal process. The as-synthesized nHA-rGO samples with 0.0, 0.5, 1.0 and 1.5 wt% rGO, named HG-0, HG-1, HG -2 and HG-3 were separated by spinning in a centrifuge, washed five times with ddH$_2$O and dried in a vacuum oven at 60 ℃ for 24 h.

3.2.2 Synthesis of Ni-doped HA with Graphene Nanoplatelets (GNPs) Composite

Ni-doped HA (0, 3 and 6 wt%) was synthesized at room temperature using the continuous precipitation method. The desired amounts of $Ca(NO_3).4H_2O$ and $Ni(NO_3)_2.6H_2O$ were mixed to produce the nitrate solution. This step was followed by the drop-wise addition of $(NH_4)H_2PO_4$ solution to the nitrate solution under vigorous magnetic stirring. The pH of the solutions was adjusted with the addition of NH_4OH to 10 and 11 for $(NH_4)H_2PO_4$ and nitrate solution, respectively. The suspension was allowed to settle for 24 h to remove the supernatant. The precipitate was filtered and washed six times with doubly deionized water (DDI). The obtained powder was dried at 100 °C for 24 h and calcined at 900 °C for 1 h. Finally, the powder was ball milled at 300 rpm in a planetary ball mill (PM 100, Retsch, UK) for 2 h to produce the fine powder. The respective compounds were labeled HA, Ni3 and Ni6. The appropriate quantities of Ni6 powders and GNPs were separately dispersed in DDI with 1 wt% CTAB and 1h sonication. To fabricate the composites, dispersions of GNPs and powders with concentrations of 0.5 wt%, 1 wt%, 1.5 wt% and 2 wt% GNPs were prepared by sonication for 1 h followed by planetary ball milling with a zirconia ball and a rotational speed of 400 rpm for 15 h to obtain a good degree of mixing. The milled slurry mixture was dried in an oven at 90 °C for 24 h.

3.2.3 Free Standing HA and its Composite Synthesis: Hot Iso-Static Pressing (HIP)

The green samples were uni-axially pressed at 250 MPa into discs using a 5 mm diameter steel die. The HIP was performed at 1150 ℃ in a high purity argon gas atmosphere at 160 MPa for 1 h. The heating and cooling rates did not exceed 5°C min^{-1}. The dimensions of the sintered samples were 5 mm in diameter and 3 mm in thickness. Finally, the sintered samples were molded with epoxy before mechanical property

testing. The surfaces of the sintered samples were polished in a single direction with 600, 1200 and 2000 grit SiC paper. The final polishing was performed with 9, 3 and 0.5 μm polishing compounds to obtain a consistent surface roughness for all of the samples.

3.3 Physical and Chemical Characterization

The relative density for each composition was measured using Archimedean's method using 3.16 g cm^{-3}, 3.07 g cm^{-3} and 2.2 g cm^{-3} for HA, β-TCP and GNPs, respectively. The surface morphologies of the disc compacts were characterized using field-emission scanning electron microscopy (FESEM, FEI Quanta 200F). Energy dispersive X-ray spectroscopy (EDS) with an EDS system attached to the FESEM instrument was used to investigate the elemental composition of the samples. Fourier-transform infrared spectroscopy (FT-IR) was performed using a Perkin Elmer System series 2000 spectrophotometer (USA) with a frequency range of 400-4000 cm^{-1}. An X-ray diffractometer (PANalytical Empyrean) with *CuKα* (λ=1.54178 Å) radiation was used for the phase analysis of the samples. Raman spectroscopy (Renishaw in *Via* Raman Microscope) was performed to characterize the composite samples using 514-nm laser excitation, 0.8-mW laser power and 20-μm spot sizes.

3.4 Mechanical Characterization

The analysis of the mechanical properties of the sintered samples was carried out using the indentation method. A nano-mechanical test system (Micro materials Ltd. Wrexham, U.K.) was used to evaluate the mechanical properties (particularly the modulus of elasticity) of the prepared samples through nano-indentation experiments. The samples subjected to nano-indentation tests were 5 mm in diameter and 3 mm in thickness. A maximum load of 10 mN was applied to the samples using a Berkovich diamond tip (radius of 20 nm) in load control mode with a dwell time of 10 s and

indentation velocity of 3 nm s^{-1}. A Vicker`s micro-indentation instrument (AVK-C2, Mitutoyo, Kawasaki, Japan) was used to determine the hardness of the samples by applying a 1 kg force for 10 s on the polished pellets. The indentation fracture toughness of the samples was calculated using diagonal crack lengths produced at the indentation corners from the micro-indentation tests. Fracture toughness values were evaluated by the Antis`s equation:

$$K_{IC} = 0.016 \left(\frac{E}{H}\right)^{0.5} \left(\frac{P}{C^{1.5}}\right)$$

where E is the elastic modulus obtained from nano-indentation test, H is the Vickers hardness (GPa), P is the applied load (N) and c is the diagonal crack length (m). The fracture toughness and hardness values are averaged for three samples with five indents per sample.

3.5   Biological Characterization

3.5.1   Mineralization in Simulated Body Fluid (SBF)

The bioactivity of the sintered samples (with a thickness of 3 mm and a diameter of 5 mm) was evaluated by examining the formation of bone-like apatite on the samples in simulated body fluid (SBF) solution. The sintered samples were soaked in SBF with pH (7.4) and ion concentrations (Na$^+$ 142.0, K$^+$ 5.0, Mg^{2+} 1.5, Ca^{2+} 2.5, Cl$^-$ 147.8, HCO$_3^-$ 4.2, HPO$^{2-}_4$ 1.0, SO$^{2-}_4$ 0.5 mM) nearly identical to those in human blood plasma. As brief, the SBF was prepared by dissolving reagent-grade mixtures of CaCl$_2$, K$_2$HPO$_4$ .3H$_2$O, KCl, NaCl, MgCl$_2$.H$_2$O, NaHCO$_3$ and Na$_2$SO$_4$ in distilled water and buffering at pH 7.4 with tris(hydroxymethyl)aminomethane and hydrochloric acid (HCl). The as sintered samples were soaked in SBF at 37 °C in a humidified atmosphere containing 5% CO2 for 7 days at a surface-area-to volume ratio of 0.1 cm^2/mL. The SBF solution was renewed once in 2 days. After 7 days, they were removed from SBF, gently rinsed

with distilled water, and dried in vacuum at 80 °C. Changes in the surface morphologies of samples after soaking in the SBF were characterized by FESEM equipped with EDX.

3.5.2 *In-vitro* Bone Cell-Material Interactions

The *in-vitro* cytotoxicity behavior and biocompatibility of the doped, undoped HA and composite samples were evaluated after 1, 3, and 5 days of incubation using human osteoblast cell lines (hFOB 1.19SV40 transfected osteoblast) that were provided by the American Type Culture Collection (ATCC, Rockville, MD). The cells used were derived from an immortalized osteoblastic cell line, established from DME/F12 solution (Hyclone, Utah, USA) supplemented with a 10% human fetal bovine serum (Gibco, NY, USA), 100 U mL^{-1} penicillin and 100 µg mL^{-1} streptomycin in 5% CO_2 and 95% air atmosphere at 37 °C in an incubator. All the samples were sterilized by autoclaving at 121 °C and 15 atm for 15 min before the cell culture experiment. The cells were then seeded onto samples and placed into the wells of a 24-well plate. The initial cell density was 1×10^4 cells mL^{-1}.

3.5.3 Cell Proliferation Using MTT Assay

The methyl thiazole tetrasodium (MTT) assay (Sigma, St. Louis, MO, USA) was performed for 1, 3 and 5 days of incubation to determine the hFOB cell proliferation. Triplicate samples per group were evaluated, and three data points were measured from each sample. An MTT solution of 5 mg ml^{-1} was prepared by dissolving MTT in PBS and was filter-sterilized using a filter paper with a 0.2-µm pore size and stored at 4 °C. Then, 20 µl of the MTT solution was added to each sample in the 24-well plates. The cells were then incubated for 4 h at 37 °C in a humid atmosphere with a CO_2 concentration of 5%. After 4 h of incubation, 100 µl of solubilization/stopping solution was added to each well. Blank and control groups were established to calibrate the

cellular survival rate. Only the culture media were added in the blank group, whereas cells and culture media without samples were added in the control group. The optical density (OD) was measured using a 96-well plate reader (TECAN, Mannendorf, Switzerland) and read by a plate reader at 570 nm. Triplicate samples were used in all the experiments to ensure reproducibility. The data from the MTT assay are presented as means or plotted as ± SD. Statistical analysis was performed on the MTT assay results using one-way analysis of variance (ANOVA) and a Tukey-Kramer post hoc test using SPSS 19.0; a p-value less than 0.05 was considered significant.

3.5.4   Cell Morphology

The cell morphology was assessed using FESEM observation after 1, 3 and 5 days of incubation. Cultured samples for SEM observation were rinsed with 0.1 M phosphate-buffered saline (PBS) and fixed with 4% glutaraldehyde for 2 h at room temperature. The drying procedure was as follows: the fixed samples were dehydrated in an ethanol series 40%, 50%, 60%, 70%, 80%, 90% and 100% three times followed by the addition of 0.5 mL of hexamethyldisilane (HMDS) to each well to maintain the original morphology of the cell. The dried samples were then platinum coated and examined under a FESEM.

3.5.5   Confocal Laser Scanning Microscopy

The samples were washed with 1×PBS before staining with 100 μg/ml acridine orange (Sigma Aldrich) for 5 min at room temperature. Excess stain was removed by washing twice with 1×PBS for 10 min. The stained cells were then analyzed using confocal microscopy (Leica TCS-SP5 II, Leica Microsystem and Mannheim, Germany), and the images were processed with Leica LAS AF software.

4.1 Mechanical Properties and Biomedical Applications of a Nano-tube Hydroxyapatite-reduced Graphene Oxide Composite

4.1.1 Microstructural and Physical Properties

Figure 4.1 shows the hydrothermal formation mechanism of the nHA-rGO composite. In the first step, a carboxyl (-COOH or COO$^-$) group on the surface of the GO strongly absorbs Ca^{2+} ions by an electrostatic interaction. This phenomenon increases the rate of HA nucleation on the surface of GO. The existence of EG can initially decrease the diffusion of Ca^{2+} and HPO_4^{2-} ions at room temperature. However, as the temperature increases, the viscosity of the EG rapidly decreases and may facilitate anisotropic growth on the HA nano-sheet. This is notable because under hydrothermal conditions at 200°C for 24 h, nano-sheets of HA and GO can be converted to sheets with brush-like ends. The evolution process from the brush-like ends to HA nano-wires or nano-tubes may be explained by a dissolution/re-precipitation process under hydrothermal conditions. At this early stage, the brush-like ends are partially dissolved in the solution and may create a primary HA nano-crystal under hydrothermal conditions.

Other researchers believe that this self-assembly process is the reason that assembled nano-tubes or nano-wires have been observed in HA during the nucleation of a primary nano-crystal. In this case, it is notable that the DMF also alleviates the agglomeration of the rGO nano-sheets (Shah et al., 2013). The process is described by the following relations:

$$Nanosheet\ brush\text{-}like + OH^- \rightarrow Ca^{2+} + PO_4^{3-} + H_2O,$$

$$5Ca^{2+} + 3PO_4^{3-} + OH^- \rightarrow Ca_5(PO_4)_3OH$$
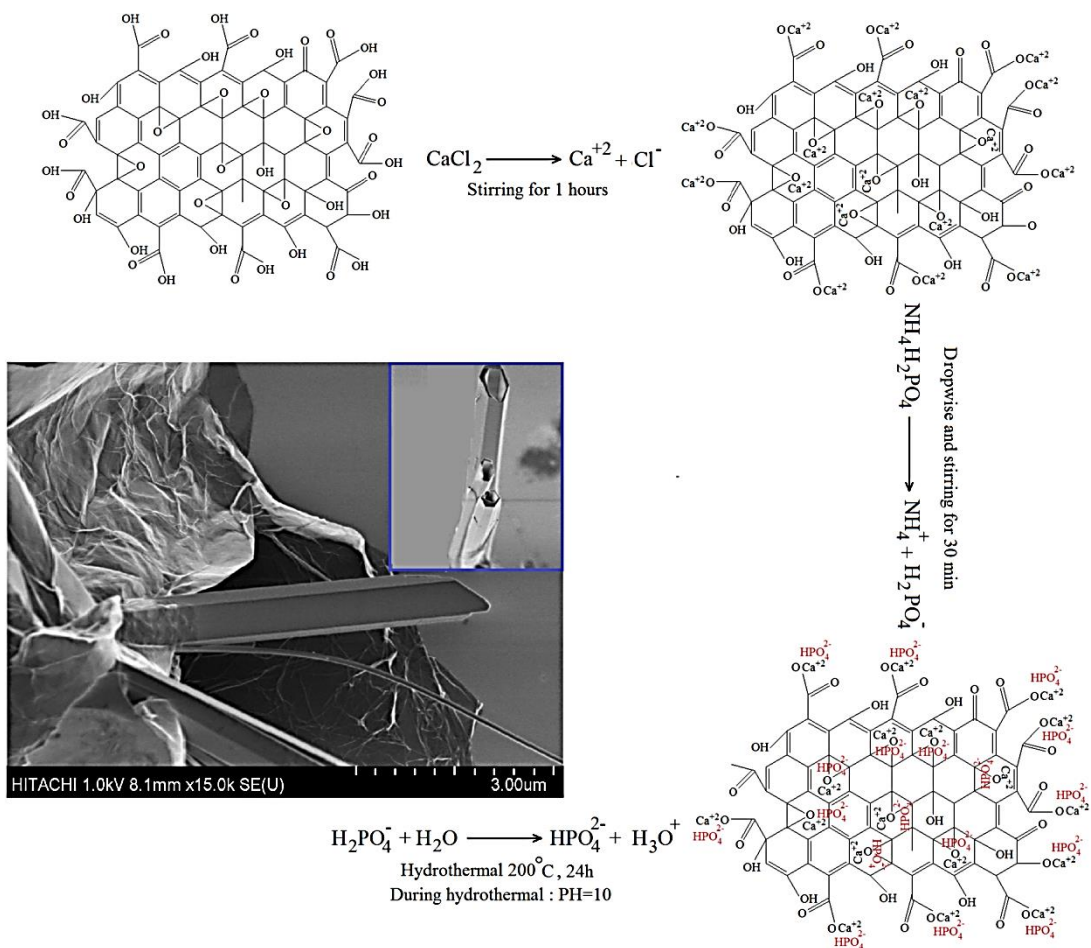
Figure 4.1 The proposed *in situ*-synthesis mechanism for the nHA-rGO composites in solvo-thermal processing.

Figure 4.2 shows the FESEM images of the samples created using the hydrothermal method. As observed in Figure 4.2a, the rGO nano-sheet is very thin with some wrinkles and folding (Yang et al., 2012; L. Zhang et al., 2013). The morphology of the nHA is shown in in Figure 4.2b with the preferred c-axis growth orientation of the nano-tubes on the hexagonal HA with an average length that is shorter than 15 µm. This is similar to the natural HA in bone and enamel tissue. These nano-tubes self-assemble in an array and even exhibit fabric-like features.
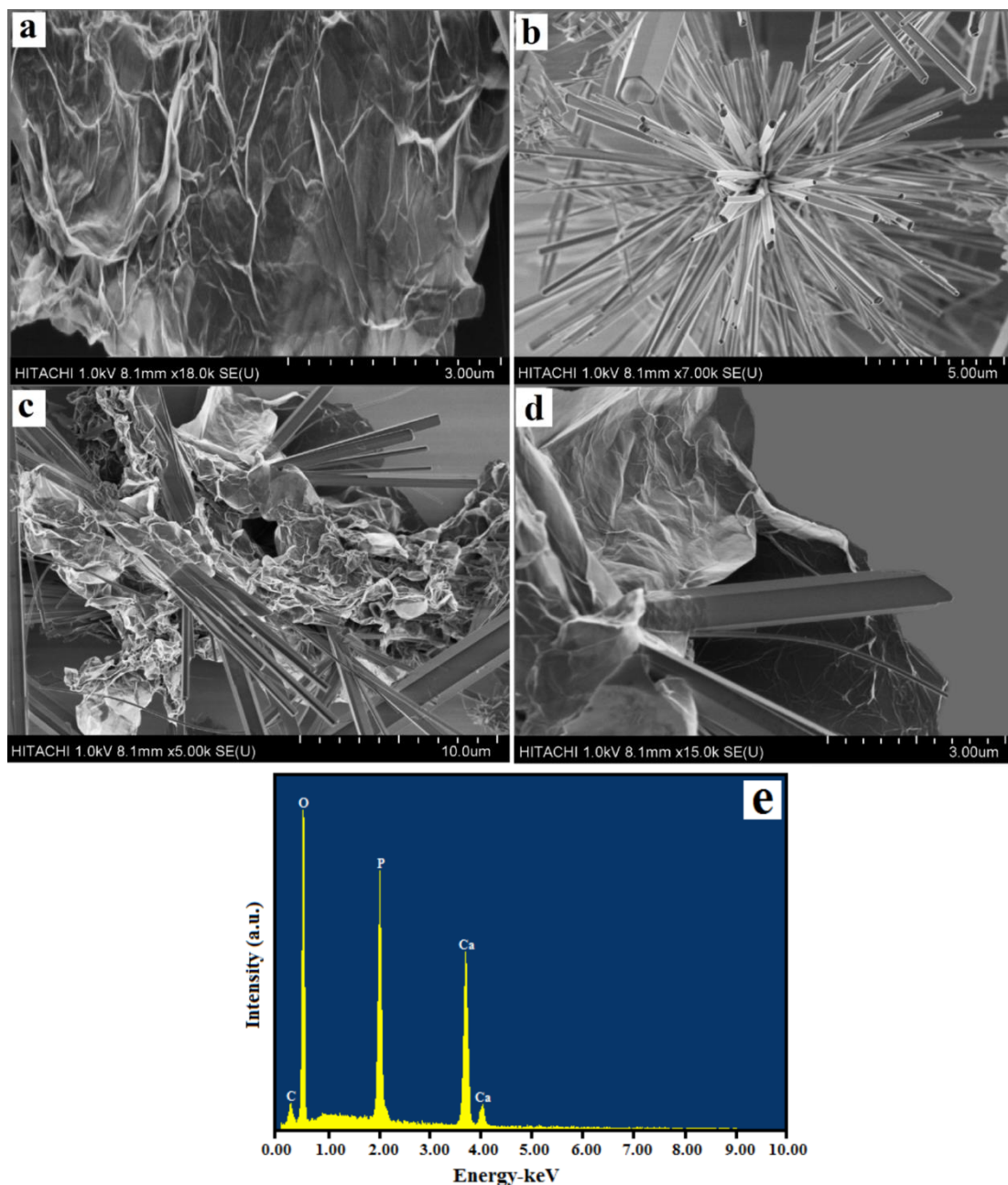
Figure 4.2 FESEM images of the GO (a), HG-0 (b), HG-3 (c and d) and EDAX spectrum of HG-3 (e).

The HG-3 composite is shown in Figure 4.2(c and d). The rGO is curled and corrugated on the nHA, forming uniform and smooth surface structures. Figure 4.2d shows a high resolution FESEM image of an individual nHA with an rGO sheet. The wrinkled surface of the rGO is clearly discernible in the image. Figure 4.2e shows results from the energy-dispersive X-ray spectrometry (EDX) that was performed on the composite, where the atomic Ca to P ratio is approximately 1.58, which is consistent with the stoichiometric ratio for the nHA.

The XRD patterns for the GO, rGO, HG-0 powder and sintered HG-3 are shown in Figure 4.3. The XRD patterns for the GO and rGO (Figure 4.3(a and b)) show related peaks that were centered at 9.85º and 24.72º and 43.54º. The XRD pattern for the GO shows an intense and sharp diffraction peak at $2\theta = 9.85º$ that is attributed to the (001) lattice plane, which corresponds to a d-spacing of 0.83 nm. This is consistent with the lamellar structure of the GO. Comparatively, the diffractogram of the rGO shows the disappearance of this strong peak and the appearance of a broad (002) peak at 24.85º, which corresponds to a d-spacing of 0.35 nm, indicating the successful reduction of the GO. Figure 4.3(c and d) shows the XRD patterns for the synthesized HG-0 and sintered HG-3. The major peaks in two patterns are from hydroxyapatite (JCPDS PDF 09-0432) which contains sharp and strong peaks due to the high degree of crystallinity of the powder and composite after HIP. According to phase transformation of HA, the consideration of two major phases (β-TCP and α-TCP) is significant. The two highest peaks of β-TCP (JCPDS PDF 070-2065) appears at $2\theta= 27.77°$ and $2\theta=31.02°$ are absent after consolidification, whereas, the third highest peak at $2\theta=34.33°$ overlaps with the peak of HG-0 ($2\theta=34.3°$). On the other hand, the highest peaks of α-TCP (JCPDS PDF 029-0359) at $2\theta=30.71°$ is absent and the second and third highest peaks ($2\theta=28.89°$ and $2\theta=34.21°$) overlap with peaks of HG-0 ($2\theta=28.93°$ and $2\theta=34.3°$) (Lahiri et al., 2010; L. Zhang et al., 2013).
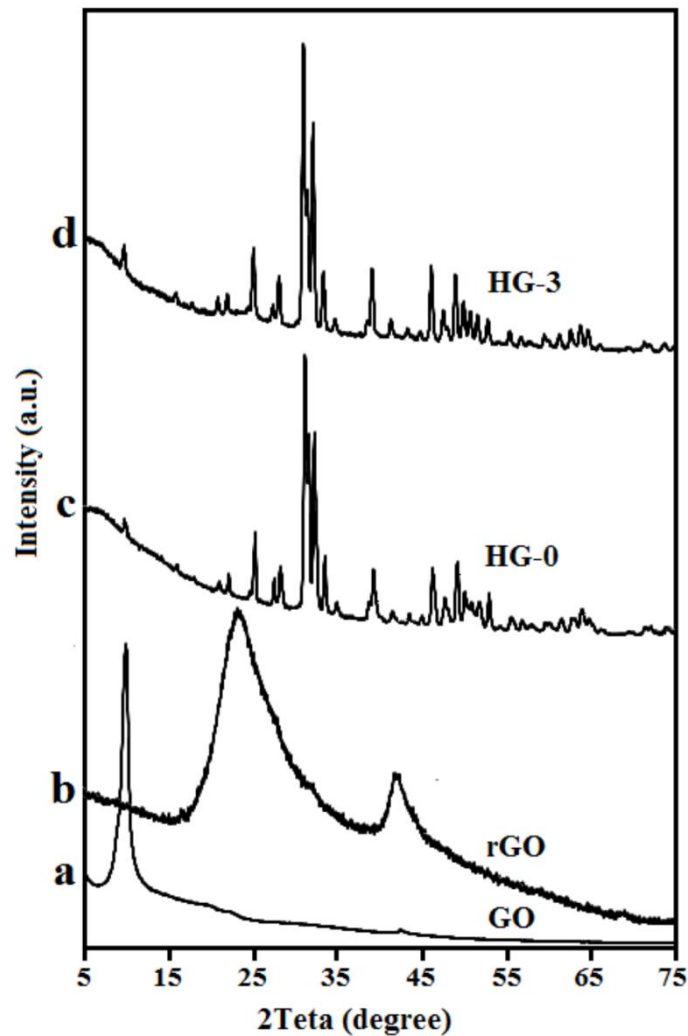
Figure 4.3 X-ray diffraction patterns for the synthesized GO (a), rGO (b), HG-0 powder (c) and sintered HG-3 (d).

Hence, the presence of β-TCP and α-TCP cannot be concluded. These observations prove that HA does not dissociate into TCP during HIP processing. Previous studies on HIP processing of HA and HA composites report only a partial decomposition of HA to TCP. They mentioned that the decomposition was enhanced with the presence of minute impurities or non-stoichiometric compositions in the HA powders. The excellent compositional homogeneity and phase purity associated with nanocrystalline HA stabilized the samples against decomposition at high temperature (Ahn et al., 2001; Ergun, 2011; Raksujarit et al., 2010; Sadeghian et al., 2006). Moreover, there are no traces of the graphite peaks due to the presence of strong HA peaks in the vicinity and their small content GO, whereas their presence can be

confirmed by FESEM, which demonstrates that the incorporation of the rGO has no influence on the stability of the nHA. Moreover, the lack of rGO peaks is most likely relevant to the layered structure of the rGO with irregular arrays of atoms in three dimensions. (Y. Liu et al., 2013a).
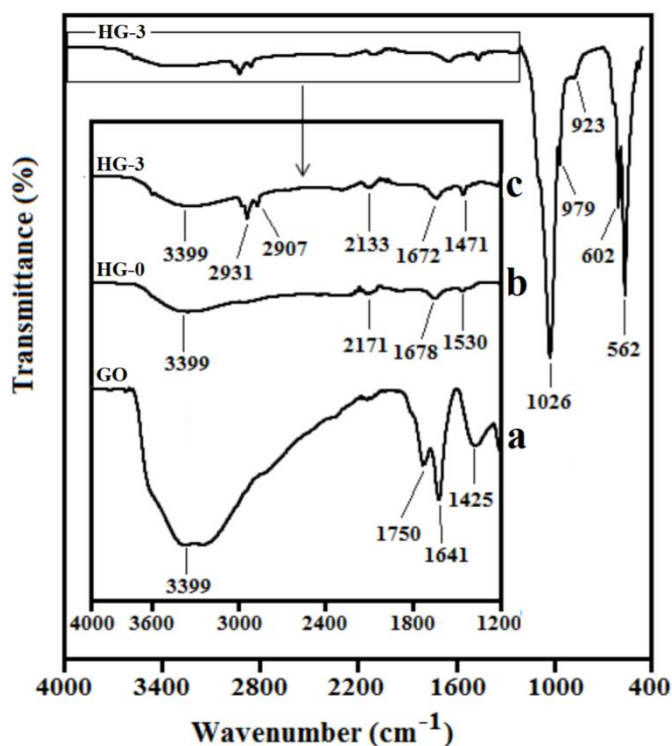
Figure 4.4 FT-IR spectra of the HG-3 powder and insets: GO (a), HG-0 powder (b) and sintered HG-3 (c).

Figure 4.4 and insets a, b, and c show the FTIR spectra of the GO, HG-0 and sintered HG-3. The mutual absorbance bands at approximately 3399 cm^{-1} are assigned to hydroxyl group (OH⁻) stretching. The position of the characteristic bands at 1026, 979, 923, and 562 cm^{-1} in the FTIR are attributed to the stretching and bending of phosphate (Y. Liu et al., 2013a). The band at 923 cm^{-1} is assigned to the acidic phosphate group (HPO_4^{2-}) due to P-O(H) stretching vibrations. The band located at approximately 562 cm^{-1} is attributed to P-O bending ($\upsilon_4 PO_4$). From the insets of Figure 4.4(a, b and c), the bands at 1750 cm^{-1} and 1641 cm^{-1} are assigned to the stretching vibrations of the carboxyl group (COOH) on the edge of the basal planes or the conjugated carbonyl groups (C=O) and the sp^2 hybridized C=C vibration stretching,

respectively (M. Li, Wang, et al., 2013). The absorption bands of the methylene groups (CH$_2$), which are inherent in the rGO, are present at approximately 2907 cm^{-1} and 2931 cm^{-1}. The peak at 1425 cm^{-1} is attributed to the deformation of the O-H (K. Wang et al., 2011). In contrast, the peaks at 1750 cm^{-1} and 1425 cm^{-1} in the FTIR spectrum of the HG-3 composite are no longer visible, which points to the reduction of GO.

The high temperatures required during sintering make it necessary to check on the survival of rGO structure in the final samples. Raman spectroscopy is a very powerful tool and permits a relatively easy and effective approach for investigating the crystalline quality and structural changes resulting from the GO to rGO transformation. This is performed by monitoring the relative intensities of the D and G peaks, which are characteristic of the sp^2 and sp^3 bonds in the hexagonal carbon structure and represent the in-plane stretching and breathing modes, respectively. The 2D (Ǵ) peaks are attributed to their respective higher order modes originating from a double resonance process (Miranzo et al., 2013; Govindaraajan B Yadhukulakrishnan et al., 2013). Figure 4.5 and Table 4.1 show the Raman spectra and all related values, respectively. The existence of the G and 2D peaks before and after sintering the bulk samples confirms the presence of rGO in the samples. The position of the G and 2D peaks are affected by several factors: (i) the densities of the defects in the rGO during the sintering process, (ii) the residual thermal stress evolution during the cooling step and (iii) the reduction in the number of graphene layers (rGO) (Ferrari et al., 2006; Ferrari & Robertson, 2000; Tsoukleri et al., 2009; G. B. Yadhukulakrishnan et al., 2012).

Table 4.1 Peak position of the D and G bands and intensity ratios of I_D/I_G and I_{2D}/I_G.

Sample	D band	G band	2G band	I_D/I_G	I_{2D}/I_G
	Raman shift	**Raman shift**	**Raman shift**		
Graphene oxide	1360	1595	------	0.788	------
Unsintered HG-3	1352	1593	2718	0.944	0.295
Sintered HG-3	1358	1602	2738	1.15	0.14
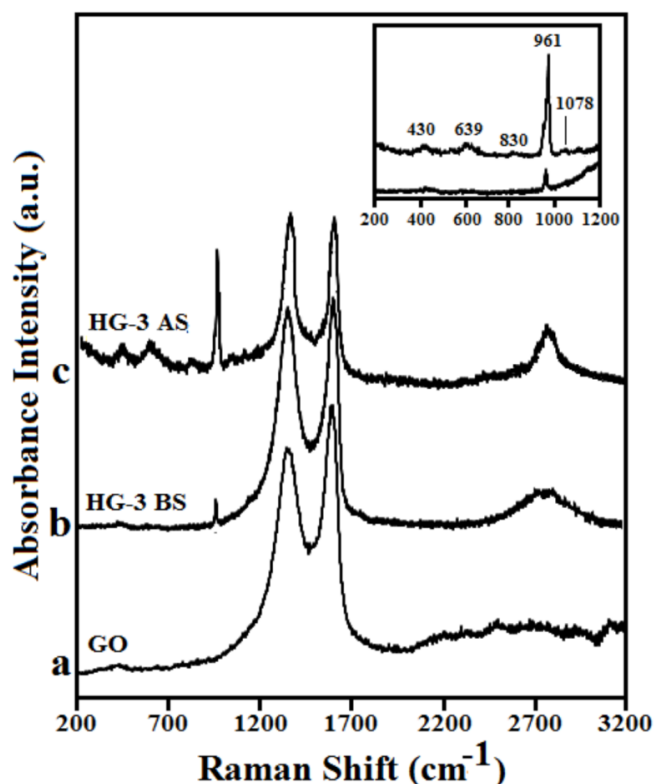
Figure 4.5 Raman spectra of the GO (a), HG-3 before sintering (BS) (b) and HG-3 after sintering (AS) (c).

As shown in Figure 4.5a, the two typical GO peaks are found at 1360 cm^{-1} and 1595 cm^{-1}, which correspond to the D and G bands, respectively. With the reduction of the GO, the D and G bands shift to lower wave-numbers of 1352 cm^{-1} and 1593 cm^{-1}, respectively. The presence of the 2D peak at approximately 2718 cm^{-1} (as observed in Figure 4.5b) shows an increase in the number of layers in the rGO compared to the GO. The ratio of I_{2D}/I_G and the Full Width Half Maximum (FWHM) of the 2D peak are sensitive to the layers of graphene. From Figure 4.5(b and c), the I_{2D}/I_G intensity ratio decreased from 0.29 to 0.14, and the 2D peak is narrower, sharper and shifts to higher

wavenumbers compared to samples examined prior to sintering, confirming an increase in the number of graphene layers (H. Fan et al., 2010; Ferrari et al., 2006; Ni et al., 2008; A. Reina et al., 2009; Y. Zhang et al., 2013). This result strongly shows that the thinning rGO agglomerating into a few layers of graphene takes place during the HIP process (L. Zhang et al., 2013). Furthermore, the I_D/I_G ratio is the index of the degree of crystallization or the surface defect density present in the GO and the rGO. However, the major evidence is the degree of disorder in the rGO compared to the GO, which is observed from the intensity ratio of the D and G bands (I_D/I_G) (Kosma et al., 2013). As observed in Figure 4.5(a and b), the ratio for the rGO increases from 0.788 to 0.944 compared to the GO, implying that the thermal reduction created a large number of sp^2 bonds and structural defects in the graphene lattice (Stankovich et al., 2007). The spectra of the bulk composite (HG-3) after sintering is shown in Figure 4.5c. The carbon peaks in the rGO were retained, inferring that no chemical reaction occurred during the HIP process. The lower relative intensity of the D (1358 cm^{-1}) to G (1602 cm^{-1}) band implies that the obtained rGO is mainly composed of well-crystallized graphite (Haipeng Li et al., 2010). The I_D/I_G ratio for the un-sintered samples is 0.944, whereas the ratio for the sintered samples is 1.15, suggesting that the damage and defects performed to the rGO is due to the high pressure and temperature during the sintering process (M. Cheng et al., 2012; Gupta et al., 2013). Moreover, the intensity of the D band in the sintered sample is less than in the un-sintered sample, which shows that some structural transformation occurred in the sintered samples (Afzal et al., 2013).

Figure 4.5b shows the spectrum of the HG-3 before sintering, indicating the existence of the HA phase. The broad and sharp peak with a low intensity at approximately 425 cm^{-1} and 958 cm^{-1} and a FWHM of approximately 18 cm^{-1} is due to the O-P-O bending modes (ϑ_2) and the P-O stretching mode (ϑ_1) of the PO$_4$ group in the HA, respectively (Antonakos et al., 2007; Sungjin Kim & Park, 2010; Lobo et al.,

2010). Only after sintering (Figure 4.5c) does the HA high crystalline phase appear. As is observed, the characteristic peaks of the HA at 430, 639, 830, 961, 1078 and 1115 cm^{-1} are all present. All these peaks indicate the stretching of different bonds in the PO_4^{3-} ions. The higher crystalline degree for the HA (specifically in the 961 cm^{-1} band) is evident due to the lower band FWHM of 12.3 cm^{-1}. However, other bands of lower intensities are observed at approximately 430, 639 and 830 cm^{-1}. The strongest and sharpest peak at 961 cm^{-1} corresponds to the symmetrical stretching of the tetrahedral oxygen atoms, surrounding the phosphorus atom. This peak is the strongest evidence for the presence of HA and is unique and different from the peaks from other calcium phosphate materials (Afzal et al., 2013). The 1078 cm^{-1} peak that is assigned to the apatitic phosphate groups is observed only in high quality crystalline stoichiometric HA. The Raman band recorded at 1040-1045 cm^{-1} taken from a sample of human bone formed *ex-vivo* is assigned to P-O stretching (Lobo et al., 2010).

4.1.2   Mechanical Properties

Figure 4.6 shows the FESEM of the fracture surface morphology of the sintered samples with different ratios of rGO additions. In these micrographs, not only the overall distribution but also the local contacts between the matrix and the rGO additions can be observed. These figures show rGO nano-sheets of different sizes that are homogeneously dispersed with no clustering or agglomeration in the HA grains (Figure 4.6(c-h)). Several factors determine the reinforcing efficiency of the nano-scale fillers in a ceramic: (1) the inherent mechanical properties of the filler material, (2) the efficiency of the load transfer at the interface of the matrix and filler and (3) the dispersion level of the nano-scale fillers in the ceramic matrix (J. Liu et al., 2013).
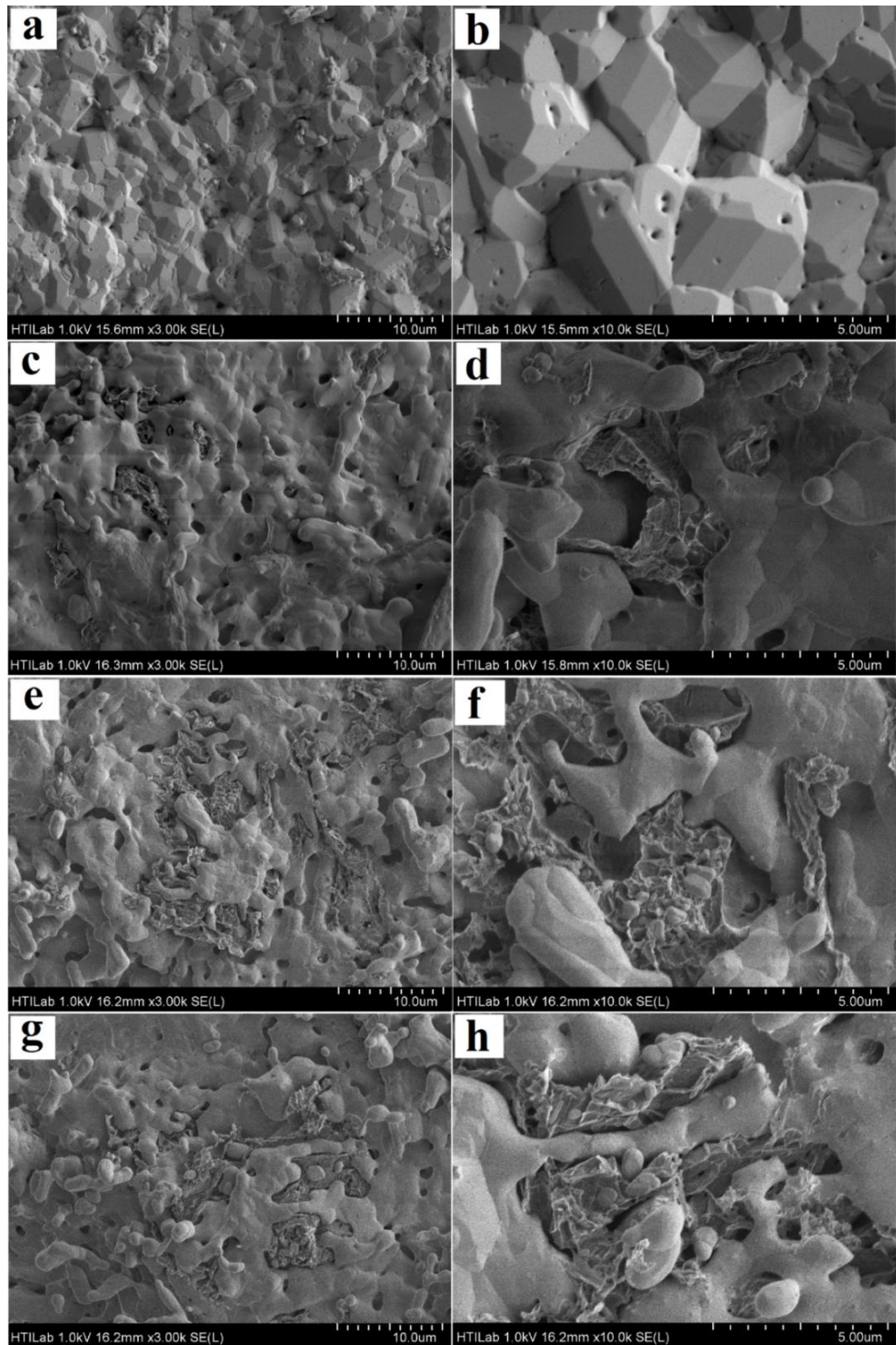
Figure 4.6 FESEM and high magnification micrograph of fracture surfaces for the sintered samples: HG-0 (a and b), HG-1 (c and d), HG-2 (e and f) and HG-3 (g and h).

When consolidation occurs, the graphene nano-sheets are either bent or embedded between the HA grains due to the force applied by the matrix grains surrounding the rGO nano-sheets or are distributed in the grain boundary with a rough and wrinkled surface texture. The close contact between the grains and the nano-sheets

causes more binding between the matrix grains and the graphene, causing increased contact area and mechanical interlocking, leading to enhanced load transfer efficiency between the HA matrix and the rGO.
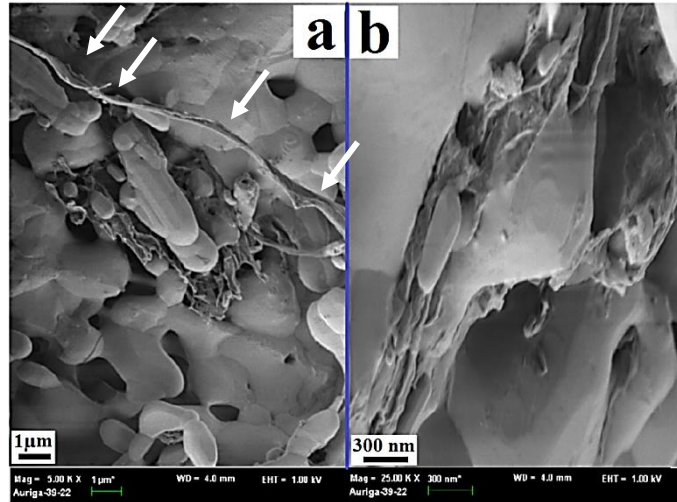
Figure 4.7 FESEM images of the fracture surface for the sintered HG-3 composite. A large rGO sheet is visible and is indicated by a white arrows (a) and a high magnification image of a rGO nanosheet (b).

This effect plays a significant role in enhancing the mechanical properties of the composites. Moreover, the FESEM micrographs (Figure 4.7(a and b)) obviously show the rGO pulling out at the grain boundary on the fractured surface of the sintered composite samples. These effects are the result of an increase in bonding strength between the rGO and the HA grain that requires more energy to cause the nano-filler to pull out from the HA matrix (L. Zhang et al., 2013). The absorption of more fracture energy during the protrusion of the rGO further delays the rupture and increases the strength of the bulk composite structure (Lahiri et al., 2013; L. Zhang et al., 2013). We expect that the energy required to pull out a sheet is greater than that of a single-walled or multi-walled nano-tube or nano-fiber due to "sheet wrapping" around the matrix grain boundaries and the increased contact area with the matrix, especially in the HIP composites (Kvetková et al., 2013). Moreover, the added rGO seems to increase the porosity of the composite. From the results in Table 4.2 and Figure 4.6, the addition of the rGO affects the density of the composites, and the increase in the amount of the rGO

slightly decreases the relative density of the composite from 96.7% to 93.23%, which may lead to the deterioration of the mechanical properties.

Table 4.2 Relative density and mechanical properties of the composites.

rGO (wt%)	Relative density (%)	Microhardness (Hv)	Elastic modulus (GPa)	Fracture toughness (MPa m$^{0.5}$)
0	98.12±0.21	322±8	87±8.34	0.81±0.05
0.5	96.76±0.33	363±5	93±4.23	0.95±0.03
1	94.85±0.28	425±4	111±6.41	1.31±0.07
1.5	93.23±0.24	381±7	123±3.86	1.51±0.05

A summary of relative density and mechanical properties (hardness, elastic modulus and fracture toughness) of the composites is shown in Table 4.2. Microhardness values for the composites decrease at only 1 wt% rGO compared to the other samples examined. These results show that even low concentrations of rGO have a significant influence on the bulk mechanical properties. The decrease in the hardness of composite for high filler loading fractions (HG-3) is dependent on the residual porosity present around the rGO after the sintering process (Kvetková et al., 2012; Kvetková et al., 2013; J. Zhu et al., 2011). It is clear that the fracture toughness and elastic modulus are greatly dependent on the amount of rGO in the composite. The composite containing 1.5 wt% rGO shows a maximum fracture toughness and elastic modulus of 1.51 MPa m$^{0.5}$ and 123 GPa, approximately 86% and 40% higher than pure nHA, respectively. The enhancement in the elastic modulus of the composite is due to three significant factors: (i) the higher E value associated with rGO reinforcement (ii) the homogeneous distribution of the nano-sheets in the matrix and (iii) a strong HA/rGO interface (Lahiri et al., 2010). From the fracture toughness results, the nano-sheets are more effective at toughening the HA prepared by the HIP process, even at very low weight percentages. Our results are comparable with those from other works using different sintering process. Liu *et al*. (Y. Liu et al., 2013a) examined the mechanical properties of a 0.1 and 1 wt% rGO-HA composite that was consolidated using SPS and reported that the

hardness, elastic modulus and fracture toughness values improved by 26%, 48% and 203% compared to a pure HA pellet, respectively. The mechanical properties in the present study are dependent on the sintering process. Zhao *et al*. (Y. Zhao et al., 2013) used a hot pressing method and found the hardness decreased with an increase in the GNP, whereas the fracture toughness improved 75% compared to pure HA. For the SPS sintering procedure, Zhang *et al.* (L. Zhang et al., 2013) identified improved hardness, elastic modulus and fracture toughness of 43%, 31% and 82%, respectively, compared with pure HA.

To assist in providing a detailed understanding about the improved fracture toughness at different weight percentages of rGO, Figure 4.7 and Figure 4.8 show the high specific area of the rGO, which is located at the intergranular region and provides a higher resistance to crack propagation compared to pure HA. Fractographic examination of the striation lines and fracture surfaces show signs of various toughening mechanisms resulting from the presence of rGO. Figure 4.8 shows the observed toughening mechanisms, such as crack branching (Figure 4.8b), crack bridging (Figure 4.8(c and f)), pull out (Figure 4.8(d and f)), and crack deflection (Figure 4.8e) in ceramic composites reinforced with rGO and identified from microhardness indentations. In this case, notwithstanding the fact that the rGO was annihilated during the grinding/polishing procedure, the effectiveness of the toughening mechanisms resulting from the rGO addition is still clearly visible.

Crack branching is a toughening mechanism that is frequently observed in all of the investigated composites. The origin of this mechanism is the interaction of the propagating crack and the rGO of a different size. The lengths of the cracks are several microns, and the frequency of occurrence of this mechanism is quite high (Figure 4.8b).
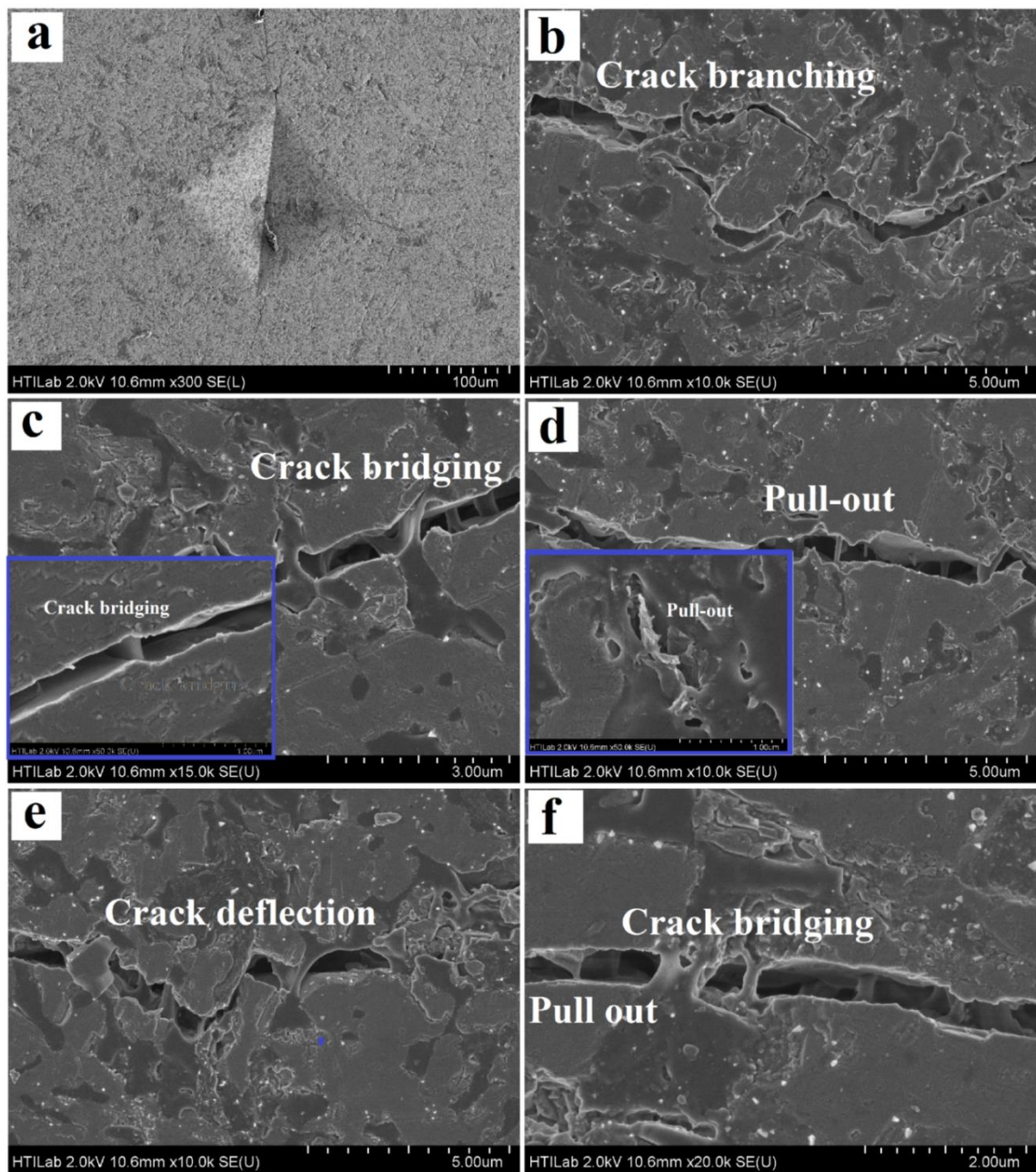
Figure 4.8 Characteristic toughening mechanisms at a striation line in the HG-3 composite: vicker`s indentation craters (a) and radial cracks: crack branching (b), crack bridging (c and f), pull out (d and f), crack deflection (e).

Characteristic crack bridging is visible in Figure 4.8(c and f) on the striation line with a plane of the rGO nano-sheets. A similar bridging/pullout mechanism is illustrated in Figure 4.7 and Figure 4.8(d and f), where the rGO bridges the propagated crack and pulls out in the bridging zone of the crack far behind the crack tip. We frequently observe similar pull outs in the rGO nano-sheets, which are tucked and wrapped around the matrix grains in the rGO and HIP systems. As shown in Figure 4.8e, when a crack

propagates and interacts with an rGO nano-sheet, it is arrested and deflected in-plane. It is believed that such a crack deflection mechanism creates a more tortuous path to release stress, which helps increase the fracture toughness. All the toughening mechanisms encountered in this study are similar to those reported by other researchers (J. Dusza et al., 2012; Kvetková et al., 2012; Kvetková et al., 2013; J. Liu et al., 2012; Walker et al., 2011; Govindaraajan B Yadhukulakrishnan et al., 2013)

4.1.3 Biological Properties

Apart from the mechanical characteristics, the non-toxicity and good biocompatibility found in the nHA-rGO composites are vital for potential clinical applications. The biological performance of the composites was initially reviewed in a cell culture test in this study. As acknowledged, biomaterials were used to promote new tissue formation by providing active surface sites for direct cellular attachment, migration and proliferation. In this context, the composites designed here should promote adhesion and proliferation of osteoblasts to ensure successful results for use in orthopedics.

Typical morphologies in the HOFB human osteoblastic cells adhered on the surfaces of the sintered HA, nHA and composites for the nHA-rGO specimens after culturing for 1 day are shown in Figure 4.9(a–e), respectively. In the FESEM images, osteoblastic cells are polygonal and contain widespread forms of fine filopedia in each group. After 1 day of cultivation, osteoblast cells are attached and then flattened on the specimen surfaces. This behavior is more pronounced for the sintered HG-3 composite. Further increases in the culture time from to 3 and 5 days show that the density of the adhered cells increases dramatically. The cells proliferate and anchor on the specimen surfaces through the fine filopodia at the leading edges. Figure 4.10(a-c) shows typical

examples (HG-3) of the cell migration by extension of the filopodia on the specimen surfaces for different culture times.
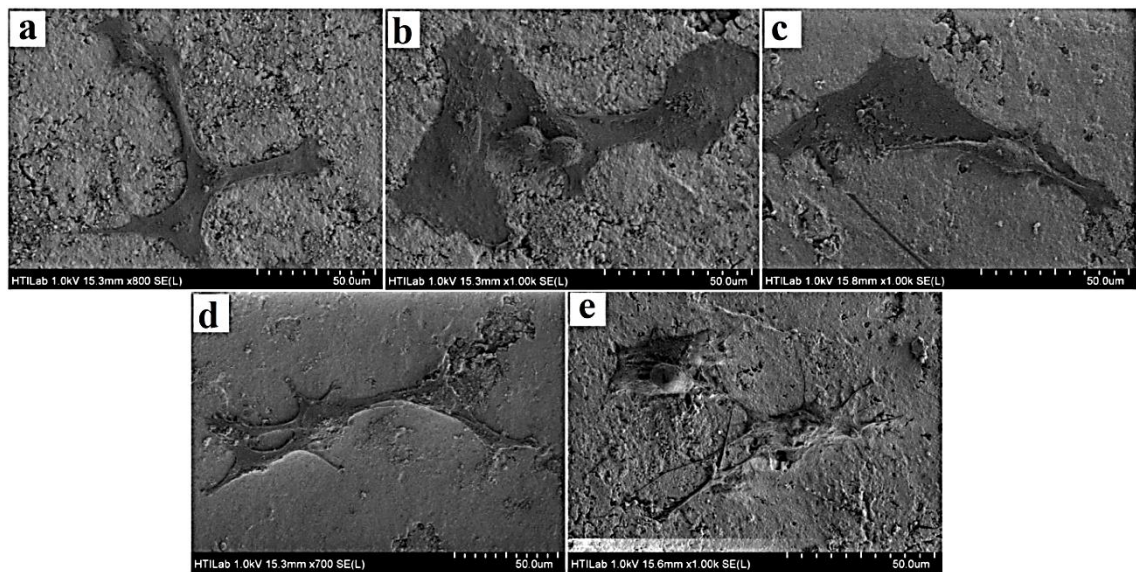
Figure 4.9 Morphology of the osteoblasts cultured on the surfaces of the sintered HA (a), HG-0 (b), HG-1 (c), HG-2 (d) and HG-3 (e)
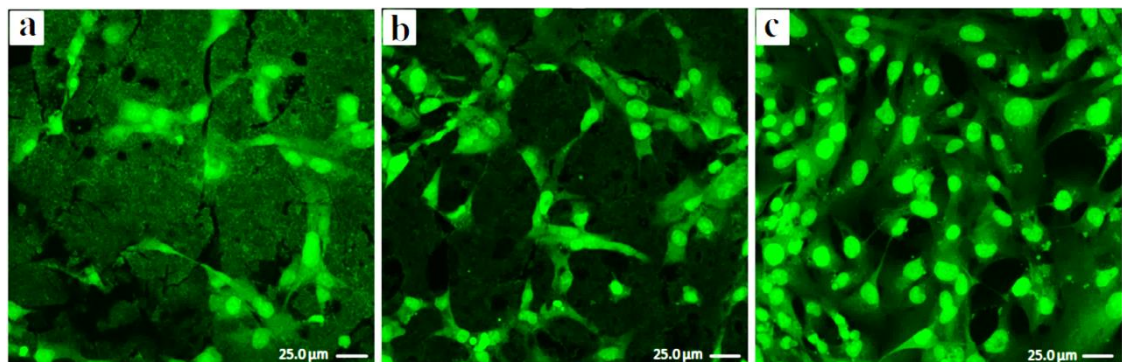
Figure 4.10 Confocal microscopy images of live (green) osteoblast cells cultured on the surface of the sintered HG-3 sample at 1 day (a), 3 days (b) and 5 days (c).

An MTT assay is a commonly used practice to assess the viability of biological cells by a reaction with a chemical reagent. Viable cells reduce the MTT reagent to form a colored formazan salt. Thus, water-soluble MTT is converted by mitochondrial dehydrogenases in living cells to a water-insoluble formazan product. The precipitated formazan is dissolved in a solution of SDS in diluted HCl acid to yield a colored solution. The optical absorbance of the colored solution is measured with a detector at 570 nm. The intensity of the color produced is directly related to the number of viable

cells. The MTT assay results from the sintered specimens are shown in Figure 4.11. The MTT assay shows that the cell viability increases with increasing time when the osteoblast cells were co-cultured with HA, nHA and nHA-rGO, indicating that nano-tube hydroxyapatite affected the cell proliferation. It is clear that the HG-0 and its composites may improve the viability and enhanced proliferation of the osteoblasts. Moreover, the HG-3 composite exhibits the highest optical absorbance after 1, 3 and 5 days in the culture. This implies that the HG-3 composite exhibits excellent bio-compatibility.
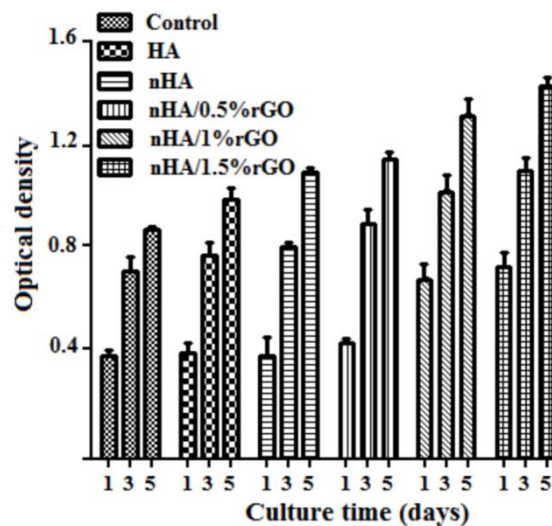
Figure 4.11 Proliferation of the osteoblasts on the surface of the sintered samples: HA, HG-0, HG-1, HG-2 and HG-3 for 1 day, 3 days and 5 days.

Additionally, a comparison of the absorbance values of the HA and nHA shows that the morphology and crystalline degree of synthesized powder has an important effect on the osteoblast viability (F. Chen et al., 2010; X. Liu et al., 2012). Liu *et al*. considered the cell responses from nano-rod HA of different diameters, lengths and crystalline degrees. They reported that the nano-rod with higher a crystalline degree and larger diameter and length yielded a better biological response at promoting cell growth, inhibiting cell apoptosis and increasing active cell morphology. Chen *et al*. performed cell viability tests on the as-prepared HA samples with different morphologies at HA concentrations in the range of 10-100 mg mL^{-1}. They reported that the as-prepared HA

nano-wire/nano-tube ordered arrays and fabrics exhibit similar structures as natural hard tissues and may be useful in biomedical research areas.

4.2 Characterization of Nickel-doped Biphasic Calcium Phosphate/Graphene Nanoplatelet Composites for Biomedical Application

4.2.1 Physical and Chemical Properties

Figure 4.12(a and b) present the XRD profiles of the samples with different degrees of Ni substitution before and after calcination at 900 °C for 1 h. From Figure 4.12a, some distinct features can be recognized upon increasing the Ni content from 0 to 6%. First, the intensity of the HA characteristic peaks decreased significantly. This behavior is believed to be caused by the amorphization of the product. Second, peak broadening increases with the increase of Ni substitution because of the structural evolution (crystallite refinement and lattice strain increase). This result indicates that the synthesized powders are nanocrystalline in nature.
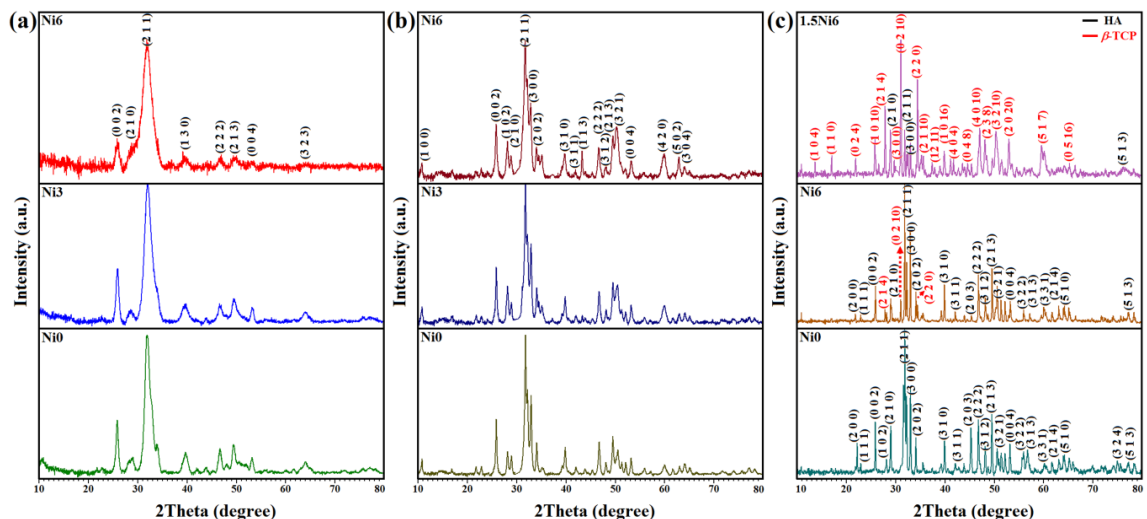
Figure 4.12 XRD profiles of Ni0, Ni3 and Ni6 (a) before and (b) after calcination and of (c) Ni0, Ni6 and 1.5Ni6 after sintering.

As observed in Figure 4.12b, high-crystalline Ni-doped-HA nanopowders were formed, and no phase transformation or decomposition occurred after the calcination at 900 °C for 1 h. It is apparent that the characteristic peaks of the calcined samples were

more intense than those of the as-prepared powders. This finding suggests that the fraction of the crystalline phase increased after the thermal treatment. According to Figure 4.12c, a highly crystalline structure of monolithic HA was formed in the absence of nickel after the sintering process. With the addition of 6%Ni, the decomposition of HA to β-TCP and CaO was identified according to the following reaction:

$$Ca_{10-x}Ni_x(PO_4)_6(OH)_2 \rightarrow 3Ca_{3-x/3}Ni_{x/3}(PO_4)_2 + CaO + H_2O$$
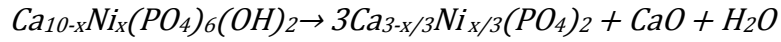
In the presence of 1.5% GNPs (1.5Ni6), HA significantly decomposed to β-TCP due to the high thermal conductivity of the GNPs. In general, HA is a non-conducting ceramic that exhibits poor thermal (1.25 W m^{-1} K^{-1}) and electrical (7×10^{-7} S cm^{-1}) conductivity (Y. Liu et al., 2013a). However, due to the presence of GNPs in the composite, a thermal gradient was created between the GNPs and HA, which results in a severe decomposition. Therefore, the phase percentage of HA decreased to 14%, while the percentage of β-TCP increased to 86%. The measurement of structural features such as crystallite size, volume fraction of grain boundary and crystallinity degree of the modified HA is essential because the phase composition and transformation are dependent on these parameters. The average crystalline size of the nanopowders was determined using the Debye-Scherrer equation. In accordance with Figure 4.13a, with an increase of the Ni content from 0 to 6%, the crystallite size of the Ni-doped HA decreased drastically from 24±1 to 11±1 nm. After the calcination process at 900 °C for 1 h, the crystallite size of pure HA increased notably to 56±3 nm. A similar trend was observed in the presence of Ni, where the crystallite size of HA increased to 45±2 and 39±2 nm when the Ni content increased from 3 to 6 %, respectively.

If a crystallite is a sphere of diameter D surrounded by a shell of grain boundary with thickness t, the volume fraction of the grain boundary (f) may be estimated using the following formula (F. Sun & Froes, 2002):

$$f = 1 - \left[\frac{D}{(D+t)} \right]^3$$

The *f* values were determined by substituting the experimental crystallite size obtained by XRD into *D* with the assumption that *t* = 1 nm.

From the obtained data, the *f* values ranged from 5±1 to 23±1 %. However, the volume fraction of grain boundary in the presence of 3 and 6 % Ni was higher than the pure HA (Figure 4.13b). After the calcinations process, the value of *f* decreased dramatically for all the samples due to the HA crystal growth during the thermal treatment. This finding suggests that the substitution of an appropriate amount of Ni in the HA lattice can lead to the formation of modified HA with a fine-grained structure. The crystallinity degree of the specimens was determined from the XRD profiles using the following equation (E Landi et al., 2000):

$$Xc = 1 - \left(\frac{V_{112/300}}{I_{300}} \right)$$

where *X*c is the crystallinity degree, I_{300} is the intensity of the (300) peak, and $V_{112/300}$ is the intensity of the shoulder between the (112) and (300) diffraction peaks.
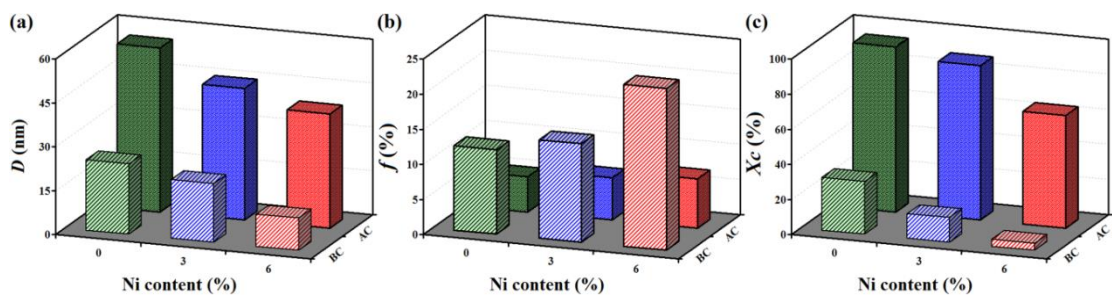
Figure 4.13 (a) Crystallite size, (b) volume fraction of grain boundaries and (c) crystallinity degree of the modified HA.

In the absence of Ni (pure HA), the crystallinity degree of HA was approximately 30±2 % (Figure 4.13c). This value decreased to 14±1 and 4±1 % when

the Ni content increased to 3 and 6 %, respectively. This finding indicates that the addition of Ni can affect the fraction of crystalline phase in the HA-based ceramics. During the calcination process, the crystallization of HA was dominant; therefore, the crystallinity degree increased sharply to 94±5 % for pure HA and to 88±4 and 64±3 % for the modified-HA with 3 and 6 % Ni, respectively. Indeed, apatites with higher crystallinity degree exhibit little or no activity toward bioresorption and are insoluble in physiological environment (Seckler et al., 1999). Therefore, all the calcined samples, especially pure HA and 3%Ni substituted-HA, can be expected to exhibit greater chemical stability, which could be applicable in bone-tissue engineering. For 1.5Ni6, severe HA decomposition was observed, which caused a drastic reduction in the crystallinity degree up to 6±1 %.

The lattice constants (*a*, *b*, and *c*) and unit cell volume of HA as a function of Ni content are summarized in Table 4.3. For the standard HA (JCPDS#24-0033), the *a*−axis and *c*−axis values are 9.4320 and 6.8810 Å, respectively. In addition, the unit cell volume of HA is 530.14 $Å^3$. The calculated data indicates that these values fluctuated during the ion-exchange and calcination treatments. In the absence of Ni, the *a*−axis and *c*−axis values were approximately 9.43264 and 6.89774 Å, respectively. In this case, HA exhibited a unit cell volume of approximately 531.501 $Å^3$. With the addition of 3 % Ni, a reduction in the lattice constants occurred, and consequently, the unit cell volume reached 529.583 $Å^3$. A further increase in the Ni content to 6 % led to a significant diminution in the unit cell volume of HA (V = 528.303 $Å^3$). These differences in the unit cell dimensions can most likely be attributed to the lattice distortion of HA during the ion-substitution process.

Table 4.3 Lattice constants (a, b, and c) and unit cell volume of HA as a function of Ni content

Composition	Calcination	$a = b$ (Å)	c (Å)	V (Å^3)
HA	–	9.43264	6.89774	531.501
HA	900 °C, 1h	9.42975	6.88974	530.559
HA–3% Ni (Ni3)	–	9.42893	6.87826	529.583
HA–3% Ni (Ni3)	900 °C, 1h	9.42202	6.89076	529.768
HA–6% Ni (Ni6)	–	9.41932	6.87564	528.303
HA–6% Ni (Ni6)	900 °C, 1h	9.42029	6.89120	529.607

It is apparent from Table 4.3 that the lattice parameters in the Ni-doped HA decreased significantly compared with undoped HA. This result is attributed to the replacement of the smaller Ni^{2+} (ionic radius 0.069 nm) with the relatively larger Ca^{2+} (ionic radius 0.099 nm) during the substitution process(Singh, 2007). This phenomenon in turn is responsible for the changes in the crystallite size, which is in good agreement with the presented data in Figure 4.12a, which indicates that the crystallite size of the product decreased with increasing Ni content from 0 to 6 %. During the calcination process at 900 °C for 1 h, the recovery of the HA lattice occurred, and therefore, the unit cell volume values increased slightly and were close to the standard HA. Overall, these results confirmed the substitution of Ni in the HA lattice.
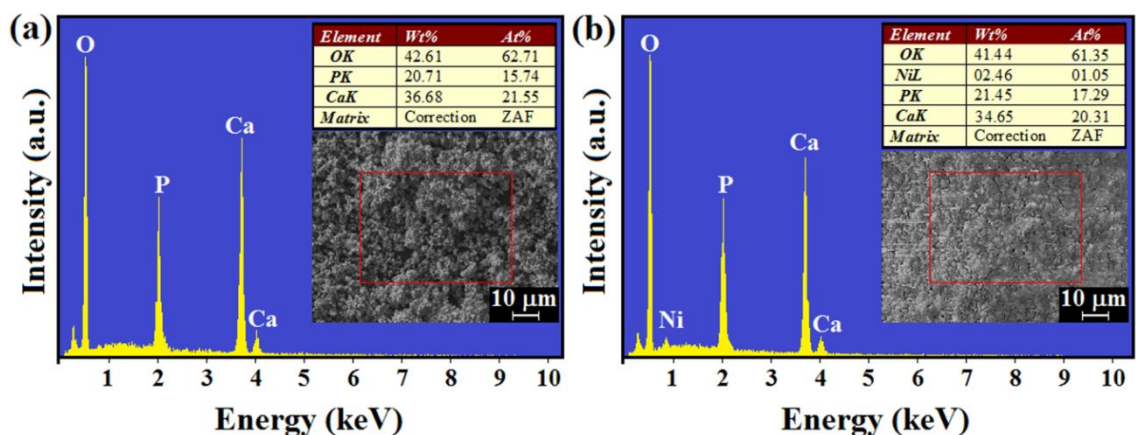
Figure 4.14 EDS analysis of the as-prepared powders: (a) pure HA and (b) 3%Ni-doped HA.

The EDS analysis was performed for several specimens, and typical results have been selected and presented in Figure 4.14. For more accurate results, EDS spectra were recorded over three different points on the specimens. The evaluation of the elemental constituents of pure HA revealed peaks belonging to calcium, phosphorus and oxygen. The EDS spectra were mainly used to determine the percentage of Ni in the HA lattice for Ni-doped HA. The average value of the tested areas indicated that the weight percentage of Ni was approximately 2.46 wt%, which was slightly lower than the ideal value (3%) but within a reasonable range. This result confirms the presence of Ni in the HA lattice, which was not apparent in XRD profiles. From the EDS spectra, pure HA had a Ca/P ratio of approximately 1.77. In the presence of various percentages of Ni substitution, this ratio changed and reached approximately 1.62 in 3%Ni-doped HA. In addition, the (Ca+Ni)/P ratio was approximately 1.73 when the Ni content reached 3%. These findings suggest that the values for HA and Ni-doped HA crystals are closer to the expected value for the molar ratio of calcium to phosphorus in the stoichiometric HA (Ca/P = 1.67). It is noteworthy that no chemically stable impurity was detected as a product of the subsequent milling.
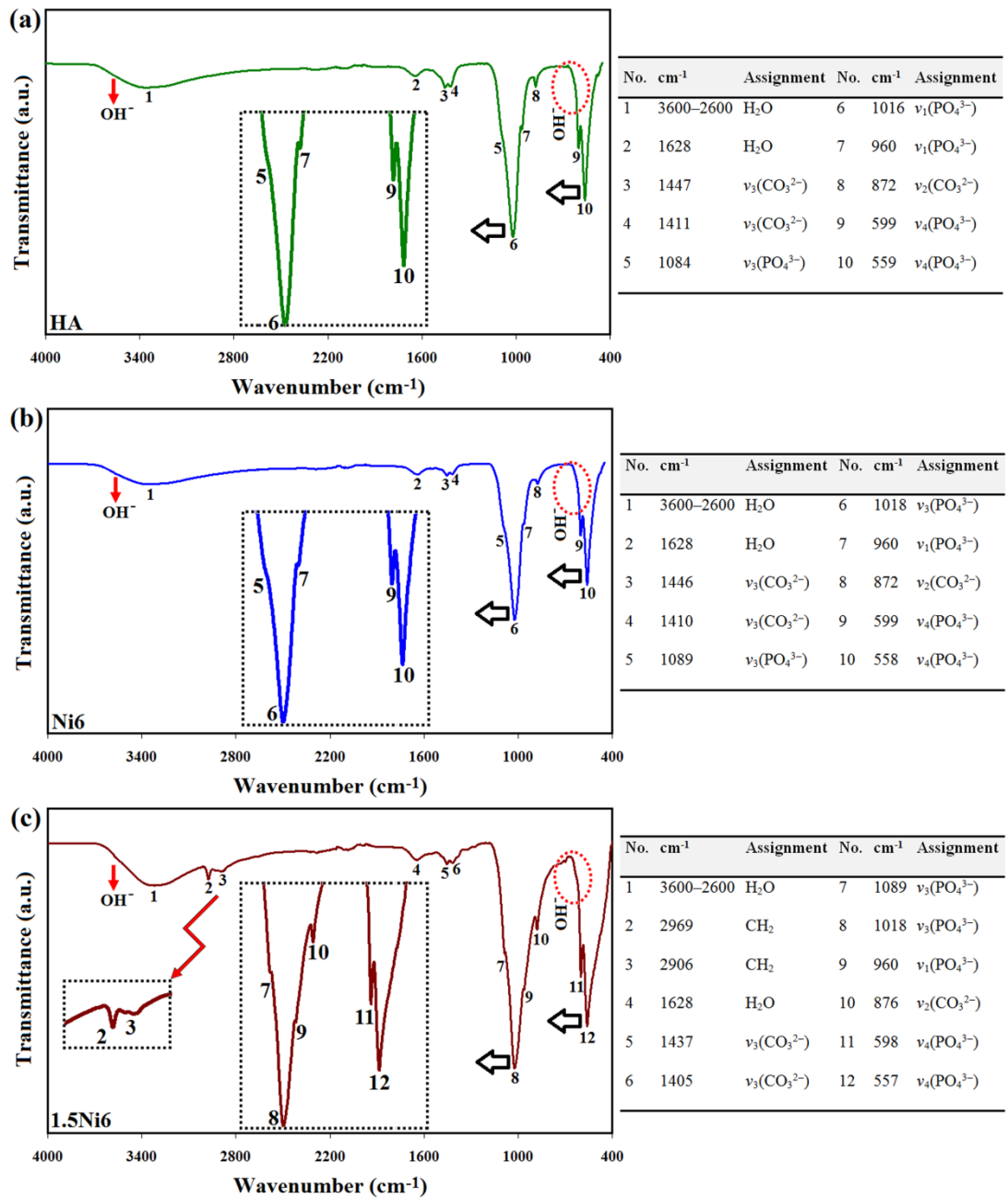
Figure 4.15 FT-IR spectra of the as-prepared powders: (a) pure HA, (b) Ni6 and (c) 1.5Ni6.

Figure 4.15 presents the FT-IR spectra of pure HA, Ni6 and 1.5Ni6. The functional groups of HA, such as PO_4^{3-}, OH^- and CO_3^{2-}, were detected in the 4000-400 cm^{-1} region in the FT-IR spectra (Kannan et al., 2011; Kaygili et al., 2014; Yajing et al., 2014; N. Zhang et al., 2014). The characteristic bands are assigned here:

(a) Two bands belonging to the vibration of the adsorbed water in HA appear at 3600–2600 and 1800–1666 cm^{-1} (Kaygili et al., 2014).

(b) For the pure HA, the bands at 1089 and 1018 cm^{-1} are attributed to v_3 PO_4; the band at 960 cm^{-1} is attributed to v_1 PO_4, and the peaks at 599 and 558 cm^{-1} are attributed to v_4 PO4 (Kannan et al., 2011; N. Zhang et al., 2014). These bands were slightly shifted due to the substitution of Ni in the HA lattice as well as the addition of 1.5% GNP.

(c) Two regions of the FT-IR spectra are ascribed to the carbonate vibrations in HA: (i) 850–890 cm^{-1} corresponding to $v_2(CO_3^{2-})$ (ii) 1420–1650 cm^{-1} belonging to v_3 vibrations of the carbonate groups (Lafon et al., 2008). The presence of the carbonated groups suggests that the as-prepared powders contained some CO_3^{2-} groups in the PO_4^{3-} sites of the apatite lattice (B-type substitution). It has been reported that this type of HA is more similar to biological apatite and can be very useful as a bone replacement material (Fathi & Mohammadi Zahrani, 2009; Bahman Nasiri-Tabrizi & Fahami, 2014). However, the usefulness of CHA depends on the powder features such as the average particle size, surface area, and morphology (W. Zhou et al., 2008).

(d) For 1.5Ni6, the characteristic bands of the methylene groups (CH_2), which are inherent in GNP, were detected at 2969 cm^{-1} and 2906 cm^{-1}.

(e) The FT-IR results indicated that in the presence of Ni, the severity of the band overlap increased slightly compared with that of pure HA, which implies a minor decrease in the fraction of the crystalline phase (crystallinity degree). This result is in good agreement with the XRD results. In accordance with the FT-IR spectra, the synthesized powders exhibited high chemical purity, which is crucial in biomedical applications.

Raman spectroscopy was performed to characterize the defect density, number of layers and crystallinity of the GNP structure in the composites. Typical Raman spectra of the samples are presented in Figure 4.16. The G and 2D (G′) peaks appear due to the

C-C bond plane stretching in GNP, where the 2D peak is related to the number of graphene layers, and the D peak corresponds to the defect density introduced in the structure. The presence of a small intensity D peak relative to the G peak in the pristine GNP indicates a very small defect density. Moreover, a 2D peak at ~ 2690 cm^{-1} is observed, which is typical of a multilayer sheet or platelet configuration of the GNP (Walker et al., 2011).

The Raman spectrum of the composite powder exhibits significant changes compared with that of GNP. Both the G and D bands are shifted toward higher wave numbers of 1349 and 1584 cm^{-1}, respectively. A shift in the G band toward higher wave numbers indicates an increase in the defect density in the graphene structure (Lahiri et al., 2010). The intensity ratio of the D to G bands (I_D/I_G) is a measure of the disorder degree and the average size of the sp^2 domains. The I_D/I_G ratios for the GNP and 1.5Ni6 composite powder were 0.26 and 0.71, respectively (Table 4.4). This result indicates an increase in the defect density in the GNP, which is most likely due to the ball-milling process.

The ball milling of 1.5Ni6 powders produced strong interactions between the GNP and Ni6 particles. These interactions on the GNP resulted in a lower I_{2D}/I_G ratio, which indicates partial loss of the graphene-like structure (Nieto et al., 2013). For the sintered samples, the I_D/I_G ratio increased from 0.71 to 0.93 compared with the composite powder, which might indicate some defect density introduced during the sintering process. The sintered samples tend to have higher I_D/I_G and lower I_{2D}/I_G ratios compared with the GNP powder. Moreover, previous studies have reported that a decrease in the intensity ratio of I_{2D}/I_G and the appearance of a narrow and sharp 2D peak compared with the pristine GNP are due to the increase of graphene layers.
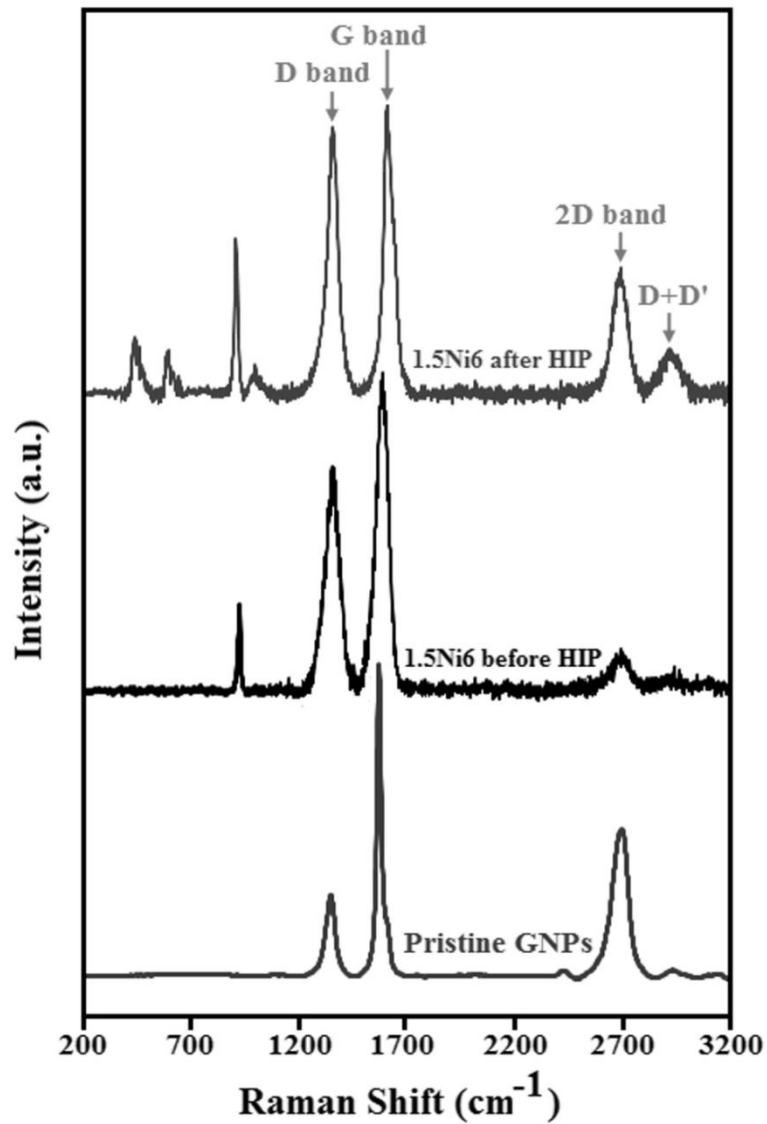
Figure 4.16 Raman spectra of pristine GNP and 1.5Ni6 before HIP and 1.5Ni6 after HIP.

Moreover, the peak at ~2940 cm^{-1} is attributed to the D+D′ band, which is generally related to point defects in the basal plane or edges of single-crystalline graphene domains. The increase in the intensity of the D+D′ peak at ~2940 cm^{-1} indicates better graphitization (Cui et al., 2011; Kiraly et al., 2013).

The Raman spectrum of 1.5Ni6 contains an intense peak at 961 cm^{-1}, which is associated with the symmetric (ϑ_1) P-O-P stretching mode of the free tetrahedral phosphate ion. After the sintering process, the peak at 961 cm^{-1} was observed to have higher intensity than the composite powder.

Table 4.4 Peak position of the D and G bands and intensity ratio of I_D/I_G and I_{2D}/I_G

Sample's name	D band	G band	2D band	D+D′	I_D/I_G	I_{2D}/I_G
	Raman shift	Raman shift	Raman shift	Raman shift		
GNP	1347	1570	2690	2928	0.26	0.48
1.5Ni6 BFS	1349	1584	2707	2942	0.71	0.44
1.5Ni6 AFS	1349	1603	2708	2978	0.93	0.25

The other peaks that are relevant to the phosphate modes appeared at different wave numbers, such as 1049 cm^{-1} (ϑ_3 PO$_4$), 591 cm^{-1} (ϑ_4 PO$_4$), 433 cm^{-1} (ϑ_2 PO$_4$), and a weak band appeared at 273 cm^{-1}, which is assigned to Ca-PO$_4$(Yilmaz & Evis, 2014). The above results confirmed that the composite was composed of GNP and HA.

4.2.2 Microstructural and Mechanical Properties

The as-received graphene sheets used in this study were 1-20 nm in thickness and 1-50 μm in width. FESEM images of the raw graphene at both low and high magnifications are presented in Figure 4.17(a and b).
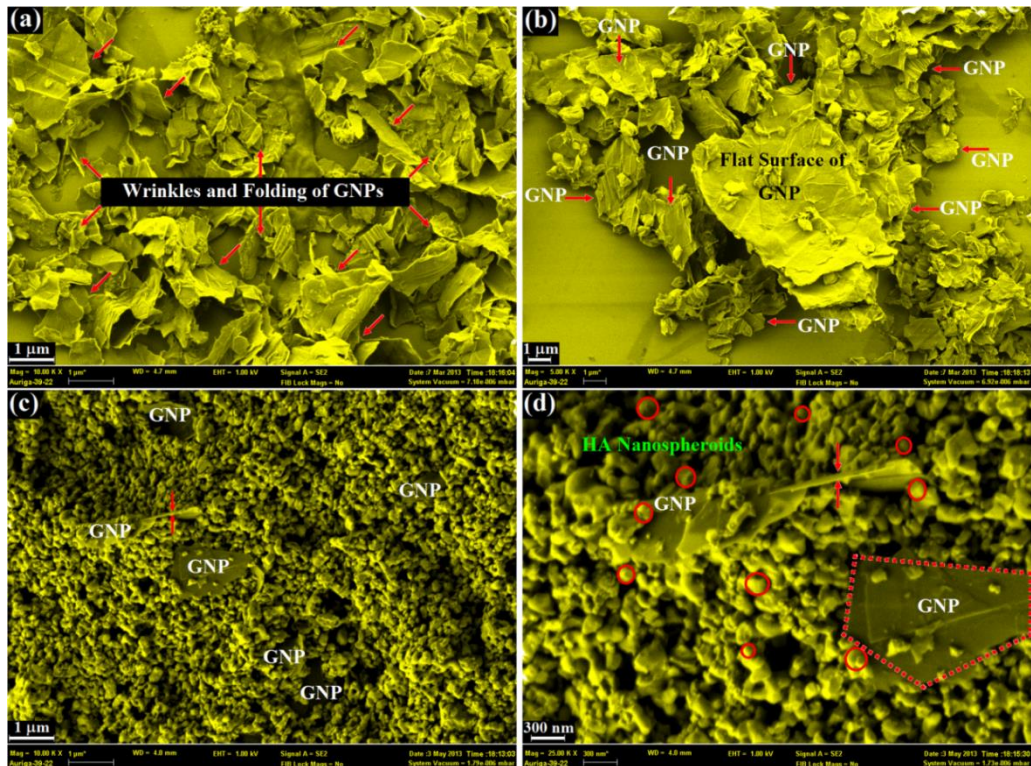
Figure 4.17 FESEM images of (a,b) GNPs and (c,d) 1.5Ni6.

It can be observed that the majority of the graphene sheets tend to agglomerate and were bundled together. In fact, several smaller graphene flakes are assembled into larger graphene blocks. In addition, the graphene sheets possess a large aspect ratio, which is the main factor for the intensification of the contact area with the other phases. The FESEM images indicate that the GNP are very thin with some wrinkles and folding (Yang et al., 2012; L. Zhang et al., 2013). Figure 4.17(c and d) show the typical microstructure of the 1.5Ni6 composite powder at both low and high magnification. As mentioned above, the calcined Ni6 powder as a matrix exhibited intrinsic expansion during the initial stage of thermal treatment. Finally, the grain coalescence and decrease in the number of grains occurred due to superficial diffusion and grain boundary sliding, respectively (Champion, 2013).

The FESEM images reveal the nanocrystalline nature of the composite powder and demonstrate that the specimens are composed of spheroidal particles with an average particle size of approximately 100 nm. Because HA granules with a smooth spherical geometry are helpful in osseointegration, the synthesized powder can be considered in bone tissue-engineering applications (Paul & Sharma, 1999). In addition, it is apparent that the graphene nanoplatelets are well distributed in the composite powder with improved mechanical behavior and biological responses (M. Gu et al., 2014). However, the particles exhibited a relatively high tendency to agglomerate. When two adjacent primary particles collide, coalescence may occur on the premise that these two particles share a common crystallographic orientation. As a result, the two primary particles attach to each other and combine to form a secondary particle. Because the sizes of the secondary particles are still very small, it is reasonable that the particles will continue to collide and coalesce. This behavior will ultimately lead to the agglomeration (Balaz, 2008; Bahman Nasiri-Tabrizi & Fahami, 2014).

To evaluate the distribution of GNPs in the composite structure, the cross-section of a typically sintered sample containing 1.5% GNPs (1.5Ni6) was examined (Figure 4.18). The FESEM micrographs show that apart from the distribution, the local contacts between the modified HA and the fully exfoliated graphene are obvious (Figure 4.18a).
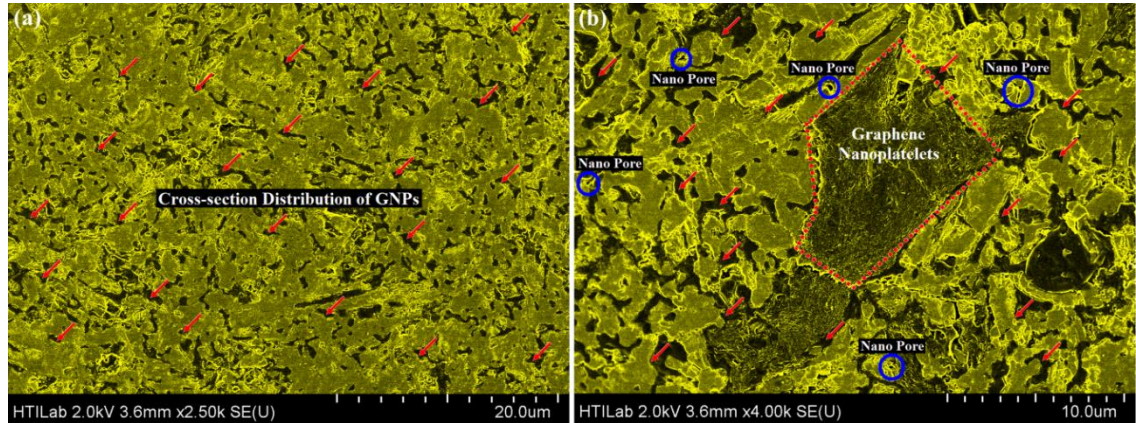
Figure 4.18 Cross-sectional image of a typical sintered sample containing 1.5% GNPs (1.5Ni6): (a) low and (b) high magnification.

The position of the embedded GNPs is indicated by the red arrows. This figure verifies the good dispersion of graphene nanoplatelets in the composite structure. Moreover, the cross-sectional view of the graphene laminates reveals stacks of graphene platelets that might affect the degree of mechanical improvement. To overcome this problem, further separation of aggregates as well as the prevention of the GNP agglomeration would be useful (Kun et al., 2012). As observed in Figure 4.18b, nano-scaled pores are formed during the sintering of the composite. It has been observed that an increase in the porosity of the HA composite might more or less deteriorate its mechanical properties. However, from the biological viewpoint, these nano-sized pores contribute to osteoblast in-growth of the composite (L. Zhang et al., 2013).

Table 4.5 Relative density and mechanical properties of the sintered samples.

Series	Relative density (%)	Elastic modulus (GPa)	Microhardness (GPa)	Fracture toughness (MPa m$^{0.5}$)
HA	97.13	53.20±3.41	2.98±0.06	0.94
Ni6	97.26	117.35±3.51	4.61±0.13	1.5
1.5Ni6	97.47	98.09±4.01	5.20±0.86	2.48

The relative density and mechanical properties of the samples (elastic modulus, hardness and fracture toughness) are summarized in Table 4.5. According to the presented data, the sintered monolithic HA, Ni6 and 1.5Ni6 composites exhibit high relative densities. All the samples are fully densified at 1150 ℃ and 160 MPa pressure during the HIP sintering. Previous reports demonstrated that the use of GNP as a reinforcement material has a significant effect on increasing or decreasing the relative density, which depends on the mixing process, sintering method and types of graphene. Zhao et al. (Y. Zhao et al., 2013) reported that the relative density of GNPs/BCP decreased with the addition of different ratios of GNPs compared with pure HA. Nieto et al. (Nieto et al., 2013) observed that with the addition of GNP to TaC, the densification of the composites increased to 60% compared with that of monolithic TaC. Govindaraajan et al. (Govindaraajan B Yadhukulakrishnan et al., 2013) reported that the reinforcement of GNPs favors the high densification of composites through the interfacial reaction, which can be retained in the composites sintered at high temperature.

However, there are no reports that discuss the effect of metal ions on the density of the dopant composites. Herein, the substitution of Ni in the HA lattice has little effect on the increase of the dopant composite density. However, the relative density of apatites may enhance the presence of GNPs such that the relative density of the 1.5Ni6 (1.5% GNPs) increased compared with the monolithic HA and Ni6. This behavior was due to the large surface area of the GNPs, which increases the surface diffusion during sintering. The measurement of the elastic modulus in bioceramic applications was performed using the nanoindentation technique in this experiment. The results revealed a significant increase in the E value for the Ni dopant by 220% over the monolithic HA. Based on our previous studies, at a very low concentration of graphene, the elastic modulus of composites improved compared with that of monolithic HA due to the

intrinsic properties of the graphene nanosheets, the homogenous distribution of GNPs in the matrix and strong Ni6/GNPs interfaces. All the samples exhibited high moduli of elasticity between graphene concentrations of 1-1.5 % in the composites. In a similar trend in Table 4.5, it is clearly observed that the elastic modulus of 1.5Ni6 (1.5% GNPs) increases to 184% compared with that of monolithic HA.

As mentioned previously (XRD data), severe HA decomposition occurred during the sintering of the composite (1.5Ni6) at 1150 °C due to the high thermal conductivity of the GNPs. Therefore, the coexistence of HA and β-TCP in the composite could explain the decrease of the elastic modulus in the composite sintered at 1150 °C. To calculate the hardness and fracture toughness values, micro-indentation (≥ 5 Kg) was conducted because indentation of presented composite did not generate a well-defined radial crack system. From Table 4.5, it is apparent that the Ni dopant increased the hardness as much as 155% due to its hard intrinsic properties compared with the monolithic HA. The microhardness improvement in 1.5Ni6 can be attributed to (i) the uniform dispersion of GNPs in the HA matrix, (ii) the prevention of localized plastic deformation due to presence of GNP and (iii) the small amount of porosity due to an appropriate sintering process. According to the results in Table 4.5, the Ni dopant plays a significant role in increasing the fracture toughness of the bulk samples. The Ni6 composite exhibits improved fracture toughness, which continuously increases to 263% in the 1.5Ni6 composite compared with the monolithic HA. As mentioned previously, severe HA decomposition occurred in 1.5Ni6. However, the fracture toughness of the composite increased due to the intrinsic properties of both β-TCP and the GNPs. The increased toughening of 1.5Ni6 is most likely due to the increase of closely spaced GNP structures resulting from the higher GNP amount (Nieto et al., 2013). It is notable that when the matrix crack is started and extended through the loading, the high strength of nanosheets plays a key role in the load transfer from the nanosheets to the path of crack

(J. Liu et al., 2012). Therefore, for increased effectiveness of GNP as a filler reinforcement to improve fracture toughness, intact GNP sheets must be efficiently bonded to the ceramic matrix (the interfacial friction in the interface) to carry the load (J. Liu et al., 2013; Kai Wang et al., 2011). In fact, the nature of the interfacial bonding between the GNPs and Ni6 affects the toughening response. It is believed that the fracture toughness of ceramics increases with additional resistance caused by the strong dragging forces from the GNP. The GNPs that are distributed along the grain boundaries are bent and embedded between the grains due to the force applied by their neighboring matrix grains during the solidification in the sintering process. The wrapping of GNPs in the intergranular region can be illustrated as follows: (I) the inhibition of grain growth during sintering and (II) increased resistance to crack propagation when several grains are wrapped together.

Figure 4.19(a-b) present the FESEM images of the fracture surfaces for the 1.5Ni6 composite. It is apparent that the grains are uniform throughout the fracture surface with a grain size approximately 350 nm and that the layered GNP surface is well expanded at the intergranular region and sandwiched between the individual Ni6 grains. The images also reveal that large GNPs are protruding out of the fracture surface and run along the grain boundaries of the matrix. The increase in the strength of 1.5Ni6 and the delay in the rupture of the composite matrix may be related to the absorption of more fracture energy during the pulling out of GNPs (Lahiri et al., 2013; Nieto et al., 2013; Walker et al., 2011). Previous reports mentioned an increased toughness value, which is attributed to various toughening mechanisms. Nieto et al. (Nieto et al., 2013) reported that the fracture toughness in the GNP composites increased due to the intrinsic energy dissipating mechanisms (sheet bending, kinking and sliding) of GNPs.
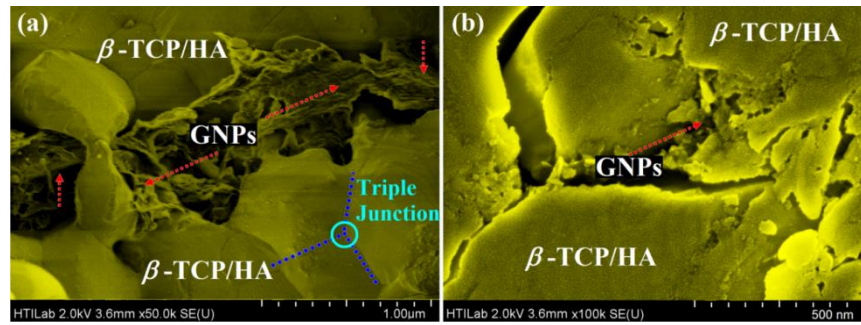
Figure 4.19 FESEM images showing the coexistence of HA and β-TCP in the 1.5Ni6 composite: (a) low and (b) high magnification.

In this study, various toughening mechanisms such as crack deflection, crack bridging and graphene necking, crack branching and pull out in radial cracks stemming from microhardness indents can be observed for the 1.5Ni6 composites (Figure 4.20). Crack deflection was observed at the interaction of the crack with larger GNPs, which resulted in deviation from its straight path. Due to the strength of the GNPs, the crack was not able to propagate through the nanosheets and therefore pursues a lower energy path and is arrested and deflected from the GNPs as observed in Figure 4.20a (Nieto et al., 2013; Walker et al., 2011). After the crack interaction with the larger and smaller GNPs, crack bridging could be observed.
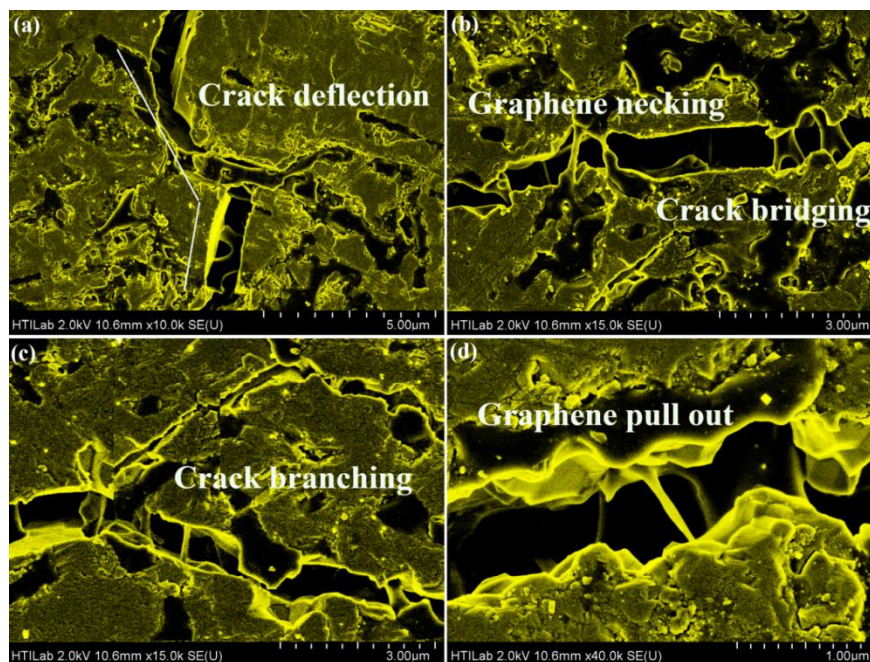
Figure 4.20 FESEM images of the various toughening mechanisms in the 1.5Ni6 composite: (a) crack deflection, (b) crack bridging, (c) crack branching, and (d) pull out.

Figure 4.20b shows a typical straight crack path with mechanisms of crack bridging and graphene necking. The effectiveness of crack bridging by the GNP is clearly visible in all the figures. In the crack line, sheet pull out and GNPs that are bridging the cracks can be observed. A similar pull out mechanism was also observed in Figure 4.19(a and b) and Figure 4.20d, where GNPs pull out from the matrix. We have frequently observed in our systems the pull-out of graphene sheets similar to that reported by other researchers (Kvetková et al., 2012; Kvetková et al., 2013). However, all the figures show the anchoring of GNPs between the cracks, which is relevant to the crack bridging toughening mechanism. The basis of these mechanisms is due to the interaction of the propagating crack and GNPs with different sizes. In addition, crack branching was observed in the composites, as shown in Figure 4.20c. The crack branching primarily occurred in various orientations to the main crack due to the increase of the outer applied load.

4.2.3 Biological Properties

Studies of the bone-biomaterials interface reveal that a common characteristic of bioactive materials is the consistent presence of an interfacial apatite layer. This can be reproduced *in-vitro* by immersion experiments using a simulated physiological solution that mimics the typical ion concentration in the body. In this study, bone like apatite formation on the surface of the samples was investigated *in-vitro* by immersion in SBF solution. The FESEM micrographs of the surface of samples, before and after immersion in the SBF are shown in Figure 4.21(a-i). After 7 days of immersion, HA pure surface (Figure 4.21(b and c)) appeared to be covered by a newly formed layer, which was chemically similar to apatite based on EDS analysis. Figure 4.21(e and f) shows the apatite formation on the surface of the Ni6. As can be seen, numerous tiny spherical crystals precipitate on the surface of the sample separately or as an appetite

cluster which they did not densely cover the entire surface of Ni6. In compare, the 1.5Ni6 composite (Figure 4.21(h and i)) shows the well covered apatite on the surface in presence of GNP which exhibit the ability to induce apatite formation on its surface only after 7 days in SBF. The significance different observations between the apatite layer growth on the surface of the samples are relevant to their morphologies which are agreed with the observations made by several research groups (Cui et al., 2011; Janković et al., 2015; L. Zhang et al., 2013). For instance, based on our recent study, the results showed that the apatite morphology varied among different rGO-containing calcium silicate (CS) ceramics. This morphological difference was attributed to changes in the ion concentrations and pH in SBF after the soaking of different rGO-containing CS ceramics (Mehrali et al., 2014a, 2014b).
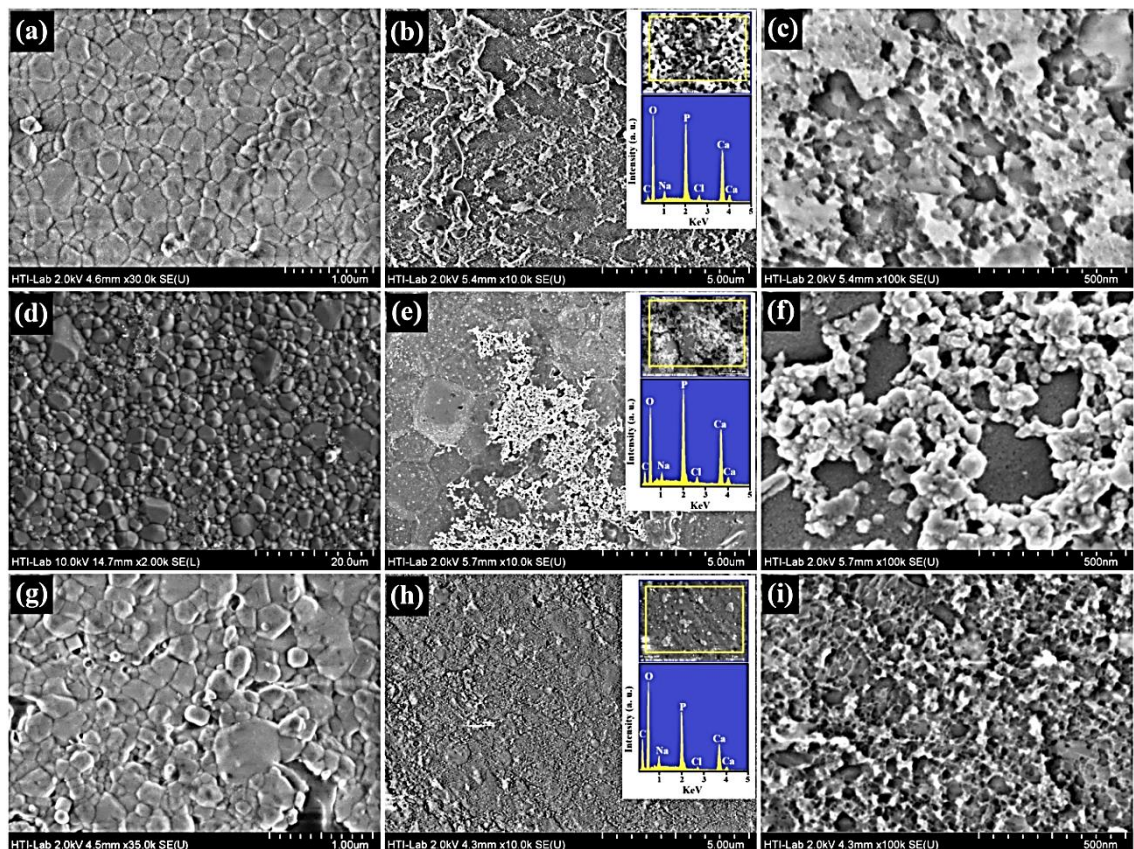
Figure 4.21 FESEM images of the samples (a, d and g) before and (b and c) pure HA, (e and f) Ni6 and (h and i) 1.5Ni6 after 7 days soaking in the SBF solution.

In addition, the EDS spectra shown in Figure 4.21, detected the elements which were mainly Ca and P peaks. Analyzing the Ca/P molar ratio of the apatite formed on the HA, Ni6 and 1.5Ni6 composites showed a range of 1.85 and 1.52 which is close to HA (1.67), suggesting that apatite formed on the samples. The fact of apatite formation on 1.5Ni6 indicates that this composite ceramic has good bioactivity in compare to Ni6. For more understanding of apatite mineralization mechanisms, previous researcher mentioned to two possible mechanisms explained for the apatite forming ability of HA-based materials (Janković et al., 2015). (i) First mechanism is based on the surface charge. To brief, the negative surface charges of HA (PO_4^{3-} and OH^-) interact with the positively charged Ca^{2+} ions in SBF forming Ca-rich amorphous calcium phosphate (ACP) on the surface. These Ca-rich ACP then interact with the negatively charged phosphate ions in SBF to form Ca-deficient ACP, which finally crystallize into bone-like apatite deposits on HA surface (H.-M. Kim et al., 2005). Fan et al. (Fan et al., 2014), Zhang et al. (L. Zhang et al., 2013) and Girija et al. have indicated the apatite forming ability of heavy ions irradiated HA and HA/GNP composites based on this mechanism. (ii) Another mechanism is related to the dissolution properties (Kumar et al., 2012) where dissolution of HA at physiological conditions releases Ca^{2+} and PO_4^{3-} ions into the surrounding fluid, resulting in precipitation of bone-like apatite on its surface.

This process may be promoted or inhibited depending on the surrounding fluid and structural properties of HA. Previous researchers showed that the replacement of partial Ca^{2+} in HA by different cationic metal ions can change dissolution behavior and growth kinetics. For example, the dissolution behavior of strontium (Sr)-doped HA in proper amount was investigated. The results showed that this changing in structure of HA led to introduce more lattice distortion which increased its solubility. In fact, the dissolution of Sr-HA results in the release of Ca^{2+}, enhancing the ionic activity product

of the apatite in surrounding fluid and inducing apatite precipitation. In addition, it has been reported that, the solubility of these apatites intensified with the increasing the Sr content (Christoffersen et al., 1997; Demin et al., 2001; Xue et al., 2006). Some researcher also investigated the effect of zinc (Zn) incorporated in HA for apatite formability. They found that Zn- HA shows more dissolution than HA whereas its apatite forming ability was less than HA. These results may be due to the inhibition of apatite formation by the Zn ions which is released along with calcium and phosphate ions during dissolution process (Hoppe et al., 2011).

The *in-vitro* assessment of the biocompatibility of HA, Ni6 and Ni6/GNP composites was conducted by culturing osteoblasts on the surface of the samples and assessing their viability and proliferation kinetics. The proliferation of the osteoblast cells was evaluated qualitatively by observing the population of FDA stained live cells on the surface of HA, Ni6 and 1.5Ni6 composites using fluorescence microscopy. The growth and proliferation of osteoblast cells on an implant surface are particularly significant for bone regeneration and integration (Shirazi et al., 2014). In general, an osteoblast attaches initially to the orthopedic implant surface and covers the implant surface by proliferation and growth due to collagen deposition in the intercellular region, known as an osteoid (Mehrali et al., 2014b). The confocal microscopy images in Figure 4.22 show the live cells in green on HA and its composite surface after 1, 3, and 5 days of growth. The cells in the images show the typical lens-shaped characteristic of the live osteoblasts with normal cell growth behavior. As observed in the monolithic HA, after 3 days of culture (Figure 4.22b), the cells became more confluent and started forming dense islands. After 5 days of growth, the cell population increased and covered the surface of the sample (Figure 4.22c).
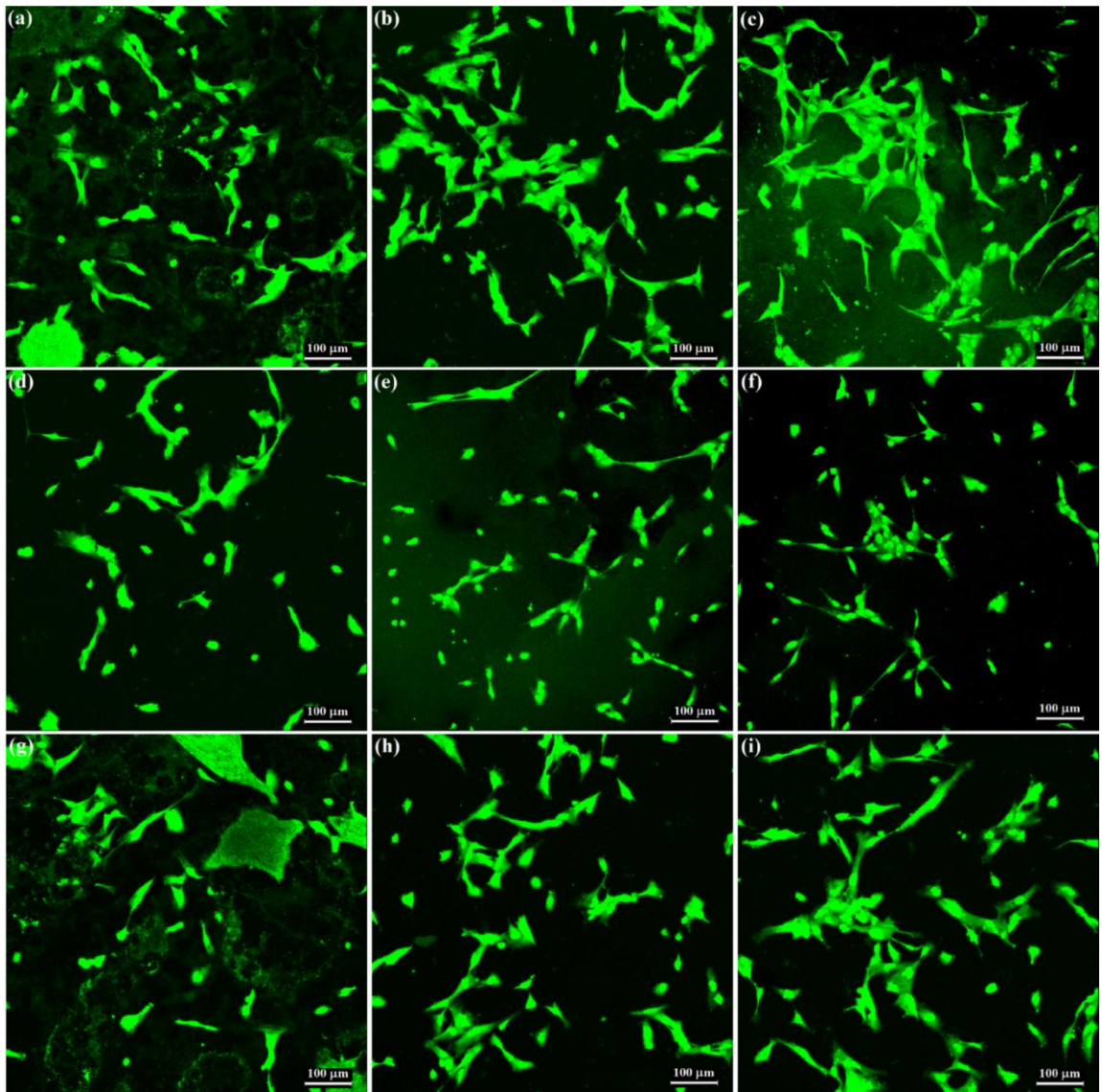
Figure 4.22 Confocal microscopy images of the specimens after 1, 3 and 5 days of culture: (a-c) HA, (d-f) Ni6 and (g-i) 1.5Ni6.

The increase of osteoblast cells with time indicates an increase in the cell proliferation and/or survival on the sample surfaces. In comparison, the cell population of the Ni6 samples was severely decreased on the first day but increased gradually on the fifth day. This finding indicates that the presence of Ni ions increased the cytotoxicity (Figure 4.22f). The two main factors contributing to the cytotoxicity are: (i) Ni ions may bind to DNA-repair enzymes and hinder the cell mitosis by disrupting the DNA repair, replication and recombination and (ii) Ni ions also generate oxygen-free radicals to cause protein degradation in situ. These adverse effects might be proportional to the Ni ion concentration in the medium (Shiao et al., 1998).
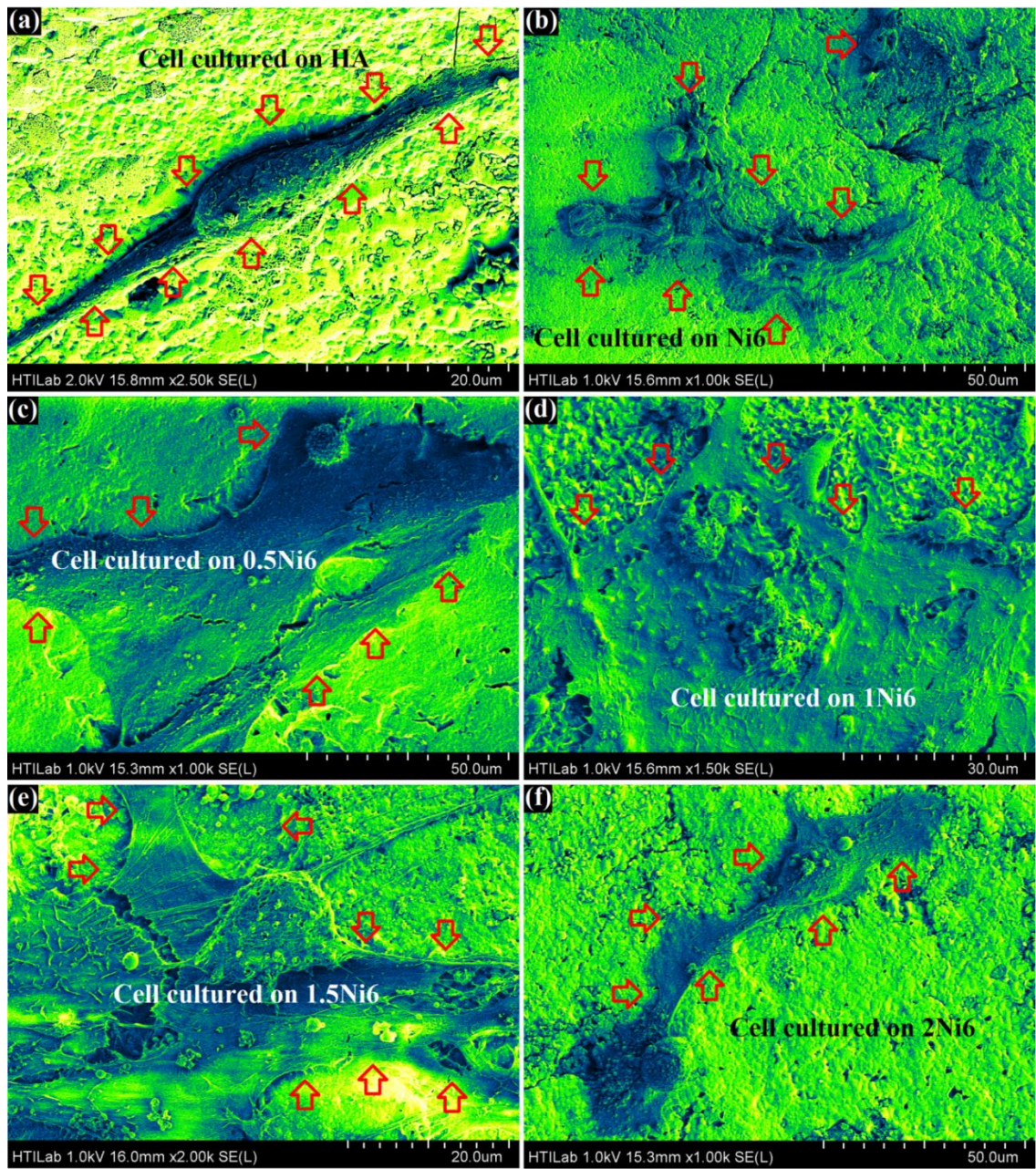
Figure 4.23 FESEM images of the osteoblast cell morphology after 1 day of culture: (a) monolithic HA, (b) Ni6, (c) 0.5Ni6, (d) 1Ni6, (e) 1.5Ni6, and (f) 2Ni6.

The effect of GNPs on the growth and proliferation of osteoblast cells was continuously assessed qualitatively by observing the population of osteoblast cells on the surface of the 1.5Ni6 after different days of culture. Studies on the biocompatibility of HA/GNP composites by other research groups have suggested that the presence of GNP in HA promotes osteoblast cell proliferation. In a similar trend, Figure 4.22(g-i) indicates that with the addition of 1.5% GNP to Ni6, the population and proliferation of

the osteoblast cells increased from 1 to 3 days compared with Ni6. After 5 days of culture, a similar population and densification of osteoblast cells was observed in the 1.5Ni6 composite compared with HA. This observation indicates that the HA and 1.5Ni6 surfaces are suitable for osteoblast cell proliferation. Figure 4.23(a-f) show the osteoblast cell morphology on the monolithic HA, Ni6 and Ni6/GNP composites with different ratios of GNP after 1 day of culture. The FESEM images reveal that the hFOB cells on all the samples were polygonal or widespread in shape, with fine filopodia, globular, flat and abundant surface folds in each group.
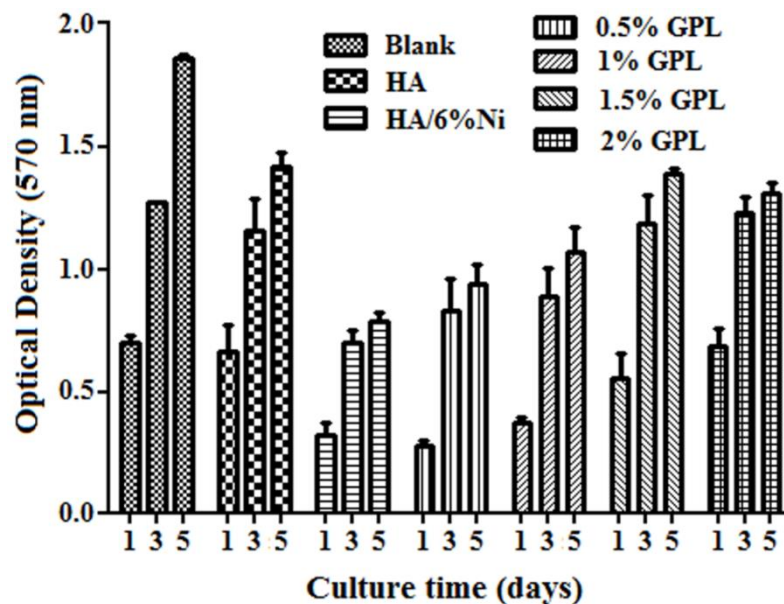
Figure 4.24 Proliferation of the hFOB cells cultured on the sintered sample surfaces.

To obtain clear insight into the effect of the addition of Ni dopant and GNP on the cell response, cytotoxicity and biocompatibility of the Ni6 and 1.5Ni6, these samples were examined by MTT. The proliferation and viability of the osteoblast cells were assessed on HA, Ni6 and Ni6/GNP surfaces after in-vitro culturing for 1, 3 and 5 days. The optical density (OD) was measured at 570 nm in an ultra-violet visible light spectrophotometer. Figure 4.24 shows that the OD value decreased with time when the osteoblast cells were cultured with Ni6 compared with HA, which indicates that Ni6 has a negative effect on cell viability and proliferation. Clearly, the OD value could improve

the viability of osteoblasts during the initial addition of GNP (0.5 wt %). This finding suggests that the GNP could promote the viability of the osteoblast cells. The optimum positive effect of GNP as a reinforcement for cell viability and proliferation is observed for 1.5Ni6, which exhibits a similar OD value as HA after 5 days of culture.

Chapter V: CONCLUSIONS AND SUGGESTIONS FOR FUTURE WORK

5.1   Conclusion

This dissertation presents a complete analysis of HA composites, in terms of synthesis, mechanical and biological behavior for orthopedic applications. Investigations on free standing HA composites reveal excellent improvement in the fracture toughness, hardness and modulus elasticity. *In-vitro* biocompatibility studies suggest a non-cytotoxic response of GNS along with a positive influence on bone cell activity. The specific conclusions on performance of HA composites are listed below:

➢ HA composites powders were synthesized via hydrothermal (nHA/rGO) and wet precipitation (HA-Ni) method in different electrolytes.

➢ The calcination process was performed by a precipitation method which was carried out at 900 °C for 1 h. No phase transformation or decomposition occurred after the calcination of the HA-Ni powder.

➢ Both types of composites were sintered by HIP process at 1150°C and 160 MPa for 1h.

i.   In case of nHA/rGO, the results proved that HA does not dissociate into TCP and CaO during the HIP process. Also, rGO do not show any negative effect on phase transformation, due to the high thermal conductivity of GNS, and uniform densification of nHA structure occurred during HIP process.

ii.   In case of Ni-HA/GNP, thermal treatment shows a significant effect on phase transformation after doping with Ni, because the decomposition was enhanced with the presence of minute impurities or non-stoichiometric compositions in the HA powders. With the addition of 6% Ni, the decomposition of HA to β-TCP and CaO was identified and consequently, in

the presence of 1.5% GNPs (1.5Ni6), decomposition of HA significantly increased the β-TCP, due to the presence of GNPs in the composite, a thermal gradient was created between the GNPs and HA, which results in a severe decomposition.

➤ Compared to the pristine HA, the composites show improvements in both their mechanical and biological properties as follows:

i. The results indicate that the elastic modulus and fracture toughness of the sintered samples increased by 86% and 40%, respectively, with increasing rGO content, compared to nHA.

ii. The hardness and fracture toughness increased by 55% and 75% and 59% and 163% for Ni6 and 1.5Ni6, respectively, compared with the monolithic HA. Moreover, the elastic modulus of the composite samples of Ni6 and 1.5Ni6, was increased by 120% and 85%, respectively, compared to the monolithic HA.

iii. Increasing the fracture toughness in both type of composite is imperative for good interfacial bonding between the GNS and HA matrix.

iv. The various toughening mechanisms such as crack deflection, crack bridging and graphene necking, crack branching and pull out in radial cracks stemming from microhardness indents were observed. The increase in the strength of composites and the delay in the rupture of the composite matrix related to the absorption of more fracture energy, which leads to fracture toughening of HA with GNS composite reinforcement.

➤ The cell culture and viability test results show that:

i. The addition of the rGO promoted the osteoblast adhesion and proliferation. The biocompatibility of the nHA/rGO composite for different cell culture times was enhanced by increasing the rGO content.

ii.   The biological properties indicated that the cytotoxicity of the Ni was improved with the addition of GNPs. The biological tests confirmed h-FOB osteoblast cell growth on the surface of the composite samples after 1, 3 and 5 days of culture. In addition, the effect of the GNPs on the growth and proliferation of the osteoblast cells was investigated in the Ni6 composite with different ratios of GNPs, where 1.5 wt.% was the optimum concentration.

5.2   Suggestions for Future Work

The aim of the current research was to explore the potential of HA and doped HA with different morphology/GNS composites. The criteria for judgment were the effect of GNS and metal ion doped reinforcement HA on mechanical and biological behavior of the composite. The findings of this study establish HA, HA/rGO and HA doped Ni/GNP composites are potential alternatives for clinical applications of HA. However, some of the topic need further investigations for the clinical translation of these composites.

Biocompatibility Evaluation for HA/GNS

HA/GNS was evaluated thoroughly for its biocompatibility in the present study, including *in-vitro* studies for osteoblast proliferation rate, viability, differentiation, mineralization. However, more biocompatibility studies (both *in-vitro* and *in-vivo*) are required to establish HA/GNS composites for orthopedic applications. In real life, the implants are in the living body for >15 years, in most of the cases. It is therefore important to assess the fate of HA/GNS composites, for longer *in-vivo* exposure, to assure their safe use. A systematic study of implanting HA/GNS composite in animal model for longer exposure period (3 months, 6 months and 1 year) followed by histocompatibility studies is recommended.

REFERENCES

Afzal, M. A. F., Kalmodia, S., Kesarwani, P., Basu, B., & Balani, K. (2013). Bactericidal effect of silver-reinforced carbon nanotube and hydroxyapatite composites. *Journal of Biomaterials Applications, 27*(8), 967-978.

Ahn, E. S., Gleason, N. J., Nakahira, A., & Ying, J. Y. (2001). Nanostructure processing of hydroxyapatite-based bioceramics. *Nano Letters, 1*(3), 149-153.

Ahymah Joshy, M., Elayaraja, K., Suganthi, R., Chandra Veerla, S., & Kalkura, S. N. (2011). In vitro sustained release of amoxicillin from lanthanum hydroxyapatite nano rods. *Current Applied Physics, 11*(4), 1100-1106.

Albee, F. H. (1920). Studies in bone growth: triple calcium phosphate as a stimulus to osteogenesis. *Annals of surgery, 71*(1), 32.

Aminian, A., Solati-Hashjin, M., Samadikuchaksaraei, A., Bakhshi, F., Gorjipour, F., Farzadi, A., Moztarzadeh, F., & Schmücker, M. (2011). Synthesis of silicon-substituted hydroxyapatite by a hydrothermal method with two different phosphorous sources. *Ceramics International, 37*(4), 1219-1229.

Anstis, G., Chantikul, P., Lawn, B. R., & Marshall, D. (1981). A critical evaluation of indentation techniques for measuring fracture toughness: I, direct crack measurements. *Journal of the American Ceramic Society, 64*(9), 533-538.

Antonakos, A., Liarokapis, E., & Leventouri, T. (2007). Micro-Raman and FTIR studies of synthetic and natural apatites. *Biomaterials, 28*(19), 3043-3054.

Aoki, H. (1994). *Medical applications of hydroxyapatite*: Ishiyaku EuroAmerica, Incorporated.

Balani, K., Lahiri, D., Keshri, A. K., Bakshi, S., Tercero, J. E., & Agarwal, A. (2009). The nano-scratch behavior of biocompatible hydroxyapatite reinforced with aluminum oxide and carbon nanotubes. *JOM Journal of the Minerals Metals and Materials Society, 61*(9), 63-66.

Balaz, P. (2008). *Mechanochemistry in nanoscience and minerals engineering*: Springer.

Bandyopadhyay, A., Bernard, S., Xue, W., & Bose, S. (2006). Calcium Phosphate-Based Resorbable Ceramics: Influence of MgO, ZnO, and SiO2 Dopants. *Journal of the American Ceramic Society, 89*(9), 2675-2688.

Basar, B., Tezcaner, A., Keskin, D., & Evis, Z. (2010). Improvements in microstructural, mechanical, and biocompatibility properties of nano-sized hydroxyapatites doped with yttrium and fluoride. *Ceramics International, 36*(5), 1633-1643.

Berger, C., Song, Z., Li, X., Wu, X., Brown, N., Naud, C., Mayou, D., Li, T., Hass, J., & Marchenkov, A. N. (2006). Electronic confinement and coherence in patterned epitaxial graphene. *Science, 312*(5777), 1191-1196.

Best, S., Porter, A., Thian, E., & Huang, J. (2008). Bioceramics: past, present and for the future. *Journal of the European Ceramic Society, 28*(7), 1319-1327.

Blokhuis, T. J., Termaat, M. F., den Boer, F. C., Patka, P., Bakker, F. C., & Henk, J. T. M. (2000). Properties of calcium phosphate ceramics in relation to their in vivo behavior. *Journal of Trauma-Injury, Infection, and Critical Care, 48*(1), 179.

Boehm, H.-P., Clauss, A., Fischer, G., & Hofmann, U. (1962). Das Adsorptionsverhalten sehr dünner Kohlenstoff-Folien. *Zeitschrift fur Anorganische und Allgemeine Chemie, 316*(3-4), 119-127.

Boehm, H.-P., & Stumpp, E. (2007). Citation errors concerning the first report on exfoliated graphite. *Carbon, 45*(7), 1381-1383.

Bohner, M. (2000). Calcium orthophosphates in medicine: from ceramics to calcium phosphate cements. *Injury, 31*, D37-D47.

Bonel, G., HEUGHEBAERT, J. C., Heughebaert, M., Lacout, J. L., & Lebugle, A. (1988). Apatitic calcium orthophosphates and related compounds for biomaterials preparation. *Annals of the New York Academy of Sciences, 523*(1), 115-130.

Bonner, M., Ward, I., McGregor, W., Tanner, K., & Bonfield, W. (2001). Hydroxyapatite/polypropylene composite: a novel bone substitute material. *Journal of Materials Science Letters, 20*(22), 2049-2051.

Brodie, B. C. (1859). On the atomic weight of graphite. *Philosophical Transactions of the Royal Society of London*, 249-259.

Burdick, J. A., & Mauck, R. L. (2011). *Biomaterials for Tissue Engineering Applications*: Springer.

Cao, L.-y., Zhang, C.-b., & Huang, J.-f. (2005). Synthesis of hydroxyapatite nanoparticles in ultrasonic precipitation. *Ceramics International, 31*(8), 1041-1044.

Capuccini, C., Torricelli, P., Boanini, E., Gazzano, M., Giardino, R., & Bigi, A. (2009). Interaction of Sr-doped hydroxyapatite nanocrystals with osteoclast and osteoblast-like cells. *Journal of Biomedical Materials Research Part A, 89A*(3), 594-600. doi:10.1002/jbm.a.31975

Carta, D., Pickup, D. M., Knowles, J. C., Smith, M. E., & Newport, R. J. (2005). Sol–gel synthesis of the P_2O_5–CaO–Na_2O–SiO_2 system as a novel bioresorbable glass. *Journal of Materials Chemistry, 15*(21), 2134-2140.

Centeno, A., Rocha, V., Alonso, B., Fernández, A., Gutierrez-Gonzalez, C. F., Torrecillas, R., & Zurutuza, A. (2013). Graphene for tough and electroconductive alumina ceramics. *Journal of the European Ceramic Society, 33*(15), 3201-3210.

Champion, E. (2013). Sintering of calcium phosphate bioceramics. *Acta Biomaterialia, 9*(4), 5855-5875.

Champion, E., Gautier, S., & Bernache-Assollant, D. (1996). Characterization of hot pressed Al_2O_3-platelet reinforced hydroxyapatite composites. *Journal of Materials Science: Materials in Medicine, 7*(2), 125-130.

Chandanshive, B. B., Rai, P., Rossi, A. L., Ersen, O., & Khushalani, D. (2013). Synthesis of hydroxyapatite nanotubes for biomedical applications. *Materials Science and Engineering: C, 33*(5), 2981-2986.

Chen, B., Zhang, T., Zhang, J., Lin, Q., & Jiang, D. (2008). Microstructure and mechanical properties of hydroxyapatite obtained by gel-casting process. *Ceramics International, 34*(2), 359-364.

Chen, C., Huang, Z., Yuan, W., Li, J., Cheng, X., & Chi, R.-a. (2011). Pressure effecting on morphology of hydroxyapatite crystals in homogeneous system. *CrystEngComm, 13*(5), 1632-1637.

Chen, F., Huang, P., Zhu, Y.-J., Wu, J., Zhang, C.-L., & Cui, D.-X. (2011). The photoluminescence, drug delivery and imaging properties of multifunctional Eu^{3+}/Gd^{3+} dual-doped hydroxyapatite nanorods. *Biomaterials, 32*(34), 9031-9039.

Chen, F., Zhu, Y.-J., Wang, K.-W., & Zhao, K.-L. (2010). Surfactant-free solvothermal synthesis of hydroxyapatite nanowire/nanotube ordered arrays with biomimetic structures. *CrystEngComm, 13*(6), 1858-1863.

Chen, F., Zhu, Y.-J., Wang, K.-W., & Zhao, K.-L. (2011). Surfactant-free solvothermal synthesis of hydroxyapatite nanowire/nanotube ordered arrays with biomimetic structures. *CrystEngComm, 13*(6), 1858-1863.

Chen, W., Yan, L., & Bangal, P. (2010). Chemical reduction of graphene oxide to graphene by sulfur-containing compounds. *The Journal of Physical Chemistry C, 114*(47), 19885-19890.

Chen, W., Yan, L., & Bangal, P. R. (2010). Preparation of graphene by the rapid and mild thermal reduction of graphene oxide induced by microwaves. *Carbon, 48*(4), 1146-1152.

Chen, Y., Zhang, T., Gan, C., & Yu, G. (2007). Wear studies of hydroxyapatite composite coating reinforced by carbon nanotubes. *Carbon, 45*(5), 998-1004.

Chen, Y., Zhang, Y., Zhang, T., Gan, C., Zheng, C., & Yu, G. (2006). Carbon nanotube reinforced hydroxyapatite composite coatings produced through laser surface alloying. *Carbon, 44*(1), 37-45.

Chen, Y., Zheng, X., Xie, Y., Ji, H., Ding, C., Li, H., & Dai, K. (2010). Silver release from silver-containing hydroxyapatite coatings. *Surface and Coatings Technology, 205*(7), 1892-1896.

Cheng, K., Zhang, S., & Weng, W. (2005). The F content in sol–gel derived FHA coatings: an XPS study. *Surface and Coatings Technology, 198*(1), 237-241.

Cheng, K., Zhang, S., Weng, W., & Zeng, X. (2005). The interfacial study of sol–gel-derived fluoridated hydroxyapatite coatings. *Surface and Coatings Technology, 198*(1), 242-246.

Cheng, M., Yang, R., Zhang, L., Shi, Z., Yang, W., Wang, D., Xie, G., Shi, D., & Zhang, G. (2012). Restoration of graphene from graphene oxide by defect repair. *Carbon, 50*(7), 2581-2587.

Cholewa-Kowalska, K., Kokoszka, J., Łączka, M., Niedźwiedzki, Ł., Madej, W., & Osyczka, A. M. (2009). Gel-derived bioglass as a compound of hydroxyapatite composites. *Biomedical Materials, 4*(5), 055007.

Christoffersen, J., Christoffersen, M. R., Kolthoff, N., & Bärenholdt, O. (1997). Effects of strontium ions on growth and dissolution of hydroxyapatite and on bone mineral detection. *Bone, 20*(1), 47-54.

Coathup, M. J., Blackburn, J., Goodship, A. E., Cunningham, J. L., Smith, T., & Blunn, G. W. (2005). Role of hydroxyapatite coating in resisting wear particle migration and osteolysis around acetabular components. *Biomaterials, 26*(19), 4161-4169.

Cox, S. C., Jamshidi, P., Grover, L. M., & Mallick, K. K. (2014). Preparation and characterisation of nanophase Sr, Mg, and Zn substituted hydroxyapatite by aqueous precipitation. *Materials Science and Engineering: C, 35*, 106-114.

Cui, P., Lee, J., Hwang, E., & Lee, H. (2011). One-pot reduction of graphene oxide at subzero temperatures. *Chemical Communications, 47*(45), 12370-12372.

Curran, D., Fleming, T., Kawachi, G., Ohtsuki, C., & Towler, M. (2009). Characterisation and mechanical testing of hydrothermally treated HA/ZrO2 composites. *Journal of Materials Science: Materials in Medicine, 20*(11), 2235-2241.

Dang, T. T., Pham, V. H., Hur, S. H., Kim, E. J., Kong, B.-S., & Chung, J. S. (2012). Superior dispersion of highly reduced graphene oxide in N, N-dimethylformamide. *Journal of Colloid and Interface Science, 376*(1), 91-96.

Dasgupta, S., Banerjee, S. S., Bandyopadhyay, A., & Bose, S. (2010). Zn-and Mg-doped hydroxyapatite nanoparticles for controlled release of protein. *Langmuir, 26*(7), 4958-4964.

De Aza, A., Chevalier, J., Fantozzi, G., Schehl, M., & Torrecillas, R. (2002). Crack growth resistance of alumina, zirconia and zirconia toughened alumina ceramics for joint prostheses. *Biomaterials, 23*(3), 937-945.

De Jong, W. (1926). La substance minerale dans les os. *Recueil des Travaux Chimiques des Pays-Bas, 45*(6), 445-448.

Demin, C., Yuanfei, F., Guozhen, G., Yunfang, Q., & Yunfen, G. (2001). Preparation and solubility of the solid solution of strontium substituted hydroxyapatite. *Chinese Journal of Biomedical Engineering, 20*(3), 278-280.

Dorozhkin, S. V. (2010). Bioceramics of calcium orthophosphates. *Biomaterials, 31*(7), 1465-1485.

Dorozhkin, S. V. (2013). Calcium orthophosphate-based bioceramics. *Materials, 6*(9), 3840-3942.

Dreyer, D. R., Park, S., Bielawski, C. W., & Ruoff, R. S. (2010). The chemistry of graphene oxide. *Chemical Society Reviews, 39*(1), 228-240.

Ducheyne, P., Radin, S., & King, L. (1993). The effect of calcium phosphate ceramic composition and structure on in vitro behavior. I. Dissolution. *Journal of biomedical materials research, 27*(1), 25-34.

Dusza, J., Morgiel, J., Duszová, A., Kvetková, L., Nosko, M., Kun, P., & Balázsi, C. (2012). Microstructure and fracture toughness of Si_3N_4+graphene platelet composites. *Journal of the European Ceramic Society, 32*(12), 3389-3397.

Dusza, J., Morgiel, J., Duszová, A., Kvetková, L., Nosko, M., Kun, P., & Balázsi, C. (2012). Microstructure and fracture toughness of Si_3N_4 + graphene platelet composites. *Journal of the European Ceramic Society, 32*(12), 3389-3397.

Eizenberg, M., & Blakely, J. (1979). Carbon monolayer phase condensation on Ni (111). *Surface Science, 82*(1), 228-236.

Elias, K. L., Price, R. L., & Webster, T. J. (2002). Enhanced functions of osteoblasts on nanometer diameter carbon fibers. *Biomaterials, 23*(15), 3279-3287.

Elliott, J. C. (1994). Structure and chemistry of the apatites and other calcium orthophosphates. *Studies in organic chemistry*.

Ellis, D., Terra, J., Warschkow, O., Jiang, M., González, G. B., Okasinski, J., Bedzyk, M., Rossi, A. M., & Eon, J.-G. (2006). A theoretical and experimental study of lead substitution in calcium hydroxyapatite. *Physical Chemistry Chemical Physics, 8*(8), 967-976.

Ergun, C. (2011). Enhanced phase stability in hydroxylapatite/zirconia composites with hot isostatic pressing. *Ceramics International, 37*(3), 935-942.

Evan, A., & Charles, E. (1976). Fracture toughness determination by indentation. *J. Am. Ceram. Soc, 59*(7/8), 371-372.

Fan, H., Wang, L., Zhao, K., Li, N., Shi, Z., Ge, Z., & Jin, Z. (2010). Fabrication, mechanical properties, and biocompatibility of graphene-reinforced chitosan composites. *Biomacromolecules, 11*(9), 2345-2351.

Fan, Y., Wang, L., Li, J., Li, J., Sun, S., Chen, F., Chen, L., & Jiang, W. (2010). Preparation and electrical properties of graphene nanosheet/Al_2O_3 composites. *Carbon, 48*(6), 1743-1749.

Fan, Z., Wang, J., Wang, Z., Ran, H., Li, Y., Niu, L., Gong, P., Liu, B., & Yang, S. (2014). One-pot synthesis of graphene/hydroxyapatite nanorod composite for tissue engineering. *Carbon, 66*, 407-416.

Fathi, M., & Hanifi, A. (2007). Evaluation and characterization of nanostructure hydroxyapatite powder prepared by simple sol–gel method. *Materials Letters, 61*(18), 3978-3983.

Fathi, M., & Mohammadi Zahrani, E. (2009). Mechanical alloying synthesis and bioactivity evaluation of nanocrystalline fluoridated hydroxyapatite. *Journal of Crystal Growth, 311*(5), 1392-1403.

Feng, W., Mu-Sen, L., Yu-Peng, L., & Yong-Xin, Q. (2005). A simple sol–gel technique for preparing hydroxyapatite nanopowders. *Materials Letters, 59*(8), 916-919.

Ferrari, A., Meyer, J., Scardaci, V., Casiraghi, C., Lazzeri, M., Mauri, F., Piscanec, S., Jiang, D., Novoselov, K., & Roth, S. (2006). Raman spectrum of graphene and graphene layers. *Physical Review Letters, 97*(18), 187401.

Ferrari, A., & Robertson, J. (2000). Interpretation of Raman spectra of disordered and amorphous carbon. *Physical review B, 61*(20), 14095.

Gao, J., Liu, F., Liu, Y., Ma, N., Wang, Z., & Zhang, X. (2010). Environment-friendly method to produce graphene that employs vitamin C and amino acid. *Chemistry of Materials, 22*(7), 2213-2218.

Gauthier, O., Goyenvalle, E., Bouler, J.-M., Guicheux, J., Pilet, P., Weiss, P., & Daculsi, G. (2001). Macroporous biphasic calcium phosphate ceramics versus injectable bone substitute: a comparative study 3 and 8 weeks after implantation in rabbit bone. *Journal of Materials Science: Materials in Medicine, 12*(5), 385-390.

Geetha, M., Singh, A., Asokamani, R., & Gogia, A. (2009). Ti based biomaterials, the ultimate choice for orthopaedic implants–A review. *Progress in Materials Science, 54*(3), 397-425.

Ghanaati, S., Barbeck, M., Detsch, R., Deisinger, U., Hilbig, U., Rausch, V., Sader, R., Unger, R. E., Ziegler, G., & Kirkpatrick, C. J. (2012). The chemical composition of synthetic bone substitutes influences tissue reactions in vivo: histological and histomorphometrical analysis of the cellular inflammatory response to hydroxyapatite, beta-tricalcium phosphate and biphasic calcium phosphate ceramics. *Biomedical Materials, 7*(1), 015005.

Gras, P., Ratel-Ramond, N., Teychene, S., Rey, C., Elkaim, E., Biscans, B., Sarda, S., & Combes, C. (2014). Structure of the calcium pyrophosphate monohydrate phase ($Ca_2P_2O_7 \cdot H_2O$): towards understanding the dehydration process in calcium pyrophosphate hydrates. *Acta Crystallographica Section C: Structural Chemistry, 70*(9), 862-866.

Gu, M., Liu, Y., Chen, T., Du, F., Zhao, X., Xiong, C., & Zhou, Y. (2014). Is graphene a promising nano-material for promoting surface modification of implants or scaffold materials in bone tissue engineering? *Tissue Engineering - Part B: Reviews, 20*(5), 477-491.

Gu, Y., Khor, K., & Cheang, P. (2004). Bone-like apatite layer formation on hydroxyapatite prepared by spark plasma sintering (SPS). *Biomaterials, 25*(18), 4127-4134.

Guerra-López, J., Pomes, R., Della Védova, C., Vina, R., & Punte, G. (2001). Influence of nickel on hydroxyapatite crystallization. *Journal of Raman Spectroscopy, 32*(4), 255-261.

Gupta, A., Tripathi, G., Lahiri, D., & Balani, K. (2013). Compression Molded Ultra High Molecular Weight Polyethylene–Hydroxyapatite–Aluminum Oxide–Carbon Nanotube Hybrid Composites for Hard Tissue Replacement. *Journal of Materials Science & Technology, 29*(6), 514-522.

Hench, L. (1993). Bioceramics: from concept to clinic. *American Ceramic Society Bulletin, 72*(4), 93-98.

Hench, L. L., & Ethridge, E. (1972). Biomaterials: an interfacial approach. *Academic Press, Inc., 1972*, 385.

Hench, L. L., & Polak, J. M. (2002). Third-generation biomedical materials. *Science, 295*(5557), 1014-1017.

Hench, L. L., Wilson, J., McLaren, M., & Niesz, D. (1993). *An introduction to bioceramics* (Vol. 1): World Scientific Singapore.

Hong, Z., Zhang, P., He, C., Qiu, X., Liu, A., Chen, L., Chen, X., & Jing, X. (2005). Nano-composite of poly (L-lactide) and surface grafted hydroxyapatite: mechanical properties and biocompatibility. *Biomaterials, 26*(32), 6296-6304.

Hoppe, A., Güldal, N. S., & Boccaccini, A. R. (2011). A review of the biological response to ionic dissolution products from bioactive glasses and glass-ceramics. *Biomaterials, 32*(11), 2757-2774.

Hu, W., Peng, C., Luo, W., Lv, M., Li, X., Li, D., Huang, Q., & Fan, C. (2010). Graphene-based antibacterial paper. *ACS nano, 4*(7), 4317-4323.

Hu, Y., Shenderova, O. A., Hu, Z., Padgett, C. W., & Brenner, D. W. (2006). Carbon nanostructures for advanced composites. *Reports on Progress in Physics, 69*(6), 1847.

Hulbert, S., Hench, L., Forbers, D., & Bowman, L. (1982). History of bioceramics. *Ceramics International, 8*(4), 131-140.

Hummers Jr, W. S., & Offeman, R. E. (1958). Preparation of graphitic oxide. *Journal of the American Chemical Society, 80*(6), 1339-1339.

Isago, Y., Suzuki, R., Isono, E., Noguchi, Y., & Kuroyanagi, Y. (2014). Development of a Freeze-Dried Skin Care Product Composed of Hyaluronic Acid and Poly (γ-Glutamic Acid) Containing Bioactive Components for Application after Chemical Peels. *Open Journal of Regenerative Medicine, 3*(03), 45.

Jadalannagari, S., Deshmukh, K., Verma, A. K., Kowshik, R. V., Ramanan, M., & Roy, S. (2014). Lanthanum-Doped Hydroxyapatite Nanoparticles as Biocompatible Fluorescent Probes for Cellular Internalization and Biolabeling. *Science of Advanced Materials, 6*(2), 312-319.

Janković, A., Eraković, S., Mitrić, M., Matić, I. Z., Juranić, Z. D., Tsui, G. C., Tang, C.-y., Mišković-Stanković, V., Rhee, K. Y., & Park, S. J. (2014). Bioactive Hydroxyapatite/Graphene Composite Coating and Its Corrosion Stability in Simulated Body Fluid. *Journal of Alloys and Compounds*.

Janković, A., Eraković, S., Mitrić, M., Matić, I. Z., Juranić, Z. D., Tsui, G. C. P., Tang, C.-y., Mišković-Stanković, V., Rhee, K. Y., & Park, S. J. (2015). Bioactive hydroxyapatite/graphene composite coating and its corrosion stability in simulated body fluid. *Journal of Alloys and Compounds, 624*(0), 148-157.

Jansen, J., Van der Waerden, J., & Wolke, J. (1993). Histologic investigation of the biologic behavior of different hydroxyapatite plasma-sprayed coatings in rabbits. *Journal of biomedical materials research, 27*(5), 603-610.

Jarcho, M., Bolen, C., Thomas, M., Bobick, J., Kay, J., & Doremus, R. H. (1976). Hydroxylapatite synthesis and characterization in dense polycrystalline form. *Journal of Materials Science, 11*(11), 2027-2035.

Kadir, A., Rafiq, M., & Mahmood, N. H. (2013). Characterization, antibacterial and in vitro compatibility of zinc-silver doped hydroxyapatite nanoparticles prepared through microwave synthesis. *Ceramics International, 40*(3), 4507-4513.

Kalita, S. J., & Bhatt, H. A. (2007). Nanocrystalline hydroxyapatite doped with magnesium and zinc: Synthesis and characterization. *Materials Science and Engineering: C, 27*(4), 837-848.

Kannan, S., Vieira, S., Olhero, S., Torres, P., Pina, S., Da Cruz e Silva, O., & Ferreira, J. (2011). Synthesis, mechanical and biological characterization of ionic doped carbonated hydroxyapatite/β-tricalcium phosphate mixtures. *Acta Biomaterialia, 7*(4), 1835-1843.

Kaygili, O., Dorozhkin, S. V., & Keser, S. (2014). Synthesis and characterization of Ce-substituted hydroxyapatite by sol–gel method. *Materials Science and Engineering: C, 42*, 78-82.

Kim, H.-M., Himeno, T., Kokubo, T., & Nakamura, T. (2005). Process and kinetics of bonelike apatite formation on sintered hydroxyapatite in a simulated body fluid. *Biomaterials, 26*(21), 4366-4373.

Kim, J., Cote, L. J., Kim, F., Yuan, W., Shull, K. R., & Huang, J. (2010). Graphene oxide sheets at interfaces. *Journal of the American Chemical Society, 132*(23), 8180-8186.

Kim, S., Kong, Y.-M., Lee, I.-S., & Kim, H.-E. (2002). Effect of calcinations of starting powder on mechanical properties of hydroxyapatite–alumina bioceramic composite. *Journal of Materials Science: Materials in Medicine, 13*(3), 307-310.

Kim, S., & Park, C. B. (2010). Mussel-inspired transformation of $CaCO_3$ to bone minerals. *Biomaterials, 31*(25), 6628-6634.

Kiraly, B., Iski, E. V., Mannix, A. J., Fisher, B. L., Hersam, M. C., & Guisinger, N. P. (2013). Solid-source growth and atomic-scale characterization of graphene on Ag (111). *Nature communications, 4*.

Kokubo, T., & Takadama, H. (2006). How useful is SBF in predicting in vivo bone bioactivity? *Biomaterials, 27*(15), 2907-2915.

Kosma, V., Tsoufis, T., Koliou, T., Kazantzis, A., Beltsios, K., De Hosson, J. T. M., & Gournis, D. (2013). Fibrous hydroxyapatite-carbon nanotube composites by chemical vapor deposition: In situ fabrication, structural and morphological characterization. *Materials Science and Engineering B: Solid-State Materials for Advanced Technology, 178*(7), 457-464.

Koutsopoulos, S. (2002). Synthesis and characterization of hydroxyapatite crystals: a review study on the analytical methods. *Journal of biomedical materials research, 62*(4), 600-612.

Kumar, G. S., Thamizhavel, A., Yokogawa, Y., Kalkura, S. N., & Girija, E. (2012). Synthesis, characterization and in vitro studies of zinc and carbonate co-substituted nano-hydroxyapatite for biomedical applications. *Materials Chemistry and Physics, 134*(2), 1127-1135.

Kun, P., Tapasztó, O., Wéber, F., & Balázsi, C. (2012). Determination of structural and mechanical properties of multilayer graphene added silicon nitride-based composites. *Ceramics International, 38*(1), 211-216.

Kvetková, L., Duszová, A., Hvizdoš, P., Dusza, J., Kun, P., & Balázsi, C. (2012). Fracture toughness and toughening mechanisms in graphene platelet reinforced Si_3N_4 composites. *Scripta Materialia, 66*(10), 793-796.

Kvetková, L., Duszová, A., Kašiarová, M., Dorčáková, F., Dusza, J., & Balázsi, C. (2013). Influence of processing on fracture toughness of Si3N4; graphene platelet composites. *Journal of the European Ceramic Society, 33*(12), 2299-2304.

Lacefield, W., Hench, L., & Wilson, J. (1993). An introduction to bioceramics. *An introduction to bioceramics*.

Lafon, J.-P., Champion, E., & Bernache-Assollant, D. (2008). Processing of AB-type carbonated hydroxyapatite $Ca_{10-x}(PO_4)_{6-x}(CO_3)_x(OH)_{2-x-2y}(CO3)_y$, ceramics with controlled composition. *Journal of the European Ceramic Society, 28*(1), 139-147.

Lahiri, D., Benaduce, A. P., Rouzaud, F., Solomon, J., Keshri, A. K., Kos, L., & Agarwal, A. (2011). Wear behavior and in vitro cytotoxicity of wear debris generated from hydroxyapatite–carbon nanotube composite coating. *Journal of Biomedical Materials Research Part A, 96*(1), 1-12.

Lahiri, D., Ghosh, S., & Agarwal, A. (2012). Carbon nanotube reinforced hydroxyapatite composite for orthopedic application: A review. *Materials Science and Engineering: C, 32*(7), 1727-1758.

Lahiri, D., Khaleghi, E., Bakshi, S. R., Li, W., Olevsky, E. A., & Agarwal, A. (2013). Graphene-induced strengthening in spark plasma sintered tantalum carbide-nanotube composite. *Scripta Materialia, 68*(5), 285-288.

Lahiri, D., Singh, V., Benaduce, A. P., Seal, S., Kos, L., & Agarwal, A. (2011). Boron nitride nanotube reinforced hydroxyapatite composite: Mechanical and tribological performance and in-vitro biocompatibility to osteoblasts. *Journal of the mechanical behavior of biomedical materials, 4*(1), 44-56.

Lahiri, D., Singh, V., Keshri, A. K., Seal, S., & Agarwal, A. (2010). Carbon nanotube toughened hydroxyapatite by spark plasma sintering: Microstructural evolution and multiscale tribological properties. *Carbon, 48*(11), 3103-3120.

Landi, E., Tampieri, A., Celotti, G., & Sprio, S. (2000). Densification behaviour and mechanisms of synthetic hydroxyapatites. *Journal of the European Ceramic Society, 20*(14), 2377-2387.

Landi, E., Tampieri, A., Celotti, G., Sprio, S., Sandri, M., & Logroscino, G. (2007). Sr-substituted hydroxyapatites for osteoporotic bone replacement. *Acta Biomaterialia, 3*(6), 961-969.

Landi, E., Tampieri, A., Celotti, G., Vichi, L., & Sandri, M. (2004). Influence of synthesis and sintering parameters on the characteristics of carbonate apatite. *Biomaterials, 25*(10), 1763-1770.

Lawn, B. R., Evans, A., & Marshall, D. (1980). Elastic/plastic indentation damage in ceramics: the median/radial crack system. *Journal of the American Ceramic Society, 63*(9-10), 574-581.

Lee, C., Wei, X., Kysar, J. W., & Hone, J. (2008). Measurement of the elastic properties and intrinsic strength of monolayer graphene. *science, 321*(5887), 385-388.

Lee, D. K., Park, J. Y., Kim, M. R., & Jang, D.-J. (2011). Facile hydrothermal fabrication of hollow hexagonal hydroxyapatite prisms. *CrystEngComm, 13*(17), 5455-5459.

LeGeros, R. (1988). Calcium phosphate materials in restorative dentistry: a review. *Advances in Dental Research, 2*(1), 164-180.

LeGeros, R. Z., & LeGeros, J. P. (1993). Dense hydroxyapatite. *Adv. Ser. Ceram., 1*, 139-180.

Lester, E., Tang, S. V., Khlobystov, A., Rose, V. L., Buttery, L., & Roberts, C. J. (2013). Producing nanotubes of biocompatible hydroxyapatite by continuous hydrothermal synthesis. *CrystEngComm, 15*(17), 3256-3260.

Li, A., Sun, K., Dong, W., & Zhao, D. (2007). Mechanical properties, microstructure and histocompatibility of MWCNTs/HAp biocomposites. *Materials Letters, 61*(8), 1839-1844.

Li, H., Wang, L., Liang, C., Wang, Z., & Zhao, W. (2010). Dispersion of carbon nanotubes in hydroxyapatite powder by in situ chemical vapor deposition. *Materials Science and Engineering: B, 166*(1), 19-23.

Li, H., Zhao, X., Cao, S., Li, K., Chen, M., Xu, Z., Lu, J., & Zhang, L. (2012). Na-doped hydroxyapatite coating on carbon/carbon composites: Preparation, in vitro bioactivity and biocompatibility. *Applied Surface Science, 263*, 163-173.

Li, J., Fartash, B., & Hermansson, L. (1995). Hydroxyapatite—alumina composites and bone-bonding. *Biomaterials, 16*(5), 417-422.

Li, M., Liu, Q., Jia, Z., Xu, X., Cheng, Y., Zheng, Y., Xi, T., & Wei, S. (2014). Graphene oxide/hydroxyapatite composite coatings fabricated by electrophoretic nanotechnology for biological applications. *Carbon, 67*, 185-197.

Li, M., Liu, Q., Jia, Z., Xu, X., Shi, Y., Cheng, Y., Zheng, Y., Xi, T., & Wei, S. (2013). Electrophoretic deposition and electrochemical behavior of novel graphene oxide-hyaluronic acid-hydroxyapatite nanocomposite coatings. *Applied Surface Science, 284*, 804-810.

Li, M., Wang, Y., Liu, Q., Li, Q., Cheng, Y., Zheng, Y., Xi, T., & Wei, S. (2013). In situ synthesis and biocompatibility of nano hydroxyapatite on pristine and chitosan functionalized graphene oxide. *Journal of Materials Chemistry B, 1*(4), 475-484.

Ligot, S., Godfroid, T., Music, D., Bousser, E., Schneider, J., & Snyders, R. (2012). Tantalum-doped hydroxyapatite thin films: Synthesis and characterization. *Acta Materialia, 60*(8), 3435-3443.

Lim, H. N., Huang, N. M., Lim, S. S., Harrison, I., & Chia, C. H. (2011). Fabrication and characterization of graphene hydrogel via hydrothermal approach as a scaffold for preliminary study of cell growth. *International journal of nanomedicine, 6*, 1817-1823.

Liu, C., Huang, Y., Shen, W., & Cui, J. (2001). Kinetics of hydroxyapatite precipitation at pH 10 to 11. *Biomaterials, 22*(4), 301-306.

Liu, D.-M., Troczynski, T., & Tseng, W. J. (2001). Water-based sol–gel synthesis of hydroxyapatite: process development. *Biomaterials, 22*(13), 1721-1730.

Liu, J., Yan, H., & Jiang, K. (2013). Mechanical properties of graphene platelet-reinforced alumina ceramic composites. *Ceramics International, 39*(6), 6215-6221.

Liu, J., Yan, H., Reece, M. J., & Jiang, K. (2012). Toughening of zirconia/alumina composites by the addition of graphene platelets. *Journal of the European Ceramic Society, 32*(16), 4185-4193.

Liu, J., Ye, X., Wang, H., Zhu, M., Wang, B., & Yan, H. (2003). The influence of pH and temperature on the morphology of hydroxyapatite synthesized by hydrothermal method. *Ceramics International, 29*(6), 629-633.

Liu, X., Zhao, M., Lu, J., Ma, J., Wei, J., & Wei, S. (2012). Cell responses to two kinds of nanohydroxyapatite with different sizes and crystallinities. *International Journal of Nanomedicine, 7*, 1239-1250.

Liu, Y., Dang, Z., Wang, Y., Huang, J., & Li, H. (2014). Hydroxyapatite/graphene-nanosheet composite coatings deposited by vacuum cold spraying for biomedical applications: Inherited nanostructures and enhanced properties. *Carbon, 67*, 250-259.

Liu, Y., Huang, J., & Li, H. (2013a). Synthesis of hydroxyapatite-reduced graphite oxide nanocomposites for biomedical applications: oriented nucleation and epitaxial growth of hydroxyapatite. *Journal of Materials Chemistry B, 1*(13), 1826-1834. doi:10.1039/C3TB00531C

Liu, Y., Huang, J., & Li, H. (2013b). Synthesis of hydroxyapatite–reduced graphite oxide nanocomposites for biomedical applications: oriented nucleation and epitaxial growth of hydroxyapatite. *Journal of Materials Chemistry B, 1*(13), 1826-1834.

Lobo, A. O., Corat, M. A., Ramos, S. C., Matsushima, J. T., Granato, A. E., Pacheco-Soares, C., & Corat, E. J. (2010). Fast preparation of hydroxyapatite/superhydrophilic vertically aligned multiwalled carbon nanotube composites for bioactive application. *Langmuir, 26*(23), 18308-18314.

Ma, H., Su, W., Tai, Z., Sun, D., Yan, X., Liu, B., & Xue, Q. (2012). Preparation and cytocompatibility of polylactic acid/hydroxyapatite/graphene oxide nanocomposite fibrous membrane. *Chinese Science Bulletin, 57*(23), 3051-3058.

Ma, M.-G., Zhu, Y.-J., & Chang, J. (2008). Solvothermal preparation of hydroxyapatite microtubes in water/ N, N-dimethylformamide mixed solvents. *Materials Letters, 62*(10), 1642-1645.

Manicone, P. F., Rossi Iommetti, P., & Raffaelli, L. (2007). An overview of zirconia ceramics: basic properties and clinical applications. *Journal of dentistry, 35*(11), 819-826.

Mardziah, C., Sopyan, I., & Ramesh, S. (2009). Strontium-Doped Hydroxyapatite Nanopowder via Sol-Gel Method: Effect of Strontium Concentration and Calcination Temperature on Phase Behavior. *Trends Biomater. Artif. Organs, 23*(2), 105-113.

Martin, R., Chapman, M., Sharkey, N., Zissimos, S., Bay, B., & Shors, E. (1993). Bone ingrowth and mechanical properties of coralline hydroxyapatite 1 yr after implantation. *Biomaterials, 14*(5), 341-348.

Medvecký, Ľ., Štulajterová, R., Parilák, Ľ., Trpčevská, J., Ďurišin, J., & Barinov, S. (2006). Influence of manganese on stability and particle growth of hydroxyapatite in simulated body fluid. *Colloids and Surfaces A: Physicochemical and Engineering Aspects, 281*(1), 221-229.

Mehrali, M., Moghaddam, E., Shirazi, S. F. S., Baradaran, S., Mehrali, M., Latibari, S. T., Metselaar, H. S. C., Kadri, N. A., Zandi, K., & Osman, N. A. A. (2014a). Mechanical and In Vitro Biological Performance of Graphene Nanoplatelets Reinforced Calcium Silicate Composite. *PloS one, 9*(9), e106802.

Mehrali, M., Moghaddam, E., Shirazi, S. F. S., Baradaran, S., Mehrali, M., Latibari, S. T., Metselaar, H. S. C., Kadri, N. A., Zandi, K., & Osman, N. A. A. (2014b). Synthesis, Mechanical Properties, and in Vitro Biocompatibility with Osteoblasts of Calcium

Silicate–Reduced Graphene Oxide Composites. *ACS applied materials & interfaces, 6*(6), 3947-3962.

Meng, Y., Tang, C., Tsui, C., & Uskokovic, P. (2009). Fabrication and characterization of ha-zro2-MWCNT ceramic composites. *Journal of Composite Materials*.

Meng, Y. H., Tang, C. Y., & Tsui, C. P. (2006). *Fabrication and characterization of HA/CNT bioceramics.* Paper presented at the Materials Science Forum.

Miao, S., Weng, W., Cheng, K., Du, P., Shen, G., Han, G., & Zhang, S. (2005). Sol–gel preparation of Zn-doped fluoridated hydroxyapatite films. *Surface and Coatings Technology, 198*(1), 223-226.

Miranzo, P., Ramírez, C., Román-Manso, B., Garzón, L., Gutiérrez, H. R., Terrones, M., Ocal, C., Osendi, M. I., & Belmonte, M. (2013). In situ processing of electrically conducting graphene/SiC nanocomposites. *Journal of the European Ceramic Society, 33*(10), 1665-1674.

Mobasherpour, I., Heshajin, M. S., Kazemzadeh, A., & Zakeri, M. (2007). Synthesis of nanocrystalline hydroxyapatite by using precipitation method. *Journal of Alloys and Compounds, 430*(1), 330-333.

Moussy, F. (2010). Biomaterials for the developing world. *Journal of Biomedical Materials Research Part A, 94A*(4), 1001-1003. doi:10.1002/jbm.a.32866

Muguruma, H. (2010). Plasma-Polymerized Films for Biochip Design. *Plasma Processes and Polymers, 7*(2), 151-162.

Nakamura, S., Takeda, H., & Yamashita, K. (2001). Proton transport polarization and depolarization of hydroxyapatite ceramics. *Journal of Applied Physics, 89*(10), 5386-5392.

Nandiyanto, A. B. D., & Okuyama, K. (2011). Progress in developing spray-drying methods for the production of controlled morphology particles: From the nanometer to submicrometer size ranges. *Advanced Powder Technology, 22*(1), 1-19.

Nasiri-Tabrizi, B., & Fahami, A. (2014). Thermally induced crystallization of mechanosynthesized chlorapatite–titania composite nanopowders. *Ceramics International, 40*(6), 8201-8210.

Nasiri-Tabrizi, B., Honarmandi, P., Ebrahimi-Kahrizsangi, R., & Honarmandi, P. (2009). Synthesis of nanosize single-crystal hydroxyapatite via mechanochemical method. *Materials Letters, 63*(5), 543-546.

Nathanael, A. J., Mangalaraj, D., Hong, S., & Masuda, Y. (2011). Synthesis and in-depth analysis of highly ordered yttrium doped hydroxyapatite nanorods prepared by hydrothermal method and its mechanical analysis. *Materials Characterization, 62*(12), 1109-1115.

Nedelec, J.-M., Courthéoux, L., Jallot, E., Kinowski, C., Lao, J., Laquerriere, P., Mansuy, C., Renaudin, G., & Turrell, S. (2008). Materials doping through sol–gel

chemistry: a little something can make a big difference. *Journal of Sol-Gel Science and Technology, 46*(3), 259-271.

Neelgund, G. M., Oki, A., & Luo, Z. (2013). In situ deposition of hydroxyapatite on graphene nanosheets. *Materials Research Bulletin, 48*(2), 175-179.

Nethravathi, C., & Rajamathi, M. (2008). Chemically modified graphene sheets produced by the solvothermal reduction of colloidal dispersions of graphite oxide. *Carbon, 46*(14), 1994-1998.

Ni, Z. H., Wang, H. M., Ma, Y., Kasim, J., Wu, Y. H., & Shen, Z. X. (2008). Tunable stress and controlled thickness modification in graphene by annealing. *ACS Nano, 2*(5), 1033-1039.

Nieto, A., Lahiri, D., & Agarwal, A. (2012). Synthesis and properties of bulk graphene nanoplatelets consolidated by spark plasma sintering. *Carbon, 50*(11), 4068-4077.

Nieto, A., Lahiri, D., & Agarwal, A. (2013). Graphene NanoPlatelets reinforced tantalum carbide consolidated by spark plasma sintering. *Materials Science and Engineering: A, 582*, 338-346.

Noda, I., Miyaji, F., Ando, Y., Miyamoto, H., Shimazaki, T., Yonekura, Y., Miyazaki, M., Mawatari, M., & Hotokebuchi, T. (2009). Development of novel thermal sprayed antibacterial coating and evaluation of release properties of silver ions. *Journal of Biomedical Materials Research Part B: Applied Biomaterials, 89*(2), 456-465.

Novoselov, K. S., Geim, A. K., Morozov, S., Jiang, D., Zhang, Y., Dubonos, S., Grigorieva, I., & Firsov, A. (2004). Electric field effect in atomically thin carbon films. *science, 306*(5696), 666-669.

Núñez, J. D., Benito, A. M., González, R., Aragón, J., Arenal, R., & Maser, W. K. (2014). Integration and bioactivity of hydroxyapatite grown on carbon nanotubes and graphene oxide. *Carbon, 79*, 590-604.

Oh, S., Oh, N., Appleford, M., & Ong, J. L. (2006). Bioceramics for tissue engineering applications-a review. *American journal of biochemistry and biotechnology, 2*(2), 49.

Okumura, M., Ohgushi, H., & Tamai, S. (1991). Bonding osteogenesis in coralline hydroxyapatite combined with bone marrow cells. *Biomaterials, 12*(4), 411-416.

Oryan, A., Alidadi, S., Moshiri, A., & Maffulli, N. (2014). Bone regenerative medicine: classic options, novel strategies, and future directions. *Journal of orthopaedic surgery and research, 9*(1), 18.

Osborn, J., & Newesely, H. (1980). The material science of calcium phosphate ceramics. *Biomaterials, 1*(2), 108-111.

Oyefusi, A., Olanipekun, O., Neelgund, G. M., Peterson, D., Stone, J. M., Williams, E., Carson, L., Regisford, G., & Oki, A. (2014). Hydroxyapatite grafted carbon nanotubes and graphene nanosheets: Promising bone implant materials. *Spectrochimica Acta Part A: Molecular and Biomolecular Spectroscopy, 132*, 410-416.

Paluszkiewicz, C., Ślósarczyk, A., Pijocha, D., Sitarz, M., Bućko, M., Zima, A., Chróścicka, A., & Lewandowska-Szumieł, M. (2010). Synthesis, structural properties and thermal stability of Mn-doped hydroxyapatite. *Journal of Molecular Structure, 976*(1–3), 301-309.

Pan, H., Zhao, X., Darvell, B. W., & Lu, W. W. (2010). Apatite-formation ability–Predictor of "bioactivity"? *Acta Biomaterialia, 6*(11), 4181-4188.

Park, S., & Ruoff, R. S. (2009). Chemical methods for the production of graphenes. *Nature nanotechnology, 4*(4), 217-224.

Paul, W., & Sharma, C. (1999). Development of porous spherical hydroxyapatite granules: application towards protein delivery. *Journal of Materials Science: Materials in Medicine, 10*(7), 383-388.

Pei, S., & Cheng, H.-M. (2012). The reduction of graphene oxide. *Carbon, 50*(9), 3210-3228.

Pham, H. D., Pham, V. H., Cuong, T. V., Nguyen-Phan, T.-D., Chung, J. S., Shin, E. W., & Kim, S. (2011). Synthesis of the chemically converted graphene xerogel with superior electrical conductivity. *Chemical Communications, 47*(34), 9672-9674.

Pielichowska, K., & Blazewicz, S. (2010). Bioactive polymer/hydroxyapatite (nano) composites for bone tissue regeneration *Biopolymers* (pp. 97-207): Springer.

Pierson, H. (1993). Handbook of carbon, graphite, diamond and fullerenes: properties, processing and applications, 1993. *NY: William Andrew Publishing/Noyes*.

Poinern, G. E., Brundavanam, R. K., Mondinos, N., & Jiang, Z.-T. (2009). Synthesis and characterisation of nanohydroxyapatite using an ultrasound assisted method. *Ultrasonics Sonochemistry, 16*(4), 469-474.

Porwal, H., Tatarko, P., Grasso, S., Hu, C., Boccaccini, A. R., Dlouhý, I., & Reece, M. J. (2013). Toughened and machinable glass matrix composites reinforced with graphene and graphene-oxide nano platelets. *Science and Technology of Advanced Materials, 14*(5), 055007.

Qi, C., Zhu, Y.-J., Ding, G.-J., Wu, J., & Chen, F. (2015). Solvothermal synthesis of hydroxyapatite nanostructures with various morphologies using adenosine 5′-monophosphate sodium salt as an organic phosphorus source. *RSC Advances, 5*(5), 3792-3798.

Quan, R., Yang, D., Wu, X., Wang, H., Miao, X., & Li, W. (2008). In vitro and in vivo biocompatibility of graded hydroxyapatite–zirconia composite bioceramic. *Journal of Materials Science: Materials in Medicine, 19*(1), 183-187.

Radin, S., & Ducheyne, P. (1992). Plasma spraying induced changes of calcium phosphate ceramic characteristics and the effect onin vitro stability. *Journal of Materials Science: Materials in Medicine, 3*(1), 33-42.

Rafiee, M. A., Rafiee, J., Wang, Z., Song, H., Yu, Z.-Z., & Koratkar, N. (2009). Enhanced mechanical properties of nanocomposites at low graphene content. *ACS nano, 3*(12), 3884-3890.

Raksujarit, A., Pengpat, K., Rujijanagul, G., & Tunkasiri, T. (2010). Processing and properties of nanoporous hydroxyapatite ceramics. *Materials & Design, 31*(4), 1658-1660.

Ramirez, C., Miranzo, P., Belmonte, M., Osendi, M. I., Poza, P., Vega-Diaz, S. M., & Terrones, M. (2014). Extraordinary toughening enhancement and flexural strength in Si_3N_4 composites using graphene sheets. *Journal of the European Ceramic Society, 34*(2), 161-169.

Ravaglioli, A., & Krajewski, A. (1992). *Bioceramics*: Springer.

Ravarian, R., Moztarzadeh, F., Hashjin, M. S., Rabiee, S., Khoshakhlagh, P., & Tahriri, M. (2010). Synthesis, characterization and bioactivity investigation of bioglass/hydroxyapatite composite. *Ceramics International, 36*(1), 291-297.

Reina, A., Jia, X., Ho, J., Nezich, D., Son, H., Bulovic, V., Dresselhaus, M. S., & Jing, K. (2009). Large area, few-layer graphene films on arbitrary substrates by chemical vapor deposition. *Nano Letters, 9*(1), 30-35.

Reina, A., Jia, X., Ho, J., Nezich, D., Son, H., Bulovic, V., Dresselhaus, M. S., & Kong, J. (2008). Large area, few-layer graphene films on arbitrary substrates by chemical vapor deposition. *Nano Letters, 9*(1), 30-35.

Ren, F., Leng, Y., Xin, R., & Ge, X. (2010). Synthesis, characterization and ab initio simulation of magnesium-substituted hydroxyapatite. *Acta Biomaterialia, 6*(7), 2787-2796.

Rho, J.-Y., Tsui, T. Y., & Pharr, G. M. (1997). Elastic properties of human cortical and trabecular lamellar bone measured by nanoindentation. *Biomaterials, 18*(20), 1325-1330.

Roy, M., Bandyopadhyay, A., & Bose, S. (2011). Induction plasma sprayed Sr and Mg doped nano hydroxyapatite coatings on Ti for bone implant. *Journal of Biomedical Materials Research Part B: Applied Biomaterials, 99*(2), 258-265.

Ruys, A., Wei, M., Sorrell, C., Dickson, M., Brandwood, A., & Milthorpe, B. (1995). Sintering effects on the strength of hydroxyapatite. *Biomaterials, 16*(5), 409-415.

Sadeghian, Z., Heinrich, J., & Moztarzadeh, F. (2006). Influence of powder pre-treatments and milling on dispersion ability of aqueous hydroxyapatite-based suspensions. *Ceramics International, 32*(3), 331-337.

Safavi, A., & Sorouri, M. (2013). Multiwalled carbon nanotube wrapped hydroxyapatite, convenient synthesis via microwave assisted solid state metathesis. *Materials Letters, 91*, 287-290.

Salgado, A. J., Coutinho, O. P., & Reis, R. L. (2004). Bone tissue engineering: state of the art and future trends. *Macromolecular Bioscience, 4*(8), 743-765.

Sato, M., Sambito, M. A., Aslani, A., Kalkhoran, N. M., Slamovich, E. B., & Webster, T. J. (2006). Increased osteoblast functions on undoped and yttrium-doped nanocrystalline hydroxyapatite coatings on titanium. *Biomaterials, 27*(11), 2358-2369.

Scaglione, S., & Quarto, R. (2009). Clinical Applications of Bone Tissue Engineering *Strategies in Regenerative Medicine* (pp. 1-18): Springer.

Schepers, E., Clercq, M., Ducheyne, P., & Kempeneers, R. (1991). Bioactive glass particulate material as a filler for bone lesions. *Journal of oral rehabilitation, 18*(5), 439-452.

Seckler, M., Danese, M., Derenzo, S., Valarelli, J., Giulietti, M., & Rodríguez-Clemente, R. (1999). Influence of process conditions on hydroxyapatite crystallinity obtained by direct crystallization. *Materials research, 2*(2), 59-62.

Shah, M. S. A. S., Zhang, K., Park, A. R., Kim, K. S., Park, N.-G., Park, J. H., & Yoo, P. J. (2013). Single-step solvothermal synthesis of mesoporous Ag–TiO2–reduced graphene oxide ternary composites with enhanced photocatalytic activity. *Nanoscale, 5*(11), 5093-5101.

Shen, M.-Y., Chang, T.-Y., Hsieh, T.-H., Li, Y.-L., Chiang, C.-L., Yang, H., & Yip, M.-C. (2013). Mechanical properties and tensile fatigue of graphene nanoplatelets reinforced polymer nanocomposites. *Journal of Nanomaterials, 2013*, 1.

Shenderova, O., Zhirnov, V., & Brenner, D. (2002). Carbon nanostructures. *Critical Reviews in Solid State and Material Sciences, 27*(3-4), 227-356.

Shepherd, D. V., Kauppinen, K., Brooks, R. A., & Best, S. M. (2014). An in vitro study into the effect of zinc substituted hydroxyapatite on osteoclast number and activity. *Journal of Biomedical Materials Research Part A*.

Shepperd, J., & Apthorp, H. (2005). A contemporary snapshot of the use of hydroxyapatite coating in orthopaedic surgery. *Journal of Bone & Joint Surgery, British Volume, 87*(8), 1046-1049.

Shiao, Y. H., Lee, S. H., & Kasprzak, K. S. (1998). Cell cycle arrest, apoptosis and p53 expression in nickel(II) acetate-treated Chinese hamster ovary cells. *Carcinogenesis, 19*(7), 1203-1207.

Shin, J.-H., & Hong, S.-H. (2014). Fabrication and properties of reduced graphene oxide reinforced yttria-stabilized zirconia composite ceramics. *Journal of the European Ceramic Society, 34*(5), 1297-1302.

Shirazi, F., Moghaddam, E., Mehrali, M., Oshkour, A., Metselaar, H., Kadri, N., Zandi, K., & Abu, N. (2014). In vitro characterization and mechanical properties of β-calcium silicate/POC composite as a bone fixation device. *Journal of Biomedical Materials Research Part A*.

Si, Y., & Samulski, E. T. (2008). Synthesis of water soluble graphene. *Nano Letters, 8*(6), 1679-1682.

Silva, C., Pinheiro, A., Miranda, M., Góes, J., & Sombra, A. (2003). Structural properties of hydroxyapatite obtained by mechanosynthesis. *Solid state sciences, 5*(4), 553-558.

Silva, V. V., Lameiras, F. S., & Domingues, R. Z. (2001). Synthesis and characterization of calcia partially stabilized zirconia-hydroxyapatite powders prepared by co-precipitation method. *Ceramics International, 27*(6), 615-620.

Singh, G. (2007). *Chemistry Of D-Block Elements*: Discovery Publishing House.

Stanić, V., Janaćković, D., Dimitrijević, S., Tanasković, S. B., Mitrić, M., Pavlović, M. S., Krstić, A., Jovanović, D., & Raičević, S. (2011). Synthesis of antimicrobial monophase silver-doped hydroxyapatite nanopowders for bone tissue engineering. *Applied Surface Science, 257*(9), 4510-4518.

Stankovich, S., Dikin, D. A., Dommett, G. H., Kohlhaas, K. M., Zimney, E. J., Stach, E. A., Piner, R. D., Nguyen, S. T., & Ruoff, R. S. (2006). Graphene-based composite materials. *Nature, 442*(7100), 282-286.

Stankovich, S., Dikin, D. A., Piner, R. D., Kohlhaas, K. A., Kleinhammes, A., Jia, Y., Wu, Y., Nguyen, S. T., & Ruoff, R. S. (2007). Synthesis of graphene-based nanosheets via chemical reduction of exfoliated graphite oxide. *Carbon, 45*(7), 1558-1565.

Stankovich, S., Piner, R. D., Nguyen, S. T., & Ruoff, R. S. (2006). Synthesis and exfoliation of isocyanate-treated graphene oxide nanoplatelets. *Carbon, 44*(15), 3342-3347.

Staudenmaier, L. (1898). Method for the preparation of graphitic acid. *Ber Dtsch Chem Ges, 31*, 1481-1487.

Suchanek, W., Yashima, M., Kakihana, M., & Yoshimura, M. (1996). Processing and mechanical properties of hydroxyapatite reinforced with hydroxyapatite whiskers. *Biomaterials, 17*(17), 1715-1723.

Sun, F., & Froes, F. (2002). Synthesis and characterization of mechanical-alloyed Ti–x Mg alloys. *Journal of Alloys and Compounds, 340*(1), 220-225.

Sun, K., Li, A., Yin, Y., & Yu, Z. (2004). Study on the fabrication of hydroxyapatite and carbon nanotube composites. *Chin. J. Biomed. Eng, 6*, 573-578.

Sun, R., Lu, Y., & Chen, K. (2009). Preparation and characterization of hollow hydroxyapatite microspheres by spray drying method. *Materials Science and Engineering: C, 29*(4), 1088-1092.

Sutter, P. W., Flege, J.-I., & Sutter, E. A. (2008). Epitaxial graphene on ruthenium. *Nature materials, 7*(5), 406-411.

Takayama, T., Todo, M., & Ito, H. (2012). Mechanical Properties and Degradability of HA/PLLA Composites with Different Particle Size Distribution *Interface Oral Health Science 2011* (pp. 100-101): Springer.

Tan, C. Y., Singh, R., Tolouei, R., Sopyan, I., & Teng, W. D. (2011). Synthesis of High Fracture Toughness of Hydroxyapatite Bioceramics. *Advanced Materials Research, 264*, 1849-1855.

Terra, J., Jiang, M., & Ellis, D. (2002). Characterization of electronic structure and bonding in hydroxyapatite: Zn substitution for Ca. *Philosophical Magazine A, 82*(11), 2357-2377.

Thian, E., Konishi, T., Kawanobe, Y., Lim, P., Choong, C., Ho, B., & Aizawa, M. (2013). Zinc-substituted hydroxyapatite: a biomaterial with enhanced bioactivity and antibacterial properties. *Journal of Materials Science: Materials in Medicine, 24*(2), 437-445.

Thomas, M., Doremus, R., Jarcho, M., & Salsbury, R. (1980). Dense hydroxylapatite: fatigue and fracture strength after various treatments, from diametral tests. *Journal of Materials Science, 15*(4), 891-894.

Tsoukleri, G., Parthenios, J., Papagelis, K., Jalil, R., Ferrari, A. C., Geim, A. K., Novoselov, K. S., & Galiotis, C. (2009). Subjecting a graphene monolayer to tension and compression. *Small, 5*(21), 2397-2402.

Tung, V. C., Allen, M. J., Yang, Y., & Kaner, R. B. (2008). High-throughput solution processing of large-scale graphene. *Nature nanotechnology, 4*(1), 25-29.

Uysal, I., Severcan, F., & Evis, Z. (2013). Characterization by Fourier transform infrared spectroscopy of hydroxyapatite co-doped with zinc and fluoride. *Ceramics International, 39*(7), 7727-7733.

Vertenten, G., Gasthuys, F., Cornelissen, M., Schacht, E., & Vlaminck, L. (2010). Enhancing bone healing and regeneration: present and future perspectives in veterinary orthopaedics. *Veterinary and Comparative Orthopaedics and Traumatology, 23*(3), 153.

Viculis, L. M., Mack, J. J., Mayer, O. M., Hahn, H. T., & Kaner, R. B. (2005). Intercalation and exfoliation routes to graphite nanoplatelets. *Journal of Materials Chemistry, 15*(9), 974-978.

Walker, L. S., Marotto, V. R., Rafiee, M. A., Koratkar, N., & Corral, E. L. (2011). Toughening in graphene ceramic composites. *Acs Nano, 5*(4), 3182-3190.

Wang, G., Wang, B., Park, J., Yang, J., Shen, X., & Yao, J. (2009). Synthesis of enhanced hydrophilic and hydrophobic graphene oxide nanosheets by a solvothermal method. *Carbon, 47*(1), 68-72.

Wang, G., Yang, J., Park, J., Gou, X., Wang, B., Liu, H., & Yao, J. (2008). Facile synthesis and characterization of graphene nanosheets. *The Journal of Physical Chemistry C, 112*(22), 8192-8195.

Wang, J., & Shaw, L. L. (2009). Nanocrystalline hydroxyapatite with simultaneous enhancements in hardness and toughness. *Biomaterials, 30*(34), 6565-6572.

Wang, K., Ruan, J., Song, H., Zhang, J., Wo, Y., Guo, S., & Cui, D. (2011). Biocompatibility of Graphene Oxide. *Nanoscale Research Letters, 6*(1), 1-8.

Wang, K., Wang, Y., Fan, Z., Yan, J., & Wei, T. (2011). Preparation of graphene nanosheet/alumina composites by spark plasma sintering. *Materials Research Bulletin, 46*(2), 315-318.

Wang, P., Li, C., Gong, H., Jiang, X., Wang, H., & Li, K. (2010). Effects of synthesis conditions on the morphology of hydroxyapatite nanoparticles produced by wet chemical process. *Powder Technology, 203*(2), 315-321.

Wang, P. E., & Chaki, T. (1993). Sintering behaviour and mechanical properties of hydroxyapatite and dicalcium phosphate. *Journal of Materials Science: Materials in Medicine, 4*(2), 150-158.

Wang, W., Zhu, Y., Watari, F., Liao, S., Yokoyama, A., Omori, M., Ai, H., & Cui, F. (2012). Carbon nanotubes/hydroxyapatite nanocomposites fabricated by spark plasma sintering for bonegraft applications. *Applied Surface Science, 262*(0), 194-199.

Wang, X., Xing, W., Zhang, P., Song, L., Yang, H., & Hu, Y. (2012). Covalent functionalization of graphene with organosilane and its use as a reinforcement in epoxy composites. *Composites Science and Technology, 72*(6), 737-743.

White, A., Inam, F., Pattinson, S., Reece, M., Windle, A., & Best, S. (2011). Comparison of properties and microstructure of dense hydroxyapatite-carbon nanotube composites prepared by spark plasma sintering and pressureless sintering.

White, A. A., Best, S. M., & Kinloch, I. A. (2007). Hydroxyapatite–carbon nanotube composites for biomedical applications: a review. *International Journal of Applied Ceramic Technology, 4*(1), 1-13.

Xu, J., Khor, K., Sui, J., & Chen, W. (2009). Preparation and characterization of a novel hydroxyapatite/carbon nanotubes composite and its interaction with osteoblast-like cells. *Materials Science and Engineering: C, 29*(1), 44-49.

Xu, J., & Khor, K. A. (2007). Chemical analysis of silica doped hydroxyapatite biomaterials consolidated by a spark plasma sintering method. *Journal of Inorganic Biochemistry, 101*(2), 187-195.

Xu, J. L., & Khor, K. A. (2007). Chemical analysis of silica doped hydroxyapatite biomaterials consolidated by a spark plasma sintering method. *Journal of Inorganic Biochemistry, 101*(2), 187-195.

Xue, W., Moore, J. L., Hosick, H. L., Bose, S., Bandyopadhyay, A., Lu, W., Cheung, K., & Luk, K. D. (2006). Osteoprecursor cell response to strontium-containing hydroxyapatite ceramics. *Journal of Biomedical Materials Research Part A, 79*(4), 804-814.

Yadhukulakrishnan, G. B., Karumuri, S., Rahman, A., Singh, R. P., Kaan Kalkan, A., & Harimkar, S. P. (2013). Spark plasma sintering of graphene reinforced zirconium diboride ultra-high temperature ceramic composites. *Ceramics International, 39*(6), 6637-6646.

Yadhukulakrishnan, G. B., Rahman, A., Karumuri, S., Stackpoole, M. M., Kalkan, A. K., Singh, R. P., & Harimkar, S. P. (2012). Spark plasma sintering of silicon carbide and multi-walled carbon nanotube reinforced zirconium diboride ceramic composite. *Materials Science and Engineering: A, 552*(0), 125-133.

Yajing, Y., Qiongqiong, D., Yong, H., Han, S., & Pang, X. (2014). Magnesium substituted hydroxyapatite coating on titanium with nanotublar TiO2 intermediate layer via electrochemical deposition. *Applied Surface Science, 305*, 77-85.

Yang, J., Yan, X., Chen, J., Ma, H., Sun, D., & Xue, Q. (2012). Comparison between metal ion and polyelectrolyte functionalization for electrophoretic deposition of graphene nanosheet films. *RSC Advances, 2*(25), 9665-9670.

Yang, L., Zhang, L., & Webster, T. J. (2011). Carbon nanostructures for orthopedic medical applications. *Nanomedicine, 6*(7), 1231-1244.

Yang, Y., Kang, Y., Sen, M., & Park, S. (2011). *Bioceramics in tissue engineering*: Springer.

Yaszemski, M. J. (2013). *Biomaterials in orthopedics*: CRC Press.

Yatongchai, C., Wren, A. W., Curran, D. J., Hornez, J.-C., & Mark R, T. (2013). Comparison of the Weibull characteristics of hydroxyapatite and strontium doped hydroxyapatite. *Journal of the mechanical behavior of biomedical materials, 21*, 95-108.

Yelten, A., Yilmaz, S., & Oktar, F. N. (2012). Sol–gel derived alumina–hydroxyapatite–tricalcium phosphate porous composite powders. *Ceramics International, 38*(4), 2659-2665.

Yilmaz, B., & Evis, Z. (2014). Raman Spectroscopy Investigation of Nano Hydroxyapatite Doped with Yttrium and Fluoride Ions. *Spectroscopy Letters, 47*(1), 24-29.

Yoshida, K., Hashimoto, K., Toda, Y., Udagawa, S., & Kanazawa, T. (2006). Fabrication of structure-controlled hydroxyapatite/zirconia composite. *Journal of the European Ceramic Society, 26*(4), 515-518.

Young, R. (1974). Implications of atomic substitutions and other structural details in apatites. *Journal of Dental Research, 53*(2), 193-203.

Yu, L.-G., Khor, K., Li, H., & Cheang, P. (2003). Effect of spark plasma sintering on the microstructure and in vitro behavior of plasma sprayed HA coatings. *Biomaterials, 24*(16), 2695-2705.

Zhang, H.-b., Zhou, K.-c., Li, Z.-y., & Huang, S.-p. (2009). Plate-like hydroxyapatite nanoparticles synthesized by the hydrothermal method. *Journal of Physics and Chemistry of Solids, 70*(1), 243-248.

Zhang, J., Yang, H., Shen, G., Cheng, P., Zhang, J., & Guo, S. (2010). Reduction of graphene oxide via L-ascorbic acid. *Chemical Communications, 46*(7), 1112-1114.

Zhang, L., Li, Y.-b., Wei, J., Zuo, Y., Han, J.-m., Wu, L., & Wang, X.-j. (2005). Preparation and characterization of chitosan/nano-hydroxyapatite composite used for bone repair by co-precipitation method [J]. *Journal of Functional Materials, 3*, 012.

Zhang, L., Liu, W., Yue, C., Zhang, T., Li, P., Xing, Z., & Chen, Y. (2013). A tough graphene nanosheet/hydroxyapatite composite with improved in vitro biocompatibility. *Carbon, 61*, 105-115.

Zhang, L., Liu, W., Yue, C., Zhang, T., Li, P., Xing, Z., & Chen, Y. (2013). A tough graphene nanosheet/hydroxyapatite composite with improved in vitro biocompatibility. *Carbon, 61*, 105-115.

Zhang, N., Liu, W., Zhu, H., Chen, L., Lin, K., & Chang, J. (2014). Tailoring Si-substitution level of Si-hydroxyapatite nanowires via regulating Si-content of calcium silicates as hydrothermal precursors. *Ceramics International, 40*(7), 11239-11243.

Zhang, Y., Li, D., Tan, X., Zhang, B., Ruan, X., Liu, H., Pan, C., Liao, L., Zhai, T., Bando, Y., Chen, S., Cai, W., & Ruoff, R. S. (2013). High quality graphene sheets from graphene oxide by hot-pressing. *Carbon, 54*, 143-148.

Zhao, Y., Sun, K.-N., Wang, W.-L., Wang, Y.-X., Sun, X.-L., Liang, Y.-J., Sun, X.-N., & Chui, P.-F. (2013). Microstructure and anisotropic mechanical properties of graphene nanoplatelet toughened biphasic calcium phosphate composite. *Ceramics International, 39*(7), 7627-7634.

Zhao, Y., Sun, K. N., Wang, W. L., Wang, Y. X., Sun, X. L., Liang, Y. J., Sun, X. N., & Chui, P. F. (2013). Microstructure and anisotropic mechanical properties of graphene nanoplatelet toughened biphasic calcium phosphate composite. *Ceramics International, 39*(7), 7627-7634.

Zhou, J., Zhang, X., Chen, J., Zeng, S., & De Groot, K. (1993). High temperature characteristics of synthetic hydroxyapatite. *Journal of Materials Science: Materials in Medicine, 4*(1), 83-85.

Zhou, W., Wang, M., Cheung, W., Guo, B., & Jia, D. (2008). Synthesis of carbonated hydroxyapatite nanospheres through nanoemulsion. *Journal of Materials Science: Materials in Medicine, 19*(1), 103-110.

Zhou, X., Leung, V., Dong, Q., Cheung, K., Chan, D., & Lu, W. (2008). Mesenchymal stem cell-based repair of articular cartilage with polyglycolic acid-hydroxyapatite biphasic scaffold. *The International journal of artificial organs, 31*(6), 480-489.

Zhou, Y., Bao, Q., Tang, L. A. L., Zhong, Y., & Loh, K. P. (2009). Hydrothermal dehydration for the "green" reduction of exfoliated graphene oxide to graphene and demonstration of tunable optical limiting properties. *Chemistry of Materials, 21*(13), 2950-2956.

Zhu, J., Wong, H. M., Yeung, K. W. K., & Tjong, S. C. (2011). Spark plasma sintered hydroxyapatite/graphite nanosheet and hydroxyapatite/multiwalled carbon nanotube composites: mechanical and in vitro cellular properties. *Advanced Engineering Materials, 13*(4), 336-341.

Zhu, Y., Murali, S., Cai, W., Li, X., Suk, J. W., Potts, J. R., & Ruoff, R. S. (2010). Graphene and graphene oxide: synthesis, properties, and applications. *Advanced Materials, 22*(35), 3906-3924.

List of Papers

Publications (ISI Journals)

2013

1. S. Baradaran*, M.Hamdi and I.H.Metselaar. (2013). Biphasic Calcium Phosphate (BCP) macroporous scaffold with different ratios of HA and β-TCP by combination of gel-casting and polymer sponge methods. *Advances in Applied Ceramics*.

2. S. Baradaran*, W.J. Basirun, M.R. Mahmoudian, M. Hamdi, Y. Alias. (2013). Synthesis And Characterization Of Monetite Prepared Using A Sonochemical Method In A Mixed Solvent System Of Water/Ethylene Glycol/N,N-Dimethylformamide. *Metallurgical and Materials Transactions A*.

3. S. Baradaran*, W.J. Basirun, E. Zalnezhad, M. Hamdi, Ahmed A.D. Sarhan, Y. Alias. (2013). Fabrication and deformation behavior of Al_2O_3/Ti/TiO_2 nanotube arrays. *Journal of the Mechanical Behavior of Biomedical Materials*.

4. E. Zalnezhad, **S. Baradaran**, A.R. Bushroa, Ahmed A.D. Sarhan. (2013). Mechanical Property Enhancement of Ti-6Al-4V by MultilayerThin Solid Film Ti/TiO2 Nano tubular Array Coating for Biomedical Application. *Metallurgical and Materials Transactions A*.

2014

5. S. Baradaran*, E. Moghaddam, W.J. Basirun, M. Mehrali, M. Sookhakian, M. Hamdi, M. R. Nakhaei Moghaddam and Y. Alias. (2014). Mechanical properties and biomedical application of nano-tube hydroxyapatite/reduced graphene oxide composite. *CARBON*.

6. M. Mehrali, S. F. Seyed Shirazi, **S. Baradaran**, M. Mehrali ,H. S. C. Metselaar, N. Adib Bin Kadri, N. Azuan Abu Osman. (2014). Facile synthesis of calcium silicate hydrate using sodium dodecyl sulfate as a surfactant assisted by ultrasonic irradiation. *Ultrasonics Sonochemistry*.

7. M. Mehrali, E. Moghaddam, S. F. S. Shirazi, **S. Baradaran**, Mohammad Mehrali, S. Tahan Latibari, Hendrik Simon Cornelis Metselaar, Nahrizul Adib Kadri, Keivan Zandi, Noor Azuan Abu Osman. (2014). Synthesis, Mechanical Properties, and *in-vitro* Biocompatibility with Osteoblasts of Calcium Silicate–Reduced Graphene Oxide Composites. *ACS applied materials & interfaces.*

8. S. Baradaran*, E. Zalnezhad, W. J. Basirun, A. M. S. Hamouda, M. Sookhakian, A. A. D. Sarhan, Y. Alias. (2014). Statistical optimization and fretting fatigue study of Zr/ZrO_2 nanotubular array coating on Ti–6Al–4V. *Surface and Coatings Technology.*

9. M. Sarraf, E. Zalnezhad, A. R. Bushroa, A. M. S. Hamouda, **S. Baradaran**, B. Nasiri-Tabrizi, A. R. Rafieerad. (2014). Structural and mechanical characterization of Al/Al $_2$ O $_3$ nanotube thin film on TiV alloy. *Applied Surface Science.*

10. M. Mehrali, E. Moghaddam, S. F. S. Shirazi, **S. Baradaran**, Mohammad Mehrali, Sara Tahan Latibari, Hendrik Simon Cornelis Metselaar, Nahrizul Adib Kadri, Keivan Zandi, Noor Azuan Abu Osman. (2014). Mechanical and *in-vitro* Biological Performance of Graphene Nanoplatelets Reinforced Calcium Silicate Composite. *PloS one*.

2015

11. S. Baradaran*, E. Moghaddam, Bahman Nasiri-Tabrizi, W.J. Basirun, M. Mehrali, M. Sookhakian, M. Hamdi, Y. Alias. (2015). Characterization of nickel-doped biphasic calcium phosphate/graphene nanoplatelet composites for biomedical application. *Materials Science and Engineering: C.*

12. A. R. Rafieerad, A. R. Bushroa, E. Zalnezhad, M. Sarraf, W. J. Basirun, **S. Baradaran**, B. Nasiri-Tabrizi. (2015). Microstructural development and corrosion behavior of self-organized TiO $_2$ nanotubes coated on Ti–6Al–7Nb. *Surface and Coatings Technology.*

13. B. Nasiri-Tabrizi, E. Zalnezhad, B. Pingguan-Murphy, W. J. Basirun, A. M. S. Hamouda, **S. Baradaran.** (2015). Structural and morphological study of mechanochemically synthesized crystalline nanoneedles of Zr-doped carbonated chlorapatite. *Materials Letters.*

14. F. S. Shirazi, M. Mehrali, B. Nasiri-Tabrizi, **S. Baradaran**, S. Gharehkhani, H. S. C. Metselaar, N. A. Kadri, N. A. Abu Osman. (2015). Mechanochemical Synthesis and Characterization of Silver (Ag$^+$) and Tantalum (Ta^{5+}) Doped Calcium Silicate Nanopowders. *Science of Advanced Materials.*

16. A. R. Rafieerad, A. R. Bushroa, E. Zalnezhad, M. Sarraf, W. J. Basirun, **S. Baradaran**, B. Nasiri-Tabrizi. (2015). Microstructural development and corrosion behavior of self-organized TiO $_2$ nanotubes coated on Ti–6Al–7Nb. *Ceramics International.*

Chapter book

B. Nasiri-Tabrizi, **S. Baradaran**, E. Zalnezhad, W. J. Basirun. (2014). Applications of electron microscopy in mechanochemistry, Microscopy: Advances in Scientific Research and Education, A. Mendez-Vilas (Ed.), **Formatex Microscopy Series** Vol. 2. pp. 791-802

Biphasic calcium phosphate (BCP) macroporous scaffold with different ratios of HA/β-TCP by combination of gel casting and polymer sponge methods

S. Baradararan*[1], M. Hamdi[2] and I. H. Metselaar[3]

Open and interconnected porous scaffolds were prepared with various ratios of hydroxyapatite (HA)/β-tricalcium phosphate by a combination of gel casting and polymer sponge methods to improve the mechanical properties and structure. The scaffolds were prepared using slurries containing 50 vol.-% of ceramic powders and sintered at 1100°C for 2 h. Thermogravimetric analysis result shows that the proper temperature to burn out organic materials and polyurethane foams is 600°C. The compressive strength was between 5·3 and 8·4 MPa. Field emission scanning electron microscope shows an open, relatively uniform and large interconnected porous structure with pore size ranging between 150 and 400 μm. X-ray diffraction and Brunauer–Emmett–Teller methods were employed to determine the microstructural crystallite and surface area respectively. The results show that the compressive strength of scaffolds increased with the increase in HA concentration. The reason can be explained by the increasing pore wall thickness and density in scaffolds.

Keywords: Porous scaffold, Gel casting, Polymer sponge, Hydroxyapatite, β-Tricalcium phosphate

Introduction

In recent decades, tissue engineering has developed as one of the most significant technologies for creating artificial organs and for repairing or replacing organ function. In the field of bone tissue engineering, the aim is to fabricate scaffolds from materials with controlled porosity, bioresorbability and biodegradability. This process begins when the blood vessel permeates into the structure of the scaffold and finally degrades and establishes new organs in place.[1–7]

During the past 30 years, bioceramics have had wide clinical applications, especially in medical implants, repair and regeneration of damaged hard tissues. In recent years, calcium phosphates have played a significant role as scaffolding materials for bone tissue engineering. Various phases of calcium phosphates were applied to fabricate porous scaffolds. Calcium phosphate biomaterials such as hydroxyapatite (HA) and β-tricalcium phosphate (β-TCP) with atomic ratio of Ca/P 1·67 and 1·5 respectively and biphasic calcium phosphate (BCP) having a combination of phases (HA/β-TCP), due to having good biocompatibility, biorestorability, osteoconductivity, sufficient mechanical properties and lack of osteoinductivity, are most widely used.[8–11] In recent researches, BCP has shown better biological properties than pure HA and β-TCP. By controlling the ratio of HA/β-TCP, BCP composites with appropriate bioactivity and biodegradability properties[12,13] were obtained. In addition, bone tissue engineering offers a porous structure due to increasing the surface area of scaffolds to improve chemical bonding between bioceramics and bones.[14,15] For that issue, a highly interconnected porosity for three-dimensional scaffolds is recommended due to their ability to support cell migration and attachment, diffusion of proteins as well as flow of biofluids.[16,17]

There are several techniques for fabricating porous bioceramic scaffolds,[18,19] including the following:

(i) solid state sintering[20]
(ii) sol–gel process[21]
(iii) replication of polymer foams by impregnation[22,23]
(iv) gel casting of foam process.[24–26]

These methods cannot completely satisfy some characteristics, such as high porosity, large size interconnected pore structure and reasonable mechanical strength. The combination of gel casting and polymer sponge in order to produce the open porosity in ceramic scaffolds as well as controlling the pore size and interconnected pore with good pore morphology was suggested.[7,27,28]

[1] Department of Engineering Design and Manufacture, Faculty of Engineering, University of Malaya, Kuala Lumpur 50603, Malaysia
[2] Center of Advanced Manufacturing and Material Processing, University of Malaya, Kuala Lumpur 50603, Malaysia
[3] Department of Mechanical Engineering, Faculty of Engineering, University of Malaya, Kuala Lumpur 50603, Malaysia

*Corresponding author, email saeid_baradaran@yahoo.com

Synthesis and Characterization of Monetite Prepared Using a Sonochemical Method in a Mixed Solvent System of Water/Ethylene Glycol/N,N-Dimethylformamide

S. BARADARAN, W.J. BASIRUN, M.R. MAHMOUDIAN, M. HAMDI, and Y. ALIAS

Bioactive monetite (anhydrous calcium hydrogen phosphate, $CaHPO_4$) has been successfully synthesized using the sonochemical method in the presence of a ternary solvent system of water/ethylene glycol (EG)/N,N-dimethylformamide (DMF). The morphology and chemical composition of the synthesized powders were characterized using field emission scanning electron microscopy, X-ray diffraction, and Fourier transform infrared spectroscopy. The results indicated that with increasing sonication time, the morphology changed slightly from a plate-like one to a combination of plates (flower-like). The formation of flower-like nanosheets requires an optimum time of 40 minutes, and the nanosheets have an average thickness of 210 ± 87 nm. The concentration of DMF clearly influences the morphology and crystal phase of the products. The ideal product was obtained using a water/EG DMF ratio of 1:2.

I. INTRODUCTION

CALCIUM phosphates have been widely investigated as implants for substituting human bone in the field of biomaterials for orthopedics.[1-3] As a bioactive material, under acidic conditions (<4.5), monetite (DCPA, $CaHPO_4$) is one of the stable phases of the calcium phosphates, which have attracted considerable attention.[4] Over the last two decades, several studies have revealed the biomedical applications of bioactive monetite. This material may be used as restorable bone replacement material and a precursor to synthesizing hydroxyapatite, which is an important component of calcium phosphate cement for skeletal repair that is employed in tissue organs, such as the urinary tract and dental stone.[5-9] Therefore, in bio-applications, controlling the morphology of calcium phosphates is crucial because the characteristics of the synthesized powder, such as biocompatibility, bioactivity, stability, and mechanical properties, depend on the structure, morphology, and crystallite size of calcium phosphates.[5]

In addition, throughout the last two decades, calcium phosphates have been synthesized with various morphologies, such as rods,[10,11] plates,[12,13] needles,[14,15] spheres,[16,17] and sheets,[18] which can be controlled by the synthesis conditions. Numerous efforts have been made to synthesize calcium phosphates with different morphologies using diverse methods. The more common techniques include hydrothermal methods,[4,6,11,19,20] solvothermal methods,[21-23] microwave,[24] electro-deposition,[25] sol-gel,[26] emulsion,[16] precipitation from micro-emulsion,[27] crystallization from solution and, in recent years, ultrasonication.[7]

Some reports already exist on the synthesis of monetite. Ma et al.[5] reported the synthesis of monetite with a flower-like morphology that consists of nanosheets using a one-step, microwave-assisted method at 368.15 K (95 °C) for 1 hour. Jokic et al.[19] synthesized monetite and hydroxyapatite whiskers using a modified hydrothermal method at 433.15 K (160 °C) for 1 hour using urea as a homogeneous precipitation agent. Jinawath et al.[6] used the hydrothermal treatment of a monocalcium phosphate monohydrate suspension and lactic acid as a chelating agent to produce monetite whiskers at 433.15 K and 473.15 K (160 °C and 200 °C) for 4 hours. Wei et al.[8] reported the synthesis of monetite nanoparticles with various morphologies, such as spheres, nanofibers, and bundles of nanowires, using cetyltrimethylammonium bromide (CTAB) as a surfactant and n-pentanol as a co-surfactant. Ruan et al.[7] synthesized monetite nanosheets using a sonochemistry-assisted method and reported the effects of ultrasonic irradiation and the CTAB surfactant on the assembly of the monetite nanosheets. This method is extensively used to fabricate nanostructured materials that possess unusual properties,[28] and it has unique reaction effects that are relevant to acoustic cavitation, including the impulsive generation, growth, and collapse of micron-sized bubbles in liquid solutions. Compared to traditional energy sources, high temperatures and pressures occur in the center of the bubbles over a short duration; the high temperatures and pressures are estimated to reach 5000 K (4727 °C) and 1800 atm, respectively. The cooling rate is greater than 10 K/s^{-1} when the bubbles implode.[29,30] The advanta-

S. BARADARAN, PhD Student, is with the Department of Engineering Design and Manufacture, Faculty of Engineering, University of Malaya, 50603 Kuala Lumpur, Malaysia. Contact e-mail: saeid_baradaran@yahoo.com W.J. BASIRUN, Y. ALIAS, Supervisors, and M.R. MAHMOUDIAN, Senior Researcher, are with the Department of Chemistry, Faculty of Science, University of Malaya, 50603 Kuala Lumpur, Malaysia. M. HAMDI, Supervisor, is with the Center of Advanced Manufacturing and Material Processing, University of Malaya, 50603 Kuala Lumpur, Malaysia.
Manuscript submitted February 29, 2012.
Article published online January 9, 2013

Research Paper

Fabrication and deformation behaviour of multilayer Al$_2$O$_3$/Ti/TiO$_2$ nanotube arrays

S. Baradaran[a,*], W.J. Basirun[b,d], E. Zalnezhad[a], M. Hamdi[c], Ahmed A.D. Sarhan[c], Y. Alias[b]

[a]Department of Engineering Design and Manufacture, Faculty of Engineering University of Malaya, 50603 Kuala Lumpur, Malaysia
[b]Department of Chemistry, Faculty of Science, University of Malaya, Kuala Lumpur 50603, Malaysia
[c]Center of Advanced Manufacturing and Material Processing, University of Malaya, 50603 Kuala Lumpur, Malaysia
[d]Nanotechnology & Catalysis Research Centre (NanoCat), Institute of Postgraduate Studies, University Malaya, 50603 Kuala Lumpur, Malaysia

ABSTRACT

In this study, titanium thin films were deposited on alumina substrates by radio frequency (RF) magnetron sputtering. The mechanical properties of the Ti coatings were evaluated in terms of adhesion strength at various RF powers, temperatures, and substrate bias voltages. The coating conditions of 400 W of RF power, 250 °C, and a 75 V substrate bias voltage produced the strongest coating adhesion, as obtained by the Taguchi optimisation method. TiO$_2$ nanotube arrays were grown as a second layer on the Ti substrates using electrochemical anodisation at a constant potential of 20 V and anodisation times of 15 min, 45 min, and 75 min in a NH$_4$F electrolyte solution (75 ethylene glycol: 25 water). The anodised titanium was annealed at 450 °C and 650 °C in a N$_2$ gas furnace to obtain different phases of titania, anatase and rutile, respectively. The mechanical properties of the anodised layer were investigated by nanoindentation. The results indicate that Young's modulus and hardness increased with annealing temperature to 650 °C.

© 2013 Elsevier Ltd. All rights reserved.

1. Introduction

Bioceramics have recently become one of the most important biomaterials used for implants. They are the type of material most compatible with the human body due to chemical similarities that facilitate their direct bonding to bone. According to their level of interaction with living tissue, bioceramics can be divided into inert and active types. Alumina (Al$_2$O$_3$) is a type of inert bioceramic utilised in orthopaedic implantation because of its good mechanical properties (high strength, high fracture toughness) and good compatibility. In addition, it is employed in the fabrication of bone plates, screws, and femoral heads and widely applied in total hip joint and knee replacement (Liu, 2007; Velmurugan et al., 2010; Youn et al., 2011).

Over the last few decades, implant coating has found a wide array of applications. The thin-film coating of implant surfaces can be performed by various methods, including plasma spraying, electrophoresis, dipping, electrochemical deposition, pulsed laser deposition, ion beam dynamic mixing, and ion beam deposition (Oh et al., 2005; Raja et al., 2005; Kar et al., 2006; Best et al., 2008; Wang et al., 2008; Kodama et al., 2009; Roy et al., 2010; Wang and Luo, 2011). Some of these methods have severe limitations such as poor

Mechanical properties and biomedical applications of a nanotube hydroxyapatite-reduced graphene oxide composite

S. Baradaran [a,*], E. Moghaddam [b], W.J. Basirun [c,h], M. Mehrali [a,d], M. Sookhakian [e],
M. Hamdi [f], M.R. Nakhaei Moghaddam [g], Y. Alias [c]

[a] Department of Mechanical Engineering, Faculty of Engineering, University of Malaya, 50603 Kuala Lumpur, Malaysia
[b] Tropical Infectious Diseases research and education Centre, Department of Medical Microbiology, Faculty of Medicine, University of Malaya, 50603 Kuala Lumpur, Malaysia
[c] Department of Chemistry, Faculty of Science, University of Malaya, 50603 Kuala Lumpur, Malaysia
[d] Department of Biomedical Engineering, Faculty of Engineering, University of Malaya, 50603 Kuala Lumpur, Malaysia
[e] Department of Physics, Faculty of Science, University of Malaya, 50603 Kuala Lumpur, Malaysia
[f] Center of Advanced Manufacturing and Material Processing, University of Malaya, 50603 Kuala Lumpur, Malaysia
[g] Department of Orthopedic Surgery, Faculty of Medicine, University of Malaya, 50603 Kuala Lumpur, Malaysia
[h] Institute of Nanotechnology & Catalysis Research (NanoCat), University of Malaya, 50603 Kuala Lumpur, Malaysia

ARTICLE INFO

ABSTRACT

As a result of the growing interest in the biological and mechanical performance of hydroxyapatite (HA)–graphene nano-sheets (GNs) composite systems, reduced graphene oxide (rGO) reinforced hydroxyapatite nano-tube (nHA) composites were synthesized in situ using a simple hydrothermal method in a mixed solvent system of ethylene glycol (EG), N,N-dimethylformamide (DMF) and water, without using any of the typical reducing agents. The consolidation process was performed by hot isostatic pressing (HIP) at 1150 °C and 160 MPa. The composites were characterized by X-ray diffraction (XRD), Fourier transform infrared spectroscopy (FTIR) and Raman spectroscopy, enabling confirmation of the synthesis and reduction of the nHA and rGO, respectively. The structure of the synthesized powder and cell attachment on the sintered sample was confirmed by field emission scanning electron microscopy (FESEM). The effects of the rGO on the mechanical properties and the in vitro biocompatibility of the nHA based ceramic composites were investigated. The elastic modulus and fracture toughness of the sintered samples increased with the increase of the rGO content when compared to the pure nHA by 86% and 40%, respectively. Cell culture and viability test results showed that the addition of the rGO promotes osteoblast adhesion and proliferation, thereby increasing the biocompatibility of the nHA–rGO composite.

© 2013 Elsevier Ltd. All rights reserved.

1. Introduction

Research in biomaterials is a rapidly growing field due to its direct relationship to human health [1]. Currently, the largest consumer market for biomaterial products is orthopedic biomaterials. Consequently, development and improvements to orthopedic biomaterials is an active and expanding research

Contents lists available at ScienceDirect

Surface & Coatings Technology

Statistical optimization and fretting fatigue study of Zr/ZrO$_2$ nanotubular array coating on Ti–6Al–4V

S. Baradaran [a], E. Zalnezhad [a,*], W.J. Basirun [b,c], A.M.S. Hamouda [d], M. Sookhakian [e], Ahmed A.D. Sarhan [a], Y. Alias [b]

[a] Department of Mechanical Engineering, Faculty of Engineering, University of Malaya, 50603 Kuala Lumpur, Malaysia
[b] Department of Chemistry, Faculty of Science, University of Malaya, Kuala Lumpur 50603, Malaysia
[c] Department of Physics, Faculty of Science, University of Malaya, Kuala Lumpur 50603, Malaysia
[d] Mechanical and Industrial Engineering Department, College of Engineering, Qatar University, P.O. Box 2713, Doha, Qatar
[e] Nanotechnology & Catalysis Research Centre (NanoCat), University of Malaya, 50603 Kuala Lumpur, Malaysia

ARTICLE INFO

ABSTRACT

Herein, the fretting fatigue behavior of zirconium nanotube arrays on the surface of Ti–6Al–4V is studied. Initially, a thin film of pure zirconium (Zr) was deposited onto a Ti–6Al–4V substrate using physical vapor deposition (PVD) magnetron sputtering for the primary layer at varying DC power, temperature and substrate bias voltage values. To obtain higher adhesion strength, the Taguchi optimization method was used to estimate the optimum coating parameters, while a Pareto ANOVA was employed to determine the significant parameters. The strongest coating adhesion, as determined by a scratch force test, was achieved at 300 W DC power, 200 °C and a 75 V bias voltage. Consequently, nanotubes were produced via Zr anodization in an NH$_4$F electrolyte solution (95 glycerol:5 water) at different times and at a constant potential of 60 V (second layer). The fretting fatigue behavior of anodized samples annealed at 400 °C and 800 °C was investigated. The results indicate that the fretting fatigue life of the ZrO$_2$ nanotube-coated samples was significantly improved at low and high cyclic fatigue at an annealing temperature of 400 °C compared to the uncoated samples.

© 2014 Elsevier B.V. All rights reserved.

1. Introduction

Metallic biomaterials used to replace and repair human body parts have attracted tremendous amounts of attention over the past two decades [1–3]. A large number of implant materials, such as bone plates, screws, dental implants, and artificial joints, which are utilized to a large extent in various medical applications, are made of titanium alloys because of titanium's excellent biocompatibility, low elastic modulus, and high corrosion resistance [4–7]. Unfortunately, the inferior wear resistance of such implants has motivated researchers to increase their focus on overcoming this issue [8,9]. Different aspects of biomedical applications and the mechanical properties of biomaterials are crucial with respect to materials being applied as long-term in vivo implants [10–12]. The nonconformity between bone and the implant surface layer is among the reasons for mechanical failure, particularly in relation to the deteriorating modulus of elasticity [13]. Therefore, it is very important to consider the mechanical properties of implant materials, especially those used in orthopedic applications. Orthopedic implant instruments are often manipulated under fatigue conditions and occasionally fail due to monotonic loads, fatigue, and corrosion fatigue [14]. Thus, investigating the mechanical performance of titanium alloys,

particularly plain and fretting fatigue life, is a significant factor regarding their use in biomedical applications [15,16].

Fretting fatigue is a phenomenon that can occur between two bodies, such as bone plates and screws [17,18]. According to a previous assessment, 74% of implants that fail in the femoral neck region and in the modular junctions do so as a result of fretting fatigue [19–22]. Throughout the past two decades, the fretting fatigue of titanium alloys has been significantly improved using surface modifications with various nitride coatings (TiN, ZrN and TiAlN) [21–24]. Nanostructured metal oxides, such as TiO$_2$ and ZrO$_2$ nanotubes, are hard and wear-resistant, which is why the use of nanostructured TiO$_2$ and ZrO$_2$ coatings is becoming the surface modification method of choice [25,26]. Zirconia nanotubes have several advantages, among which are their chemical and dimensional stability, good fracture toughness, Young's modulus similar to that of stainless steel, bending strength, excellent biocompatibility, and high resistance to corrosion by bodily fluids. Thus, zirconia coatings on titanium alloys result in a high adhesion strength and are widely used in medical applications [27,28].

Over the last few decades, various coating methods have been implemented by numerous researchers. The mechanical properties of coatings play a considerable role in biomedical implants, which is why selecting the best coating methods is a very important issue. To date, a variety of coating methods have been implemented, such as pulsed

* Corresponding author.

Characterization of nickel-doped biphasic calcium phosphate/graphene nanoplatelet composites for biomedical application

S. Baradaran [a,*], E. Moghaddam [b], Bahman Nasiri-Tabrizi [c,*], W.J. Basirun [d,e], M. Mehrali [a,f], M. Sookhakian [g], M. Hamdi [h], Y. Alias [d]

[a] Department of Mechanical Engineering, Faculty of Engineering, University of Malaya, 50603 Kuala Lumpur, Malaysia
[b] Tropical Infectious Diseases Research and Education Centre, Department of Medical Microbiology, Faculty of Medicine, University of Malaya, 50603 Kuala Lumpur, Malaysia
[c] Advanced Materials Research Center, Materials Engineering Department, Najafabad Branch, Islamic Azad University, Isfahan, Iran
[d] Department of Chemistry, Faculty of Science, University of Malaya, Kuala Lumpur 50603, Malaysia
[e] Institute of Nanotechnology & Catalysis Research (NanoCat), University Malaya, 50603 Kuala Lumpur, Malaysia
[f] Department of Biomedical Engineering, Faculty of Engineering University of Malaya, Kuala Lumpur 50603, Malaysia
[g] Department of Physics, Faculty of Science, University of Malaya, Kuala Lumpur 50603, Malaysia
[h] Center of Advanced Manufacturing and Material Processing, University of Malaya, 50603 Kuala Lumpur, Malaysia

ABSTRACT

The effect of the addition of an ionic dopant to calcium phosphates for biomedical applications requires specific research due to the essential roles played in such processes. In the present study, the mechanical and biological properties of Ni-doped hydroxyapatite (HA) and Ni-doped HA mixed with graphene nanoplatelets (GNPs) were evaluated. Ni (3 wt.% and 6 wt.%)-doped HA was synthesized using a continuous precipitation method and calcined at 900 °C for 1 h. The GNP (0.5–2 wt.%)-reinforced 6% Ni-doped HA (Ni6) composite was prepared using rotary ball milling for 15 h. The sintering process was performed using hot isostatic pressing at processing conditions of 1150 °C and 160 MPa with a 1-h holding time. The results indicated that the phase compositions and structural features of the products were noticeably affected by the Ni and GNPs. The mechanical properties of Ni6 and 1.5Ni6 were increased by 55% and 75% in hardness, 59% and 163% in fracture toughness and 120% and 85% in elastic modulus compared with monolithic HA, respectively. The in-vitro biological behavior was investigated using h-FOB osteoblast cells in 1, 3 and 5 days of culture. Based on the osteoblast results, the cytotoxicity of the products was indeed affected by the Ni doping. In addition, the effect of GNPs on the growth and proliferation of osteoblast cells was investigated in Ni6 composites containing different ratios of GNPs, where 1.5 wt.% was the optimum value.

© 2015 Elsevier B.V. All rights reserved.

1. Introduction

One of the most exciting areas in engineering disciplines involves the development of various devices for health care. Calcium phosphate (CP)-based biomaterials have attracted great attention as bone replacements due to their similarity in composition and crystal structure to bone minerals, excellent biocompatibility, bioactivity and biodegradability. However, it is imperative to understand the mechanical responses of artificially grown calcium phosphate ceramics [1]. Some of the CPs are implantable in applications such as fracture fixation plates, nails and screws in orthopedics, orthodontic wires, total joint replacement prostheses, etc. [2,3]. Among these bioceramics, the most well-known and extensively used compounds are hydroxyapatite (HA) and tricalcium phosphate (TCP) for medical implants, bone defect fillers

and bone tissue engineering [4,5]. However, many reports have mentioned the limitation of using HA and TCP due to the resulting high insolubility and poor mechanical properties, such as low ductility and brittleness, which in turn cause implant loosening and subsequent implant failure [6]. Therefore, biomaterial engineers have focused on improving the composite properties using different types of materials and synthetic techniques. Crystal structure modification of HA via ionic substitution to enhance the solubility and biological properties has attracted considerable attention. In the past two decades, there have been several studies on the substitution of calcium in apatite compounds with various metal ions such as monovalent (Ag^+ and Na^+) [7,8], divalent (Mg^{2+}, Mn^{2+}, Sr^{2+}, Cd^{2+} and Pb^{2+}) [9–13] and trivalent (La^{3+}, Y^{3+}, In^{3+}, Ga^{3+} and Eu^{3+}) ions [14–18]. The focus of the research objectives is the improvement of the bioactivity and osteoinductivity compared with pure HA; however, only a few studies have investigated the effect of such substitution on the mechanical properties of HA [19,20]. Nickel, a first-row transition element, is rarely investigated as a dopant in HA. Nickel possess good mechanical and